A Measurement of the $t\bar{t}$ Production Cross Section in the Dimuon Final State with the DØ Detector for $p\bar{p}$ Collisions at $\sqrt{s} = 1.96$ TeV

by

Susan E. Burke

A Dissertation Submitted to the Faculty of the

DEPARTMENT OF PHYSICS

In Partial Fulfillment of the Requirements
For the Degree of

DOCTOR OF PHILOSOPHY

In the Graduate College

THE UNIVERSITY OF ARIZONA

2 0 0 7

THE UNIVERSITY OF ARIZONA
GRADUATE COLLEGE

As members of the Dissertation Committee, we certify that we have read the dissertation

prepared by Susan E. Burke

entitled A Measurement of the $t\bar{t}$ Production Cross Section in the Dimuon Final State with the DØ Detector for $p\bar{p}$ Collisions at $\sqrt{s} = 1.96$ TeV

and recommend that it be accepted as fulfilling the dissertation requirement for the

Degree of Doctor of Philosophy

                                            Date: 12/19/06
_____
Kenneth Johns

                                            Date: 12/19/06
_____
Li-Zhi Fang

                                            Date: 12/19/06
_____
Ingrid Novodvorsky

                                            Date: 12/19/06
_____
Ina Sarcevic

                                            Date: 12/19/06
_____
Erich Varnes

Final approval and acceptance of this dissertation is contingent upon the candidate's submission of the final copies of the dissertation to the Graduate College.

I hereby certify that I have read this dissertation prepared under my direction and recommend that it be accepted as fulfilling the dissertation requirement.

                                            Date: 12/19/06
_____
Dissertation Director: Kenneth Johns

STATEMENT BY AUTHOR

This dissertation has been submitted in partial fulfillment of requirements for an advanced degree at The University of Arizona and is deposited in the University Library to be made available to borrowers under rules of the Library.

Brief quotations from this dissertation are allowable without special permission, provided that accurate acknowledgment of source is made. Requests for permission for extended quotation from or reproduction of this manuscript in whole or in part may be granted by the head of the major department or the Dean of the Graduate College when in his or her judgment the proposed use of the material is in the interests of scholarship. In all other instances, however, permission must be obtained from the author.

SIGNED: _____

Susan E. Burke

Acknowledgements

Table of Contents

TABLE OF CONTENTS—*Continued*

Table of Contents—*Continued*

LIST OF FIGURES

LIST OF FIGURES—*Continued*

LIST OF FIGURES—*Continued*

LIST OF FIGURES—*Continued*

List of Tables

LIST OF TABLES—*Continued*

LIST OF TABLES—*Continued*

LIST OF TABLES—*Continued*

ABSTRACT

A measurement of the top pair production cross section in the dimuon final state for proton-antiproton collisions at $\sqrt{s} = 1.96$ TeV is presented. Approximately 420 pb^{-1} of data collected with the Run II DØ detector are used for this measurement. Two data events are observed with a total expected signal plus background yield of 3.6 events. Assuming a top mass of 175 GeV, the measured cross section is:

$$\sigma_{t\bar{t}} = 3.13^{+4.17}_{-2.60}(stat)^{+0.92}_{-0.86}(sys) \pm 0.19(lumi)\text{pb}, \tag{1}$$

which is consistent with a NNLO prediction of 6.77 ± 0.42 pb.

CHAPTER 1

INTRODUCTION

This dissertation presents a measurement of the top quark pair production cross section in the dimuon decay channel. The measurement was performed at the Fermi National Accelerator Laboratory (Figure 1.1) in Batavia, Illinois where top quarks were first discovered in 1995 [1, 2]. Heavy particles, such as top quarks, can be produced in a laboratory setting by colliding lighter particles at very high energies. At Fermilab's Tevatron accelerator, these lighter particles are protons and antiprotons (particles with the same mass as protons, but with opposite charges). The protons and antiprotons are accelerated to nearly the speed of light, giving them a combined energy at collision on the order of 10^{12} eV. To date, the Fermilab Tevatron is the world's only accelerator operating at a high enough energy to produce top quarks!

Though first discovered in the mid-90s, the existence of the top quark was anticipated several decades earlier by the Standard Model, the reigning theory that describes the elementary particles and their interactions. The discovery of the top completed the spectrum of six quarks and six leptons hypothesized no later than 1977, when the fifth quark (the bottom) was first observed [3]. Since its discovery in 1995, over 50 additional measurements related to the top quark have been published by the scientific collaborations working on the two multipurpose collider detectors at Fermilab, CDF and DØ [4, 5]. These measurements test Standard Model predictions regarding top quark production and decay mechanisms, and explore top quark properties such as its mass. Unfortunately, the measurements are statistically limited, making it desirable to continuously repeat them with improved analysis techniques and larger data sets. This dissertation details one such measurement.

The cross section is a proportionality constant that represents the interaction

FIGURE 1.1. Fermi National Accelerator Laboratory (Fermilab) [6].

probability for particles to produce a given reaction. It is expressed in units of effective area. For colliding beam experiments, the cross section can be written as:

$$\sigma = \frac{R}{\mathcal{L}} \tag{1.1}$$

where R is the production rate (#/s) and $\mathcal{L}$ is the instantaneous luminosity, or the number of particles per unit time per unit area ($\mathrm{cm}^{-2}\mathrm{s}^{-1}$) [7].

In order to measure the top pair production cross section in the dimuon decay channel, a series of selection criteria designed to identify the $t\bar{t} \rightarrow \mu\mu$ events is applied. The efficiency of each of these cuts is precisely measured. The expected number of background events (events from non-$t\bar{t}$ processes that have topologies similar to $t\bar{t} \rightarrow \mu\mu$) that survive all the selection cuts is estimated with a combination of data and Monte Carlo samples. The cross section is calculated as:

$$\sigma_{t\bar{t}} = \frac{(N_{obs} - N_{bkg})}{\epsilon_{sig} \times BR(t\bar{t} \rightarrow \mu\mu) \times \mathcal{L}_{Int}} \tag{1.2}$$

where N_{obs} is the number of observed events in the data after all cuts are applied, N_{bkg} is the estimated background yield, ϵ_{sig} is the efficiency of the selection cuts in signal events, $BR(t\bar{t} \rightarrow \mu\mu)$ is the branching ratio that specifies the fraction of $t\bar{t}$ pairs that decay into $\mu\mu$ pairs (including $W \rightarrow \tau \rightarrow \mu$ decays), and $\mathcal{L}_{Int}$ is the instantaneous luminosity integrated over the time the total data set was recorded.

The most accurate Standard Model prediction for the top pair production cross section for the current collision energy at Fermilab, $\sqrt{s} = 1.96$ TeV, is 6.77 ± 0.42 pb [8, 9]. A measurement of the cross section that significantly differs from this could indicate physics beyond the Standard Model. Specifically, a measurement below prediction would be consistent with exotic top decays, while a measurement above prediction could imply new top pair production mechanisms or indicate $t\bar{t}$ resonances [10]. This measurement also serves as a consistency check with other $t\bar{t}$ decay channels since new physics can occur in unexpected places. Thus, it is very important to precisely measure the top quark pair production cross section.

In addition to serving as a probe to the Standard Model, a rigorous cross section analysis contributes to measurements of top quark properties. The selection of $t\bar{t} \rightarrow \mu\mu$ events developed in this measurement can be used by collaborators studying the top quark mass and the helicity—the projection of the spin angular momentum onto the direction of motion—of the W boson. Also, understanding the sources of systematic errors are important for later measurements when these uncertainties dominate over statistical errors.

The measurement in this dissertation utilizes an integrated luminosity of approximately 420 pb^{-1} of data collected with the DØ detector. Although this is more than eight times the data used to cite the discovery of the top quark at DØ, statistical errors still dominate the measurement [1]. The cross section measurement is currently being repeated with 1 fb^{-1} of integrated luminosity. More than twice this amount of data has been collected at DØ to date, and up to 8 fb^{-1} is expected in the next few years.

Even more promising is the upcoming turn on of the Large Hadron Collider (LHC), a proton-proton accelerator at CERN near Geneva, Switzerland. The LHC will operate at a center-of-mass energy of $\sqrt{s} = 14$ TeV, seven times higher than that of the Fermilab Tevatron, and is expected to deliver up to 10 fb^{-1} of data to its two multipurpose detectors, ATLAS and CMS, in its first year of operation alone. At such high collision energies, the predicted top pair production cross section is more than 100 times higher than the Tevatron's, resulting in an expected production of approximately 10 million $t\bar{t}$ pairs a year [11, 12]. After its first major data collection period, the LHC will increase its delivered luminosity by a factor of 10, making it a virtual top factory. Whereas the measurement presented in this dissertation and most top measurements at the Tevatron are statistics limited, measurements at the LHC will be far more precise and limited instead by systematic uncertainties.

This dissertation is organized as follows:

- Chapter 2 gives an overview of the Standard Model and the physics of the top quark.

- Chapter 3 explains the experimental apparatus used to produce and collect data.

- Chapter 4 outlines the procedure through which data recorded by the DØ detector are processed into analyzable events.

- Chapter 5 discusses the selection cuts used to identify $t\bar{t} \rightarrow \mu\mu$ events and presents the efficiency of each of these cuts.

- Chapter 6 overviews the procedure for background estimation and provides cross-checks to demonstrate that the data is sufficiently well understood.

- Chapter 7 presents the cross section measurement together with a discussion of the systematic uncertainties.

- Chapter 8 offers concluding remarks and suggests future improvements for the measurement.

- Appendix A discusses the Level 1 Calorimeter-Track Trigger, which I helped to commission as part of my service work for the DØ experiment.

CHAPTER 2

THEORY

The Standard Model combines Quantum Chromodynamics and Electroweak Theory to describe the properties of elementary particles and the interactions among them. The Standard Model has been successful in that many experiments have confirmed its predictions to a high precision, but there are still aspects of the theory that are unsatisfying. The measurement presented in this dissertation provides an opportunity to verify parts of the Standard Model or to search for physics beyond it.

This chapter begins with an overview of the Standard Model and then proceeds to discuss the top quark, focusing on top pair production mechanisms and top quark decay–both of which are directly relevant to this measurement. A more complete review of the Standard Model can be found in [7, 13, 14, 15]. More information on the top quark can be found in [13, 16].

2.1 The Standard Model

A locally invariant gauge theory of the $SU(3)_C$ and $SU(2)_L \otimes U(1)_Y$ groups, the Standard Model is the simplest renormalizable gauge theory that can predict the known elementary particles and the dominant forces that govern them. These elementary particles consist of two types of fermions, leptons and quarks, that comprise the matter field of the gauge theory, and intermediate vector bosons that mediate the particle interactions associated with the fundamental forces.

The twelve spin 1/2 fermions are shown in Table 2.1 together with their charge and approximate mass. Each of these twelve elementary particles also has an antiparticle, identical to it except for having opposite charge and spin. Antiparticles are denoted in the text with a a superscripted line, for example, antitop is given by $\bar{t}$.

Generation	Particle	Charge (e)	Mass
Quarks			
1	up	$+2/3$	1.5-3 MeV
	down	$-1/3$	3-7 MeV
2	charm	$+2/3$	1.25 GeV
	strange	$-1/3$	70-120 MeV
3	top	$+2/3$	171.4 ± 2.1 GeV
	bottom	$-1/3$	4-5 GeV
Leptons			
1	electron e	-1	0.51 MeV
	ν_e	0	< 2 eV
2	muon μ	-1	106 MeV
	ν_μ	0	< 0.2 MeV
3	tau τ	-1	1777 MeV
	ν_τ	0	< 18.2 MeV

TABLE 2.1. Summary of the elementary particles and their properties [13, 17]. The arrangement reflects the convention that both leptons and quarks are grouped in three generations, with the particles of each successive generation having greater mass than the one before it. Note that throughout this dissertation, $c = 1$ for simplicity.

The particles and antiparticles interact via three fundamental forces predicted by the Standard Model: strong, electromagnetic, and weak. The fourth and weakest fundamental force, gravity, has yet to be unified with the Standard Model. These forces, together with the integer spin bosons that mediate their interactions, are summarized in Table 2.2.

A remarkable feature of the Standard Model is that the interactions it describes arise naturally from the mathematics of the model. For example, the Standard Model exhibits the property of local gauge invariance that implies its fundamental equation, the Lagrangian, must be invariant under position dependent gauge transformations. For a given fermionic particle, a Lagrangian consisting of just a kinetic energy term does not meet that constraint. However, if one adds terms that reflect the coupling of the particle to a gauge field, invariance can be restored. Thus, the local gauge invariance constraint requires the introduction of the gauge bosons and specifies their

Force	Approximate Strength (Order of Magnitude)	Mediator	Mass of Mediator
Strong	1	Gluon	-
Electromagnetic	10^{-3}	Photon	$< 6\mathrm{x}10^{-17}$eV
Weak	10^{-14}	$W^{\pm}$	80.4 GeV
		Z^0	91.2 GeV
Gravity	10^{-43}	Graviton	?

TABLE 2.2. Summary of the fundamental forces and gauge bosons [7, 13].

interaction with the fermions. Extending this constraint to non-Abelian groups, such as the $SU(3)_C$ group (Section 2.1), additionally gives rise to interactions of the gauge bosons, gluons in this case, with themselves. Equally important, t'Hooft showed that locally invariant gauge theories are renormalizable [18]. Since the higher order terms characteristic of perturbative expansions in non-renormalizable gauge theories can blow up to infinity, a Standard Model that was not renormalizable would be unusable. In the following sections, the implications of the gauge group symmetries are explored, and the Standard Model Lagrangian is discussed.

The Strong Force The $SU(3)_C$ component of the Standard Model is quantum chromodynamics (QCD), the gauge theory associated with the strong force [19]. The strong force is responsible for binding quarks together to form hadrons, as well as binding the protons and neutrons together to form nuclei. Also referred to as the color interaction, the strong force binds colored quarks through the exchange of colored gluons, the gauge bosons that mediate the strong interaction. Quarks have three color states, referred to as as 'red', 'blue', and 'green', while antiquarks have 'antired', 'antiblue', and 'antigreen'. Gluons have have eight color states, each one consisting of a color and an anticolor. Thus, gluons can modify a quark's (antiquark's) color state through quark-gluon (antiquark-gluon) interaction or simply self-interact. Hadrons, that is particles composed of quarks, are by definition color-neutral states. Hadrons come in two types. Mesons, which are composed of a quark-antiquark pair, have a

matching color and anticolor to ensure neutrality, while baryons, formed from three quarks or three antiquarks, must combine one of each color state to be neutral. Significantly, it is the color charge that allows quarks that would otherwise occupy the same state not to violate the Pauli Exclusion Principle. Leptons do not carry the color charge, and therefore are not affected by the strong force.

A property of the $SU(3)_C$ symmetry group is that it is non-abelian, that is, the generator matrices associated with the gauge transformation do not commute. As described in Section 2.1, the requirement of local gauge invariance on non-abelian groups leads to the addition of a term in the Lagrangian that reflects gauge boson interactions. This is the gluon self-interaction already mentioned. The strong force also exhibits the property of asymptotic freedom, that is the coupling constant associated with the strong interaction decreases for increasing momentum scales. This translates to the strong force being weak at short distances and strong at large ones, allowing quarks confined within hadrons to behave as quasi-free particles, while remaining bound because the strength of the strong interaction increases as they start to separate. If a quark does escapes confinement, such as in the case of a proton-antiproton collision where the constituent quarks scatter, a quark-antiquark pair is created from the vacuum. In a process termed hadronization, the escaped quark is joined by the newly created antiquark to form a meson, while the new quark fills the hole left by the escapee. Subsequent hadrons are created in a cascade process.

The mathematical technique commonly employed to perform gauge theory calculations is perturbation theory. This technique begins with a vacuum or ground state. Small perturbations about the vacuum state represent particle interactions, and these perturbations can be expanded to higher and higher orders of a coupling constant that reflects the interaction strength. For the perturbative approach to be valid, the coupling constant of Quantum Chromodynamics, α_s, must be less than one, which can only occur at high energies. In this regime, the coupling constant can be expressed at higher orders in terms of an arbitrary energy scale, μ:

$$\alpha_s(\mu) = \frac{\alpha_s(\mu_0)}{1 + \frac{\alpha_s(\mu_0)}{4\pi}(11 - \frac{2}{3}n_f)(\log(\frac{\mu^2}{\mu_0^2}))} \tag{2.1}$$

where n_f is the number of quarks with a lower mass than the energy scale μ, and μ_0 is a constant of integration [19]. Here $\alpha_s(\mu)$ is referred to as the 'running coupling constant' because of its dependence on the energy scale at different orders [13]:

$$\mu\frac{\partial \alpha_s}{\partial \mu} = -\frac{\beta_0}{2\pi}\alpha_s^2 - \frac{\beta_1}{4\pi^2}\alpha_s^3 + \mathcal{O}(\alpha_s^4)... \tag{2.2}$$

where

$$\begin{aligned} \beta_0 &= 11 - \frac{2}{3}n_f \\ \beta_1 &= 51 - \frac{19}{3}n_f. \end{aligned} \tag{2.3}$$

Electroweak Theory and the Higgs Mechanism The Electroweak theory, also known as the Glashow-Weinberg-Salam theory, is a gauge theory of the $SU(2)_L \otimes U(1)_Y$ group [20] [21] [22]. It unifies the familiar electromagnetic force described by quantum electrodynamics with the weak force that is responsible for beta decay of unstable nuclei. Generators of the $SU(2)_L \otimes U(1)_Y$ group are the leptonic hypercharge Y and the weak isospin T, related by $Q = T_3 + Y/2$ where Q is the electric charge.

The $SU(2)_L$ symmetry of the weak force transforms fermionic particles according to their helicity: left-handed components of fermionic particles transform as doublets:

$$\begin{pmatrix} u \\ d \end{pmatrix}_L \begin{pmatrix} c \\ s \end{pmatrix}_L \begin{pmatrix} t \\ b \end{pmatrix}_L \begin{pmatrix} e \\ \nu_e \end{pmatrix}_L \begin{pmatrix} \mu \\ \nu_\mu \end{pmatrix}_L \begin{pmatrix} \tau \\ \nu_\tau \end{pmatrix}_L \tag{2.4}$$

while right-handed components of fermions transform as weak isosinglets. The coupling constants of $SU(2)_L$ and $U(1)_Y$ are typically denoted g and g', respectively.

The requirement of gauge invariance on the electroweak symmetry group necessitates four gauge bosons: three gauge bosons associated with the $SU(2)_L$ group,

typically denoted W^α ($\alpha = 1, 2, 3$) and a neutral gauge boson, B^0, associated with the $U(1)_Y$ group. These can be related to the gauge bosons listed in Table 2.2 by writing the charged weak bosons as linear combinations of W^1 and W^2, while writing the photon and the neutral gauge boson Z^0 as combinations of W^3 and B:

$$W^\pm = (W^1 \mp W^2)/\sqrt{2} \tag{2.5}$$

$$Z^0 = W^3 \cos\theta_W - B^0 \sin\theta_W \tag{2.6}$$

$$\gamma = W^3 \cos\theta_W + B^0 \sin\theta_W \tag{2.7}$$

Above θ_W is the weak mixing angle or Weinberg angle, and $\sin^2(\theta_W) \approx 0.23$ [13]. However, simply from the gauge invariance requirement, these bosons have no mass. This makes sense for the electromagnetic force, which acts over infinite range, but the weak force acts over a short range implying that its gauge bosons should be massive. The solution to this problem, proposed and developed by several scientists including Higgs, is that by requiring the gauge theory to be locally invariant while simultaneously allowing for spontaneous symmetry breaking via the introduction of a field with a non-zero vacuum expectation value, mass is imputed to the gauge bosons while the photon remains massless [23, 24, 25, 26]. This field is termed the Higgs field and the process is called the Higgs mechanism.

Before spontaneous symmetry breaking, the Higgs fields can be expressed as a scalar doublet with four degrees of freedom:

$$\begin{pmatrix} \phi_+ \\ \phi_0 \end{pmatrix}. \tag{2.8}$$

Afterward, one component of this doublet survives as a massive scalar particle called the Higgs boson. This particle should be an observable, physical, spin zero boson, but to date it has not been observed. However, even without observing the

Higgs boson, some confidence may be retained in the Higgs mechanism because it accurately predicts the mass of the W and Z bosons:

$$M_W = \frac{gv}{2} \tag{2.9}$$

$$M_Z = \frac{gv}{2\cos\theta_W} \tag{2.10}$$

where v is the vacuum expectation value of the Higgs potential [13, 14]. The ratio can be expressed as:

$$\frac{M_W}{M_Z} = \frac{g}{\sqrt{g^2 + g'^2}} = \cos\theta_W. \tag{2.11}$$

Many independent experimental measurements of M_W, M_Z and $\cos\theta_W$ have confirmed this ratio [28].

Unfortunately, the Standard Model does not predict the mass of the Higgs boson. Quarks and leptons can acquire a mass via the introduction of a Yukawa-type coupling between the fermion field and the Higgs field. However, like the Higgs boson, the quark and lepton masses are not predicted by the Standard Model.

The Standard Model Lagrangian The Standard Model Lagrangian is a sum of the Lagrangians associated with the gauge bosons and their self-couplings, the leptons and the Yukawa coupling associated with the leptons, and the quarks and the Yukawa coupling associated with the quarks:

$$L_{gauge} + L_{Higgs} + L_{leptons} + L^l_{Yukawa} + L_{quarks} + L^q_{Yukawa} \tag{2.12}$$

This Lagrangian is a function of the Higgs boson mass, the quark and lepton masses, the CKM mixing parameters (Section 2.4), the two electroweak coupling constants, and the Higgs' vacuum expectation value. However, the Standard Model is predictive with just the last three of these parameters [13, 14]. As such, three precisely measured observables can serve as its basis. Three such quantities are:

- **Fine Structure Constant** as measured by the quantum Hall effect,

  $\alpha = 1/137.03599911(46)$ [13].

- **Fermi Constant** as measured by the muon lifetime formula,

  $G_F = 1.16637(1) \times 10^{-5}$ GeV^{-2} [13].

- **Z boson Mass** as measured by Z lineshape scan at LEP,

  $M_Z = 91.1876(21)$ GeV [13].

where measurement uncertainties appear in parentheses.

To leading order, these observables can be expressed as [14]:

$$\alpha = \frac{g^2 g'^2}{4\pi(g^2 + g'^2)} \tag{2.13}$$

$$G_F = \frac{1}{\sqrt{2}v^2} \tag{2.14}$$

$$M_Z^2 = \frac{v^2(g^2 + g'^2)}{4}. \tag{2.15}$$

Precision measurements of the Z partial decay widths, W boson mass, lepton polarizations and asymmetries, and other electroweak parameters have been conducted by the four CERN LEP experiments ALEPH, DELPHI, L3, and OPAL and the SLD experiment at the Stanford Linear Collider [27, 28]. These measurements and others have confirmed the Standard Model to a precision of 10^{-6}, but the theory is still unsatisfying in many ways [29]. The Higgs boson has yet to be observed, and the model has many unpredicted parameters: the three constants g, g', and v (mentioned above), the masses of the quarks and leptons, the parameters of flavor-changing matrix of the weak force (Section 2.4), and the mass of the Higgs boson. Also unsatisfying is that the Higgs mechanism, though not inconsistent with the Standard Model, does not arise naturally in the theory. Alternate theories have been suggested. In one such

theory, called supersymmetry, a global space-time symmetry is assumed that assigns a bosonic superpartner to each fermion and vice versa [16]. To date, no supersymmetric particles have been observed, but the experimental search for physics beyond the Standard Model is ongoing. The measurement presented in this dissertation is one of many measurements that tests Standard Model predictions. Results inconsistent with these predictions could support alternate theories of new physics.

Finally, it should be noted that a truly complete theory would also incorporate gravity, which is not yet unified with the Standard Model.

2.2   Top Quark

The top quark, first observed by the CDF and DØ collaborations in 1995, has several unique features that make it interesting to study [1, 2]. First, it is nearly 35 times as heavy as its partner quark, the bottom, making it the heaviest elementary particle so far observed (Table 2.1). In fact, the top quark mass is large enough to allow decay to exotic particles such as supersymmetric particles or the charged Higgs boson. Also, the Yukawa coupling constant for the top quark is close to one, which could imply that the source of its mass generation is different than that proposed for other fermions, i.e. the Higgs mechanism. Finally, the top quark has a uniquely short lifetime. At 4×10^{-25}s it is nearly an order smaller than the characteristic time of QCD hadronization, permitting the study of top quark decay free of confinement [16].

2.3   Top Quark Pair Production

Top quark pair production at hadron colliders results either from quark-antiquark annihilation or gluon-gluon fusion. The leading order Feynman diagrams for these processes are shown in Figure 2.1 and Figure 2.2. At the Fermilab Tevatron, protons and antiprotons collide at a center-of-mass energy of $\sqrt{s} = 1.96$ TeV. Calculations
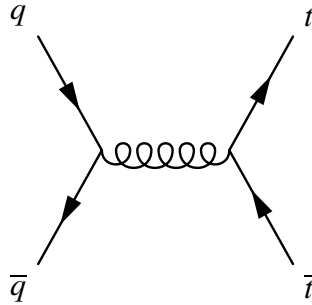
FIGURE 2.1. Quark-antiquark annihilation.
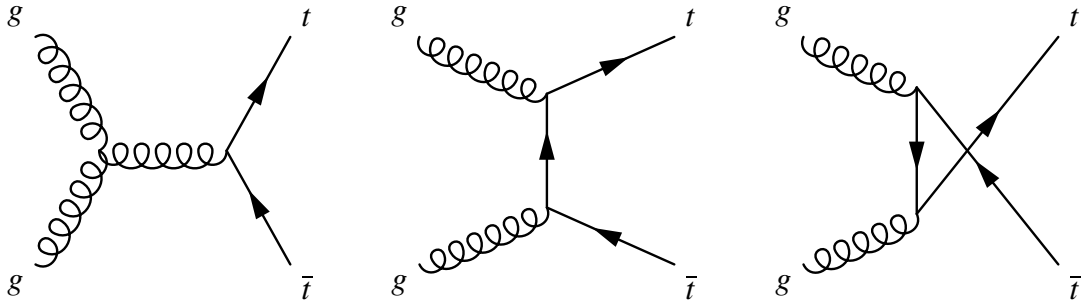
FIGURE 2.2. Gluon processes.

using leading order QCD find that $t\bar{t}$ production results from quark-antiquark annihilation about 85% of the time, while gluon-gluon fusion is responsible for the remaining 15% at this center-of-mass energy [13]. Conversely, at the Large Hadron Collider at CERN where the center-of-mass energy is $\sqrt{s} = 14$ TeV, the fraction of top quark pair production originating from quark-antiquark annihilation and gluon-gluon fusion is reversed at 10% and 90%, respectively [16].

Both mechanisms of top pair production result from the hard scatter process of $p\bar{p}$ collisions. The protons and antiprotons are composed of partons, i.e. gluons and quarks, each of which carries a fraction of the total proton or antiproton momentum. The total $t\bar{t}$ cross section can be expressed in terms of the cross sections, σ, of the two partonic processes and the parton distribution functions (PDF's), $f(x, \mu_2^2)$, which

represent the probability that the relevant parton carries fraction x of the total proton or antiproton momentum [30]:

$$\sigma(s, m_t^2) = \sum_{i,j} \int dx_1 \int dx_2 f_i(x_i, \mu_f^2) f_j(x_j, \mu_f^2) \hat{\sigma}_{ij}(\hat{s}, m_t, \alpha_s(\mu_r^2)) \qquad (2.16)$$

Above, i, j refers to possible incoming parton combinations, $\hat{s}$ is the squared center-of-mass energy of the parton interaction (defined as $\hat{s} = x_i x_j s$), and α_s is the QCD coupling constant defined in Section 2.1. Also, μ_r is the renormalization scale associated with the coupling constant (labeled just μ previously), and μ_f is a factorization scale associated with the separation of the hard scatter event into the partonic cross sections $\hat{\sigma}_{ij}$ and the scatter contributions of the remaining proton and antiproton constituents. The renormalization and factorization scales may be chosen to represent a relevant scale to the process, such as the mass of the top quark, m_t, and are often set equal to each other for calculation.

In order to calculate the total $t\bar{t}$ cross section from Equation 2.16, one first needs to calculate the partonic cross sections for each possible partonic interaction and to estimate the PDF's.

2.3.1 Partonic Cross Sections

The partonic cross sections $\hat{\sigma}_{ij}$ can be expressed as perturbative expansions of the QCD coupling constant, as:

$$\hat{\sigma}_{ij}(\rho, m_t^2, \alpha_s^2(\mu^2), \mu^2) = \frac{\alpha_s^2(\mu^2)}{m_t^2} k_{ij}\left(\rho, \alpha_s(\mu^2), \frac{\mu^2}{m_t^2}\right) \qquad (2.17)$$

where $\rho = \frac{4m_t^2}{\hat{s}}$ and k_{ij} are dimensionless functions expandable in α_s [31]:

$$k_{ij}\left(\rho, \alpha_s(\mu^2), \frac{\mu^2}{m_t^2}\right) = k_{ij}^0(\rho) + 4\pi\alpha_s(\mu^2)\left[k_{ij}^1(\rho) + \bar{k}_{ij}^1(\rho)\ln\frac{\mu^2}{m_t^2}\right] + O(\alpha_s^2). \qquad (2.18)$$

Above, the higher order corrections are split into two terms with the $\bar{k}_{ij}$ terms serving as coefficients of $\ln \frac{\mu^2}{m_t^2}$. At leading order (LO), corresponding to term k_{ij}^0, the partonic cross sections are proportional to α_s^2:

$$\hat{\sigma}(q\bar{q} \to t\bar{t}) = \frac{1}{27} \frac{\pi \alpha_s^2 \beta \rho (2 + \rho)}{m_t^2} \tag{2.19}$$

$$\hat{\sigma}(gg \to t\bar{t}) = \frac{\pi \alpha_s^2 \beta \rho}{192 m_t^2} \left[\frac{1}{\beta}(\rho^2 + 16\rho + 16) \ln \left(\frac{1+\beta}{1-\beta} \right) - 28 - 31\rho \right] \tag{2.20}$$

$$\hat{\sigma}(gq \to t\bar{t}) = \hat{\sigma}(g\bar{q} \to t\bar{t}) = 0 \tag{2.21}$$

where β is the velocity of the top quarks in the center-of-mass frame. Note that ρ, defined above as $\rho = \frac{4m_t^2}{\hat{s}}$, can also be expressed as $\rho = (1 - \beta^2)$ [30, 31].

The threshold for top pair production occurs when $\beta \to 0$, or equivalently, $\rho \to 1$ [30]. The Fermilab Tevatron operates near, but not at, the threshold for top pair production. Assuming both partons carry equal momentum $x_i \approx x_j \approx x_{threshold}$ where $x_{threshold} \approx \frac{2m_t}{\sqrt{s}}$, the Tevatron's Run II center-of-mass energy of $\sqrt{s} = 1.96$ TeV would imply a fractional momentum of $x \approx 0.18$. For this fractional momentum, the value of the quark distribution functions are significantly higher than the gluon distribution function, thus, quark-antiquark annihilation is the dominant source of top pair production at the Tevatron [16].

Unlike the LO partonic cross sections, next-to-leading order (NLO) corrections to the cross section, corresponding to k_{ij}^1 and $\bar{k}_{ij}^1$ in Equation 2.17, do not go to zero near threshold. These and higher order corrections are predominantly due to soft gluon emissions that do not suffer the phase space suppression real gluons do at threshold energies [9].

Theoretical calculations can predict the $t\bar{t}$ cross section to LO and NLO using standard perturbative techniques (including full NLO matrix elements). A technique

termed resummation is employed to evaluate the cross section at higher orders, which include the substantial logarithmic corrections due to soft gluon emissions. These corrections can be expressed in terms of a kinematic variable that represents the distance to threshold, x^{th}, and the order, n, of the QCD coupling constant, α_s^n, in the cross section:

$$\left[\frac{\ln^l(x_{th})}{x_{th}}\right]_+ \tag{2.22}$$

where $l \leq 2n - 1$ and x_{th} goes to zero at threshold.

As stated above, the LO partonic cross section is proportional to α_s^2 or $n = 2$. The corresponding leading logarithmic (LL) corrections have $l = 3$. Calculations up to next-to-next-leading order (NNLO) with next-to-next-to-leading logarithm corrections (NNLL) for which $l = 1$ have been shown to substantially reduce the dependence of the cross section on the factorization and renormalization scale μ (Equation 2.16) [9]. However, in calculating higher orders one must make a kinematic choice to define the variable x_{th}, and the dependence on kinematics is not negligible even to NNLO-NNLL. In Section 2.3.3, results are shown for NNLO with next-to-next-to-next-to leading logarithm corrections (NNNLL), for which $l = 0$. Two kinematics schemes are examined, single particle inclusive (1PI) and pair-invariant mass (PIM):

$$1PI : q(p_a) + \overline{q}(p_b) \rightarrow t(p_1) + X[\overline{t}](p_2) \tag{2.23}$$

$$PIM : q(p_a) + \overline{q}(p_b) \rightarrow t\overline{t}(p) + X(k) \tag{2.24}$$

Equation 2.23 and Equation 2.24 represent quark-antiquark annihilation where t is the top quark and X is a final state that includes antitop in 1PI kinematics and just remnants in PIM kinematics [9]. For 1PI, corrections take the form $\left[\frac{\ln^l(s_4/m^2)}{s_4}\right]_+$ where $s_4 = s + t_1 + u_1$:

$$s = (p_a + p_b)^2 \tag{2.25}$$

$$t_1 = (p_b - p_1)^2 - m^2 \tag{2.26}$$

$$u_1 = (p_a - p_1)^2 - m^2 \tag{2.27}$$

For PIM, x_{th} in Equation 2.22 is given by $1 - Z$ for $Z = M_{t\bar{t}}^2/s$, where $M_{t\bar{t}}$ is the top pair invariant mass [8]. In each kinematic scheme, the logarithmic corrections are resummed to calculate the partonic cross section.

2.3.2   Parton Distribution Functions

The parton distribution functions necessary to calculate the top pair production cross section (Equation 2.16) are formed by performing global QCD fits of experimental data to NLO QCD calculations. The data utilized is from HERA experiments, fixed target deep inelastic scattering experiments at Fermilab, and Tevatron jet and W production data [32].

The resulting PDF's are extracted by the CTEQ and MRST collaborations. The dominant uncertainty on the PDF's arises from a limited knowledge of the gluon density at high momentum fractions. Other sources of uncertainty include differing values of α_s assumed in the fits, and the number of fit parameters [32]. More information on the PDF's can be found in [9, 32].

2.3.3   Results

For a recent NLO calculation that incorporates next-to-leading logarithm (NLL) corrections and assumes a value of $m_{top} = 175$ GeV, the inclusive top pair production cross section at current Tevatron energies is predicted to be 6.7 ± 1 pb [32]. For this calculation, the renormalization and factorization scales were varied both individually and together over the range $\frac{m_{top}}{2} < \mu_{r,f} < 2m_{top}$ to test the scale dependence

σ (pb)

Order	MRST2002 NNLO			CTEQ6M		
	$\mu = m_t/2$	$\mu = m_t$	$\mu = 2m_t$	$\mu = m_t/2$	$\mu = m_t$	$\mu = 2m_t$
NLO	6.79	6.52	5.83	6.79	6.54	5.85
NNLO 1PI	7.00	7.17	6.99	7.01	7.21	7.04
NNLO PIM	6.14	6.35	6.28	6.08	6.33	6.29

TABLE 2.3. Cross section predictions for $\sqrt{s} = 1.96$ TeV and $m_t = 175$ GeV [9].

of the cross section. PDF's from both the CTEQ and MRST collaborations were considered. The resulting cross section range spanned 5.82 pb$-$7.41 pb, where the higher prediction corresponds to $\mu_{r,f} = \frac{m_{top}}{2}$ [32].

Higher order calculations are consistent with the above cross section result, predicting 6.77 pb $\pm$0.42 pb at NNLO with NNNLL corrections and assuming $\mu = m_{top} = 175$ GeV [8, 9]. As discussed in Section 2.3.1, higher order calculations have the advantage of reduced scale dependence of the cross section, though this remains a source of uncertainty. Other sources of theoretical uncertainty include the uncertainty in the PDF's (Section 2.3.2) and the uncertainty associated with the measurement of α_s. Table 2.3 shows a full set of cross section predictions by Kidonakis and Vogt for two different sources of PDF's and three values of the scale μ. The kinematic schemes are described in Section 2.3.1.

Figure 2.3 shows the $t\bar{t}$ cross section as a function of top quark mass. The cross section decreases rapidly with increasing top mass. It follows that accurate measurements of the $t\bar{t}$ cross section in conjunction with measurements of the top quark mass could provide a test for QCD predictions.

2.4 Top Quark Decay

According to the Standard Model, the top quark decays almost 100% of the time to a W boson and a b quark. The decay proceeds via the weak interaction. The
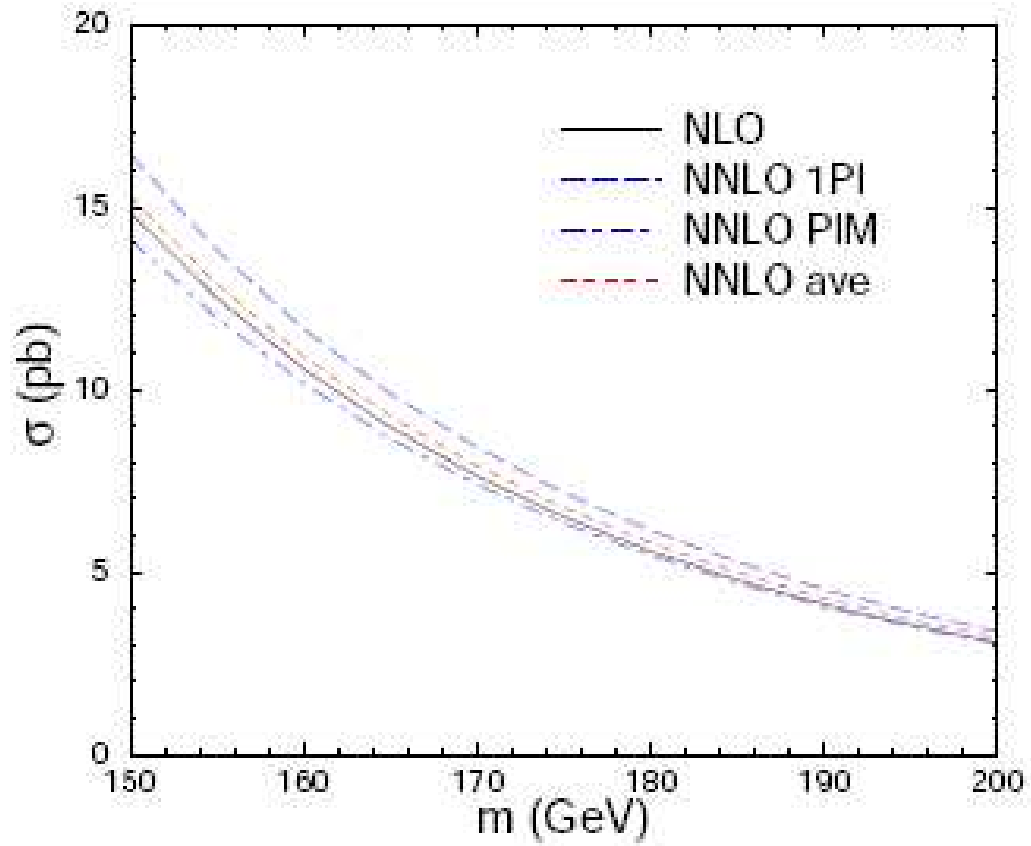
FIGURE 2.3. The theoretical $t\bar{t}$ cross section as a function of top quark mass for $\sqrt{s}=$ 1.96 TeV, assuming a scale $\mu = m_t$. Calculations are shown for NLO and NNLO using two different kinematic approaches and their average [8].

decay width, $\Gamma(t \to bW)_t$, can be expressed in terms of the top mass, m_t, the mass of the W boson, m_W, the strong coupling constant, α_s, and the Fermi constant G_F. Neglecting higher orders, it is [13]:

$$\Gamma(t \to bW) = \frac{G_F m_t^3}{8\pi\sqrt{2}} \left(1 - \frac{m_W^2}{m_t^2}\right)^2 \left(1 + 2\frac{m_W^2}{m_t^2}\right) \left[1 - \frac{2\alpha_s}{3\pi}\left(\frac{2\pi^2}{3} - \frac{5}{2}\right)\right]. \quad (2.28)$$

The lifetime, τ, of the top quark is given by $\tau = \frac{\hbar}{\Gamma}$ and is approximately 4×10^{-25} s. The top lifetime is approximately an order smaller than the characteristic time of QCD hadronization at $\approx 3 \times 10^{-24}$, making it possible to study the top quark free of confinement [16].

The weak interaction transforms quarks as doublets (Section 2.1), which implies that in addition to decaying to a b quark, the top could also decay to a s quark or d quark. The likelihood of decay to a given quark is proportional to the square of the elements of a flavor-changing matrix called the Cabibbo-Kobayashi-Maskawa (CKM) matrix, which displays the mixing between the weak (left column) and mass (right column) eigenstates of the quarks:

$$\begin{pmatrix} d^w \\ s^w \\ b^w \end{pmatrix} = \begin{pmatrix} V_{ud} & V_{us} & V_{ub} \\ V_{cd} & V_{cs} & V_{cb} \\ V_{td} & V_{ts} & V_{tb} \end{pmatrix} \begin{pmatrix} d^m \\ s^m \\ b^m \end{pmatrix}. \quad (2.29)$$

Using measurements of the lighter quark mixing elements together with the unitarity assumption and the assumption that there are only three generations of fermions, the values of V_{ts} and V_{td} can be constrained to: $V_{ts} < 0.043$ and $V_{td} < 0.014$ [13]. By contrast, V_{tb} is estimated to be greater than 0.999 [16].

For a given top-antitop pair, the final state after decay will contain two b quarks that hadronize and are detected as high P_T jets. The two W bosons can each decay individually to any weak doublet, that is either to a lepton and its associated neutrino or to quark-antiquark pair that are subsequently detected as two jets. The likelihood of decay to any given doublet is roughly equal. However, since each quark comes

	$e\nu_e$ (1/9)	$\mu\nu_\mu$ (1/9)	$\tau\nu_\tau$ (1/9)	$jj(ud$ or $c\bar{s})$ (2/3)
$e\nu_e$ (1/9)	1/81	1/81	1/81	2/27
$\mu\nu_\mu$ (1/9)	1/81	1/81	1/81	2/27
$\tau\nu_\tau$ (1/9)	1/81	1/81	1/81	2/27
$jj(ud$ or $c\bar{s})$ (2/3)	2/27	2/27	2/27	4/27

TABLE 2.4. The approximate branching ratios for $t\bar{t}$ decay, determined by the decay of the two W bosons. Here jj refers to jets arising from $W \to q\bar{q}$ decay. The original two b jets from the top decay are not shown.

in three flavors and each flavor represents an independent final state, the resulting branching ratios are approximately $\frac{1}{9}$ for each possible leptonic decay, and $\frac{1}{3}$ for the two possible quark doublets. (The third quark doublet, tb, is excluded because its mass exceeds that of the W boson.)

The measurement presented in this dissertation is the top pair production cross section in the dimuon decay channel. Since both the top and antitop quark decay to W bosons, and each W decays to a muon and muon neutrino for approximately $\frac{1}{9}$ of its decays, the total branching ratio can be approximated as $\frac{1}{81}$ (Table 2.4). The more accurate branching ratio assumed for this measurement, which includes final state muons originating from $W \to \tau\nu$ decay, is 0.01571 with a relative uncertainty of 2% [33]. The event signature in the dimuon decay channel, $t\bar{t} \to \mu\mu + \nu\nu + jj$, consists of two jets from the b quarks with high transverse momentum (P_T), two high P_T muons, and significant missing transverse energy, $\not{E}_T$, from the associated neutrinos. For simplicity, this process is written $t\bar{t} \to \mu\mu$ for the remainder of the dissertation.

Despite its low branching ratio, the dimuon channel is advantageous for study because few background processes have both two high P_T muons and significant $\not{E}_T$ in their final states. Processes that do can usually be discriminated against by requiring two high P_T jets. Such is the case with diboson production, which also suffers from a low cross section. Drell-Yan production of (Z/γ^*)+jets events has a soft P_T spectrum

relative to top events and these events have no direct decay process to dimuon final states with real neutrinos. Indirect decay proceeding via τ particles suffers from a low branching ratio. More detail on each of these background processes is given in Chapter 6.

Chapter 3

Experiment

The Fermilab Tevatron is a one kilometer-radius synchrotron that collides protons and antiprotons with sufficient energies to produce $t\bar{t}$ pairs. Collisions occur at two multipurpose detectors positioned on the synchrotron, CDF and DØ. This chapter presents an overview of the Tevatron and of the DØ detector, which was used to collect the data for this measurement. The focus is on the detector elements used to measure the energy and momentum of jets, muons, and the signature of the neutrino—all the final decay products for $t\bar{t} \rightarrow \mu\mu$ production.

3.1 The Tevatron

The Tevatron currently operates at a center-of-mass energy of $\sqrt{s} = 1.96$ TeV. This means before colliding, protons and antiprotons are accelerated to an energy of 980 GeV, only 200 miles per hour slower than the speed of light [34]. To produce such a speed, a series of five accelerators is used, each one successively increasing the energy of the particles. An antiproton source, comprised of a target and two additional accelerators, produces and stores the antiprotons prior to their injection into the Tevatron. Together these components make up Fermilab's accelerator complex, shown in Figure 3.1. The following is a brief overview of the accelerators, additional information can be found in [34, 35].

- *Proton Source* The Cockcroft-Walton pre-accelerator is the first step in the acceleration chain. Here hydrogen gas is converted to negatively charged hydrogen ions, H^-, and accelerated to an energy of 750 keV. The acceleration is accomplished as ions travel through columnar tubes from a charged dome (-750 keV)
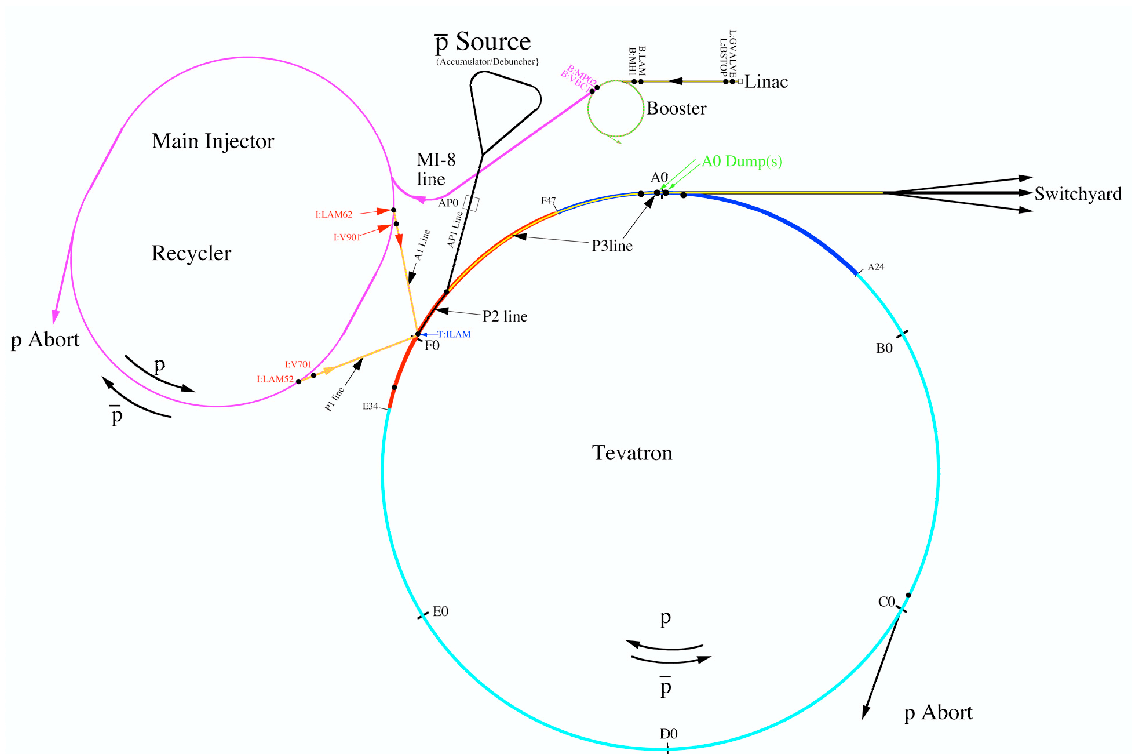
FIGURE 3.1. The Fermilab accelerator complex [35].

to a grounded wall.

- *Linac* H- ions from the Cockcroft-Walton are delivered to the Linac, a linear
  accelerator approximately 152 m long. This two-stage accelerator utilizes RF
  cavities, that is oscillating electric fields timed such that ions are given successive
  kicks by the accelerating part of the field, to accelerate the ions to a final energy
  of 400 MeV. At transfer between the the Linac and the Booster, ions are passed
  through a carbon foil, which strips off the electrons.

- *Booster* With a circumference of 475 m, the Booster is the first synchrotron in
  the chain. Protons are kept in a circular orbit by a series of magnets. Like the
  Linac, the Booster employs RF cavities for particle acceleration. Upon each
  rotation, the strength of the oscillating electric field is increased. The strength
  of the magnetic field is similarly increased with rotation in order to keep the

increasingly energetic protons at the same radius. Protons leave the Booster at an energy of 8 GeV, grouped into RF structures termed bunches.

- *Main Injector* After the Booster, protons enter a second synchrotron called the Main Injector. The circumference of the Main Injector is approximately 7 times that of the Booster, at 3319 m. The Main Injector serves several functions. It accelerates protons from 8 GeV to 150 GeV and injects them into the Tevatron. It also accelerates protons to 120 GeV and delivers them to the Antiproton Source described below. To prepare for typical collision mode in the Tevatron, the Main Injector injects 36 bunches of protons and 36 bunches of antiprotons, each at 150 GeV.

- *Tevatron* The Tevatron is the last and largest of the accelerators. Its circumference is 6283 m. The Tevatron accelerates protons and antiprotons to their final energy of 980 GeV and stores them in stable circular orbits in the same beampipe in preparation for collision. The magnets in the Tevatron are superconducting, cooled to a temperature of approximately 4 K, which makes the high currents necessary to produce and sustain these energies possible. Protons and antiprotons circle the Tevatron in opposite directions, kept apart by horizontal and vertical electrostatic separators. In collision mode, the electrostatic separators are undone at two points on the ring corresponding to the locations of the two major detectors. Here low-beta quadrupole magnets are used to focus, or reduce, the beam size for collisions. The resonant frequency of the Tevatron's RF cavities is 53 MHz, which is an RF clock period of 18.8 ns. A fully accelerated proton takes 21 μs to traverse the full Tevatron ring, and the 36×36 bunches are injected accordingly so collisions occur at each interaction point every 396 ns.

- *Antiproton Source* Antiprotons are produced in the Antiproton Source, which consists of a nickel target and two accelerators. When the 120 GeV protons from the Main Injector collide with the target, a spray of secondary particles is produced. A sample of ≈ 8 GeV antiprotons is collected from this spray, and sent to two successive synchrotrons. The first is the Debuncher, a rounded triangle-shaped synchrotron with a mean radius of 90 m. The Debuncher stochastically cools the antiprotons, reducing the the spread of antiproton momenta. The now more homogeneous 8 GeV antiprotons proceed to the second synchrotron, the Accumulator, which has the same shape and same tunnel as the Debuncher, but a mean radius of only 75 m. The antiprotons are stored in the Accumulator, undergoing further cooling, until it is time to return to the Main Injector for acceleration.

- *Recycler* The final component of the Fermilab accelerator complex is the Recycler, an antiproton storage ring that shares the Main Injector's tunnel. The Recycler receives antiprotons from the Tevatron and stores them until they can be re-injected for collisions.

3.2   DØ Detector

The DØ detector, first commissioned in the summer of 1992, was designed to study the high energy proton and antiproton collisions at the Fermilab Tevatron. It is composed of central tracking detectors, a uranium liquid-argon calorimeter, and a muon spectrometer (Figure 3.2). Approximately 125 pb^{-1} of data were collected at DØ between 1992 and 1996. This period is called Run I. Run II began in 2001 and is still in progress.

Between Run I and Run II the DØ detector was substantially upgraded. A 2 T solenoidal magnet has been added to the central tracking detectors, and a silicon microstrip tracker was installed. The forward muon system was also substantially
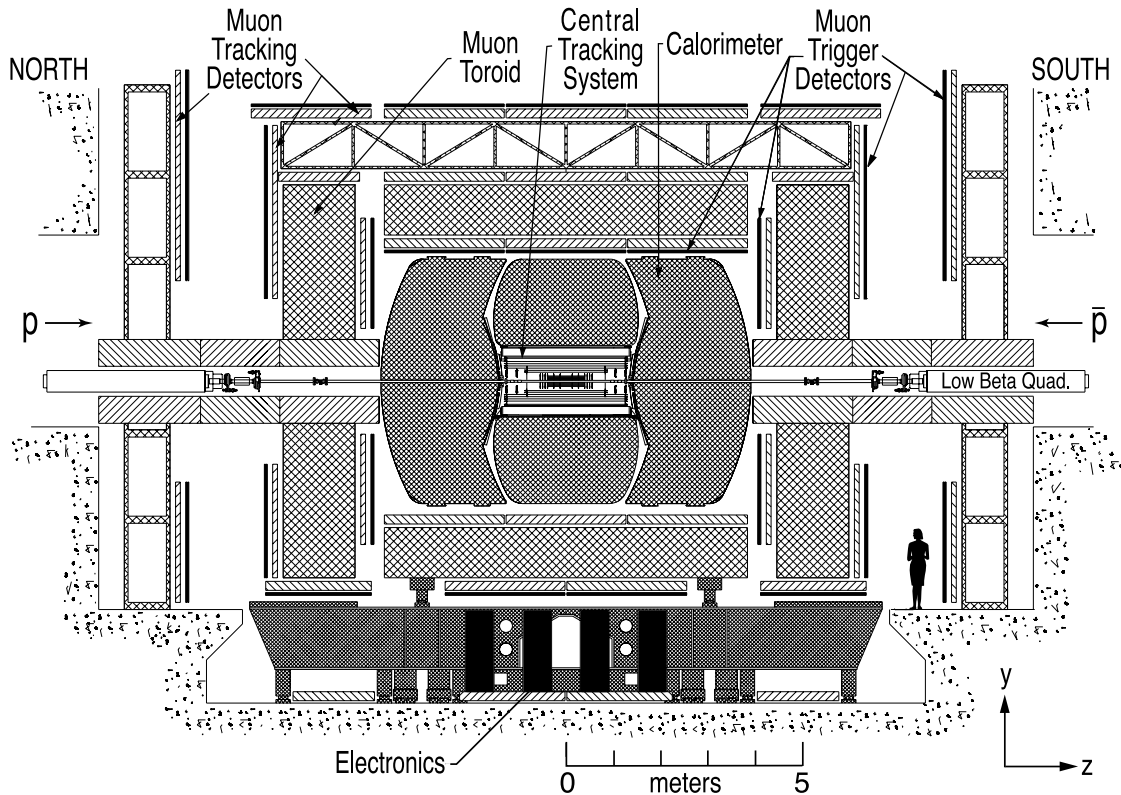
FIGURE 3.2. DØ detector for Run II [36].

upgraded, providing more robust detectors and enhanced triggering capability. The following is a brief overview of the Run II DØ detector. A more complete description can be found at [36].

3.2.1 Coordinates

The following conventions are chosen to describe the spatial coordinates of the DØ detector. The center of the DØ detector is the origin, positive y points upward from the origin, and positive z points in the direction of the proton momentum. In polar coordinates, r is defined as the perpendicular distance from the z axis, and the polar and azimuthal angles are given by θ and ϕ. Often the pseudorapidity $\eta = -\ln[\tan(\theta/2)]$ is used in place of polar angle θ. The true rapidity is given by

$y = \frac{1}{2}\ln[(E + p_z c)/(E - p_z c)]$, but the pseudorapidity is a good approximation in the limit $\frac{m}{E} \to 0$ [36].

3.2.2 Central Tracking Detectors

The central tracking detectors, shown in Figure 3.3, surround the DØ beampipe. These detectors are a silicon microstrip tracker (SMT) and a scintillating fiber tracker (CFT) within a 2 T solenoid magnet. Together they measure the momenta of charged particles and locate the primary event vertex. The transverse momentum resolution for charged particle trajectories, or tracks, measured with the central tracking detectors can be parameterized as:

$$\frac{\sigma(1/P_T)}{1/P_T} = \sqrt{\frac{(0.003P_T)^2}{L^4} + \frac{(0.026)^2}{L\sin\theta}} \tag{3.1}$$

where L is the lever arm associated with the track bending through the magnetic field [37, 38]. ($L = 1$ for tracks within $|\eta| < 1.62$ and $L = \tan\theta/\tan\theta'$ otherwise, where θ' is the angle the particle left the central tracking detectors.) The overall resolution of the primary interaction vertex location along the beamline, as measured by the central tracking detectors, is 35 μm [36].

Silicon Microstrip Tracker The SMT is composed of high-resistivity silicon sensors arranged on 6 customized barrels and 16 customized disks (Figure 3.4). The size and positioning of these barrel and disks were designed to maximize the detector surface area perpendicular to charged particle trajectories.

The barrels, with an outer radius of $7.5 - 10.5$ cm, provide $r - \phi$ coordinate information for particles at low η ($|\eta| < 1.5$). Each barrel contains 72 silicon modules, termed 'ladders', arranged in four layers. The ladders are composed of either double-sided or single-sided sensors arranged at different stereo angles (2° or 90°) for alternating layers. Although the presence of the stereo angles allows some measurement in z, the barrels are designed primarily for two dimensional reconstruction.

Intercryostat
Detector

Central Fiber Tracker

Central Calorimeter

Solenoidal Magnet

Forward
Preshower
Detector

**Luminosity
Monitor**

DØ
Beam
Pipe

End
Calorimeter

Central Preshower
Detector

Silicon
Microstrip
Tracker
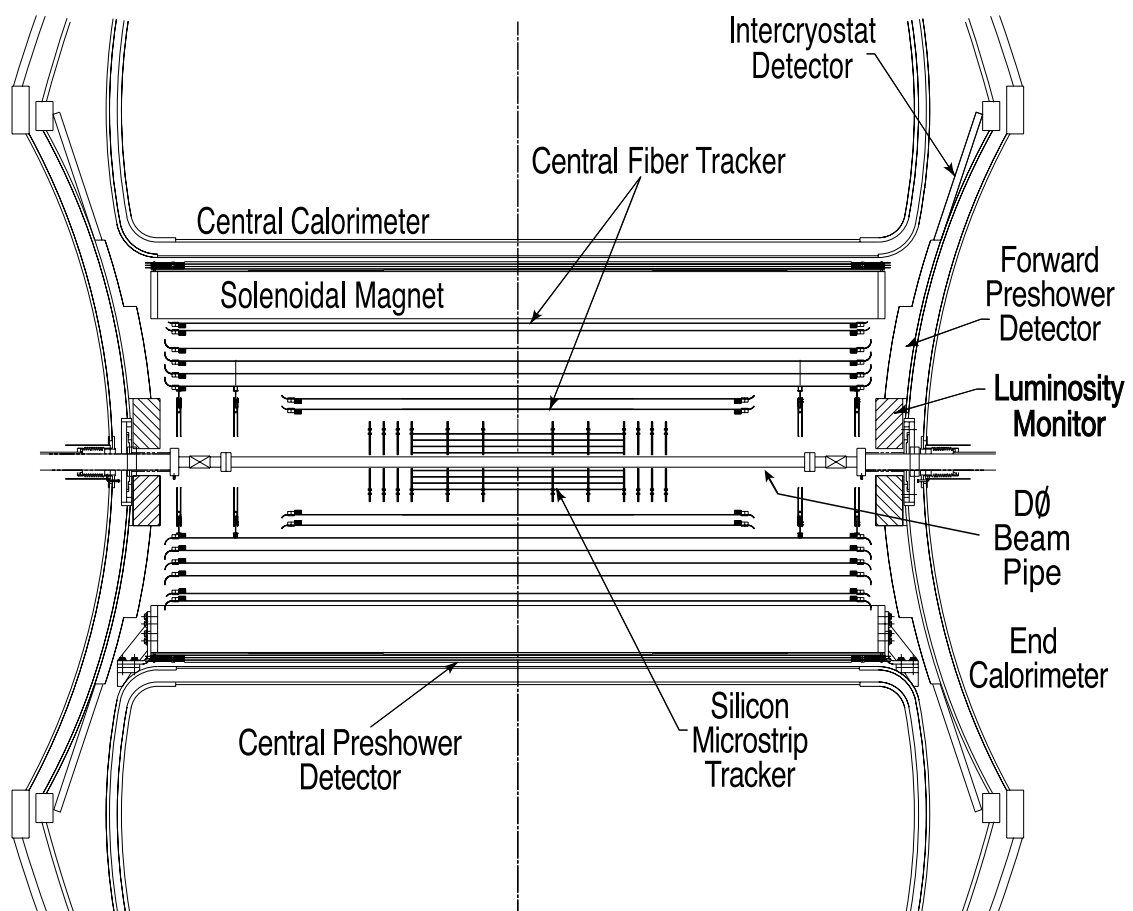
FIGURE 3.3. The central tracking detectors [36].
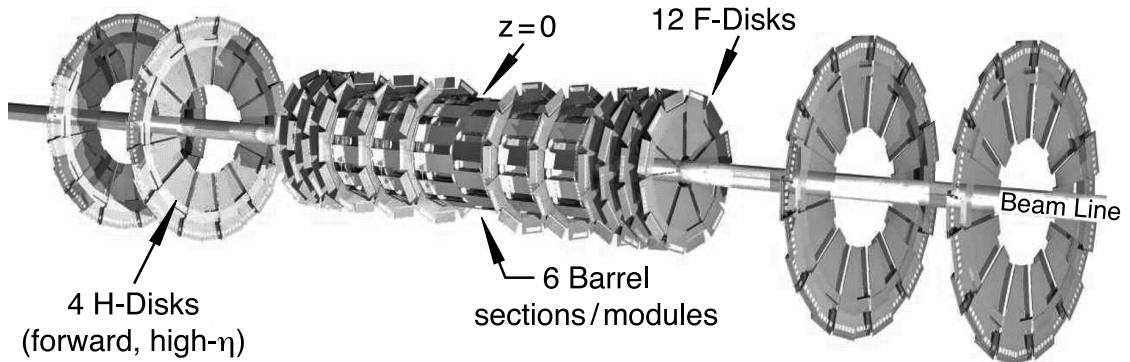
FIGURE 3.4. Barrel and disk assemblies of the Silicon Microstrip Tracker [36].

By contrast, the SMT disks are designed to provide both $r - \phi$ and $r - z$ tracking information for particles. Twelve of the disks, denoted F-disks, have an outer radius of ≈ 10 cm and contain twelve trapezoidal-shaped silicon wedge detectors. Six F-disks cap the barrels, while the other six are divided in two units of three, sitting on either side of the barrel/disk assemblies (Figure 3.4). There are a total of 144 wedge detectors on the F-disks, each double-sided sensors with a stereo angle of $30°$. The other six disks, denoted H-disks, have 24 silicon wedge detectors and are positioned in pairs on either side of the F-disk assemblies. With an outer radius of 26 cm, H-disks are particularly suited to provide tracking information for particles at high η ($|\eta| \leq 3.0$). There are a total of 96 wedge detectors on the H-disks, with an effective stereo angle of $15°$.

Each of the 240 wedge detectors on the disks are read out on both sides. Taking into account these and the 432 silicon modules in the barrels, there are a total of 912 SMT modules to be read out. This is accomplished with 128-channel custom-made SVXEIIe readout chips mounted on the modules. Approximately 800,000 channels are read out on the SMT.

Central Fiber Tracker The CFT fits over the SMT, occupying the radial space of 20 cm to 52 cm from the beampipe center, and providing tracking information for $|\eta| < 1.7$. It consists of ≈ 200 km of scintillating fibers mounted on eight concentric

support cylinders. Each of the support cylinders is 2.52 m long with the exception of the innermost two, which are 1.66 m long in order to accommodate the SMT's H-disks. Two doublet layers of scintillating fibers are mounted on each cylinder. The first layer is an 'axial' layer oriented along z. The second is a stereo layer oriented at alternating stereo angles of $\phi = 3°$ and $\phi = -3°$ if one traverses all the cylinders beginning at the beampipe. Each scintillating fiber has a diameter of 835 μm, and the position resolution of the CFT from the doublets of fibers is $\approx 100\mu$m [36].

When a charged particle strikes a scintillating fiber, light is emitted. Two fluorescent dyes are used in this process. The primary dye, paraterphynol, emits light at a wavelength of ≈ 340 nm. A second dye, 3-hydroxyflavone, absorbs the 340 nm light and re-emits it at 530 nm, a wavelength better suited to transmission in the fibers.

Coupled to the scintillating fibers are 800 km of clear fiber waveguides, $7.8-11.9$ m in length, that transfer the scintillation light to visible light photon counters (VLPCs) for readout. The VLPCs are solid-state silicon photodetectors that convert the scintillation light into electrical signals. VLPCs have high gain with low dispersion, a fast response time, quantum efficiency of over 75%, and they function well in high background environments. The VLPCs are sufficiently sensitive to detect single photons.

The output of the VLPCs is digitized and read out using the same SVXIIe chips used with the SMT. Approximately 77,000 channels are read out from the CFT. Additionally, VLPC outputs are sent to discriminators on the front-end electronics boards that fire when a charge generated from an axial fiber is above a specified threshold. These discriminator outputs are the basis of the Level 1 Central Track Trigger (L1CTT) (Section 3.9). Charged particle trajectories formed from hits in the CFT are segmented into 4.5° sectors in ϕ.

3.2.3 Calorimeter

Immediately surrounding the central tracking detectors is a sampling calorimeter (Figure 3.5). In sampling calorimeters, electromagnetic and hadronic particle showers are induced as particles pass through a dense absorber material. These secondary shower particles ionize an active sampling medium, liquid Argon in this case, between the absorbers, and the resulting ionization charge is collected and used to reconstruct the original particle's energy. The calorimeter is the primary detector responsible for the identification and energy measurement of electrons, photons, and jets. Additionally, the calorimeter can be used to identify neutrinos by making use of transverse energy conservation.

The DØ calorimeter system is actually composed of three separate calorimeters, a central calorimeter (CC) and two endcap calorimeters (EC). The η coverage of the CC is $|\eta| \lesssim 1$. The η coverage of the two endcaps is $|\eta| \lesssim 4$. The use of smaller, individual calorimeters allows access to the central tracking detectors for maintenance and upgrades.

All three calorimeters have three sections, each designed to best measure the energy of different types of particles. The electromagnetic (EM) section employs thin uranium absorber plates for shower-inducing, the fine hadronic (FH) section uses uranium-niobium alloy plates, and the coarse hadronic (CH) section utilizes copper and stainless steel absorber plates in the CC and EC, respectively.

The total depth of the EM section in all three calorimeters is approximately 20 radiation lengths (X_0), divided into four longitudinal layers. Table 3.1 gives the thickness of each of these layers.

In the CC, the fine hadronic section is longitudinally divided into three readout layers, while the coarse hadronic layer is not subdivided. The total thickness of the coarse and fine hadronic layers is approximately six nuclear interaction lengths (γ). In the EC, the three concentric cylinders of hadronic modules—inner hadronic,
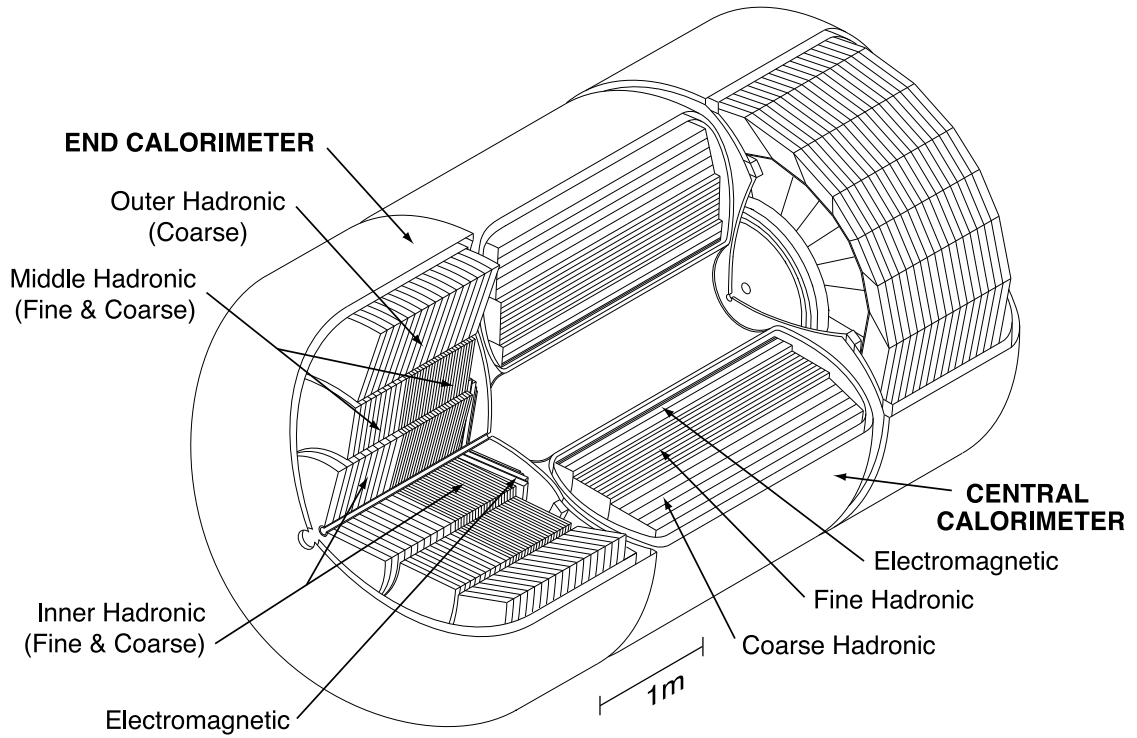
FIGURE 3.5. The DØ calorimeter [36].

Calorimeter	Layer 1 (X_0)	layer 2 (X_0)	Layer 3 (X_0)	Layer 4 (X_0)
Central	1.4	2.0	6.8	9.8
Forward	1.6	2.6	7.9	9.3

TABLE 3.1. $|z|$ thickness of each layer in the EM section of the calorimeter [36].

middle hadronic, and outer hadronic—each have a thickness of six to nine nuclear interaction lengths. The inner and middle hadronic modules are each divided into four fine hadronic layers but only one coarse hadronic layer, while the outer hadronic module has just one coarse hadronic layer.

As illustrated in 3.6, the calorimeter is also transversely divided. These divisions are termed 'pseduo-projective' towers, according to the rays the calorimeter readout cells are oriented along, which project outward from the interaction center. The calorimeter towers are themselves divided into layers of size of $\Delta\eta = 0.1$ and $\Delta\phi = \frac{2\pi}{64} \approx 0.1$. The third readout layer of the EM section, which corresponds to the location of maximum shower deposits, is segmented twice as finely to allow more precise measurements of the EM shower centroid.

Each calorimeter readout cell is composed of one or more unit cells consisting of the appropriate absorber plate, liquid argon gap, and signal board encased in a resistive coating. These resistive surfaces are connected to a positive voltage ($\approx 2\,\mathrm{kV}$) while the absorber plates are grounded, creating the electric field necessary to sample the ionizing particles. Typical electron drift time is 450 ns across 2.3 mm liquid argon gap in each cell. The transverse size of the readout cells is 1–2 cm for EM sections of the calorimeters, and ≈ 10 cm for hadronic showers, which is similar to the transverse size of the relevant shower processes.

Each calorimeter is housed in its own cryostat in order to maintain the liquid argon at an operating temperature of 90 K. This results in gaps of coverage between EC and CC calorimeters, roughly $0.8 < |\eta| < 1.4$. An inner-cryostat detector consisting of a series of scintillating tiles helps to reduce these coverage gaps. Additionally, single-cell calorimeter readout cells, termed massless gaps, are positioned in the intercryostat region of the CC and EC.

The approximate energy resolution for 50 GeV electrons in both the CC and EC is 5%. The approximate transverse momentum resolution for 50 GeV jets is 13% in the CC and 12% in the EC [38].
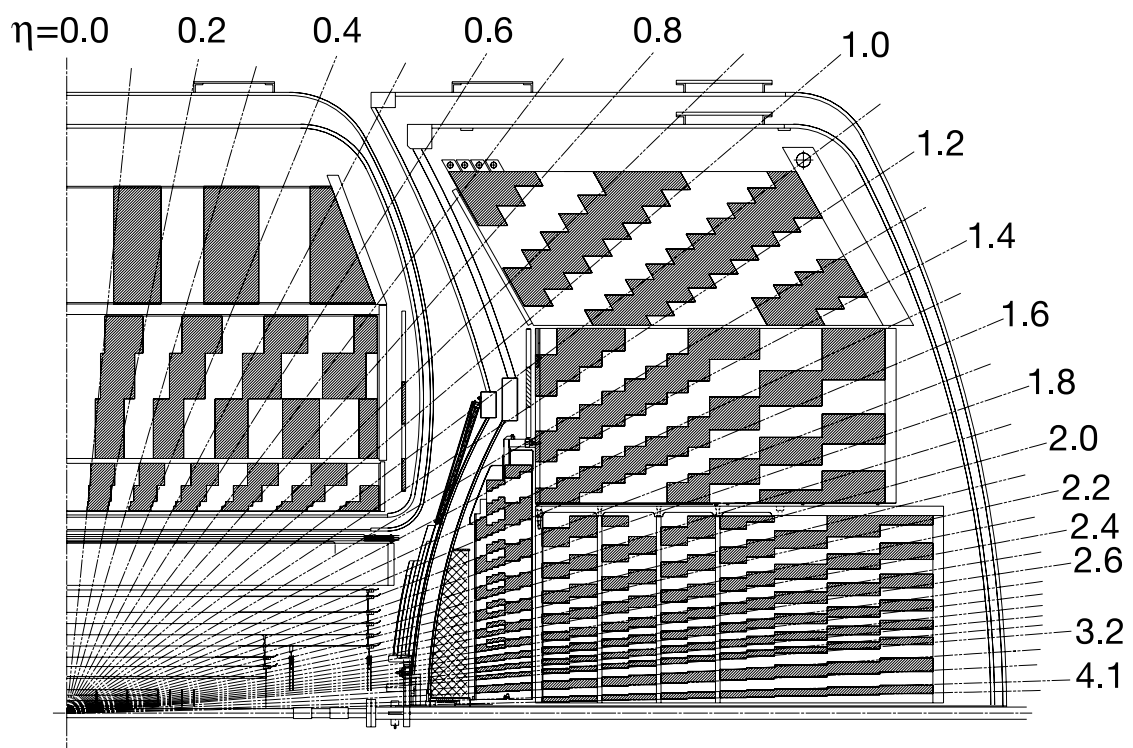
FIGURE 3.6. The DØ calorimeter [36].

Preshower Detectors Three additional detectors, denoted the central (CPS) and forward preshower detectors (FPS), use a combination of scintillation fibers with shower-inducing absorber plates to provide additional triggering capabilities for electrons.

The central preshower detector, which provides coverage to $|\eta| < 1.3$, consists of three triangular scintillator strips arranged in three cylindrical layers with an inner radius of 71.8 cm and outer radius of 74.2 cm. It is located in a 5 cm gap between the solenoid and central calorimeter. A lead radiator is positioned between the solenoid and the CPS. The two forward preshower detectors, north and south, provide coverage from $1.5 < |\eta| < 2.5$. They consist of two layers of scintillating strips with a lead absorber plate between the layers. The FPS detectors are mounted onto the end calorimeter cryostats (Figure 3.2.3). The shower-inducing plates and their location makes the preshower detectors uniquely qualified to measure the energy of electromagnetic objects that start to shower before reaching the calorimeter as well as to make offline corrections to calorimeter energy measurements due to losses in the solenoid or the detector infrastructure. All three preshower detectors employ VLPCs and follow a readout path similar to the CFT.

3.2.4 Muon System

As minimally ionizing particles, muons are not easily identified in the calorimeter. Instead muons are identified in the muon spectrometer, the outermost part of DØ detector. Like the calorimeter, the muon spectrometer is separated into central and forward regions: the central region covers $|\eta| < 1.0$, while the forward region extends this coverage to $|\eta| < 2$. In both regions, a combination of wire chambers that precisely measure the spatial location of the muons and scintillation counters that provide accompanying timing information are used. Exploded views of the wire chambers and the scintillation counters are shown in Figure 3.7 and Figure 3.8, respectively. The muon spectrometer has three layers: A, B, and C with the A-layer

located closest to the center of the detector. A 1.8 T iron toroid magnet is located between layers A and B, accommodating muon momentum measurements that can be matched to the track momentum measurements of the muons in the CFT.

Note that since the momentum resolution of the central tracking detectors is more accurate than that of the muon spectrometer, the muon momentum measurements utilized for offline analysis are taken from the central tracking detectors (Section 3.2.2). Fits that combine the momentum meaurements of the two subsystems have not yielded improved resolution with respect to measurements from the central tracking detectors alone [40].

Central Region The central wire chambers are Proportional Drift Tubes (PDTs), rectangular, aluminum chambers, typically 2.8 m × 5.6 m. PDTs are present in each layer of the muon spectrometer, though only slightly over 50% of the central region has PDTs in all three layers (90% has coverage in at least two layers). PDTs are composed of cells. Each cell houses an anode wire at the center, cathode pads above and below the wire, and is filled with a gas mixture of predominantly argon. As a particle passes through the the cell, electron-ion pairs are created in the gas. These electrons (as well as electrons from electron-ion pairs created in an avalanche initiated by the these electrons) are collected on the anode wire, while the ions are attracted to the cathode pads [39]. The drift velocity of electrons through the chamber is 10 cm/μs, yielding a maximum drift time of $\approx$ 500 ns [36]. This results in a drift distance resolution of about one millimeter, and total hit position measurement resolution between 10 cm and 50 cm, depending on where in the cell the muon hit.

Readout electronics are attached to the end of each PDT chamber. Wires are grouped in pairs for readout within 'decks' of cells. Most of the A-layer PDTs contain four decks of 10.1 cm cells, while layer B and C-layer PDTs have only three. Additionally, all A-layer cathode pads and some B and C-layer PDTs are instrumented with electronics on the cathode pads, to improve the hit position measurements. All

PDTs are oriented to maximize the resolution in the bend angle of the toroid for enhanced momentum measurements.

There are 1002 scintillation counters in the central muon spectrometer: 630 'A-ϕ' counters in the A layer, 240 counters in the 'cosmic cap' on the top of the detector, and 132 counters in the 'cosmic bottom', which includes 16 side counters. Scintillation counters are segmented longitudinally to match PDTs so they can provide precise timing information associated with each wire chamber hit. The counters are likewise segmented to match the CFT segmentation in order to allow muon hits to be matched with CFT tracks. Three sizes of counters are used to keep the constant ϕ segmentation, ranging from 23 cm to 37 cm wide. The timing resolution of the A-ϕ counters is ≈ 2 ns, fast enough to allow out-of-time background rejection.

Forward Region The forward wire chambers are 'mini drift tubes' (MDTs). The operational principle is similar to the PDTs, but MDTs are smaller with an average cell size of 9.4 mm $\times$ 9.4 mm and use a CF4-dominated fill gas. This results in a maximum drift time of 60 ns (even shorter for tracks perpendicular to the detector plane) and a ≈ 700 μm resolution per hit [36]. MDT chambers are present in all three layers of the muon system, and like the PDTs, are arranged in three or four decks depending on the layer. The maximum length of a MDT is 5.8 m in the C layer.

Scintillation counters in the forward system are referred to as pixel counters, and unlike the central counters, pixels provide full coverage in all three layers of the muon spectrometer. Pixels are arranged projectively from the interaction point, with the size varying to accommodate this arrangement from 17 cm $\times$ 24 cm to 60 cm $\times$ 110 cm. Like the central scintillation counters, pixels are segmented in ϕ to match the CFT. They are segmented in η from 0.7 to 0.12 depending on the position of the counter.

For muons with $P_T < 40$ GeV, the overall momentum resolution in the forward muon system is 20% [36].

Proportional
Drift
Tubes

C-layer

B-layer

A-layer

Mini
Drift
Tubes

+y

-x
West

-z
North

+z
South

-y

+x
East
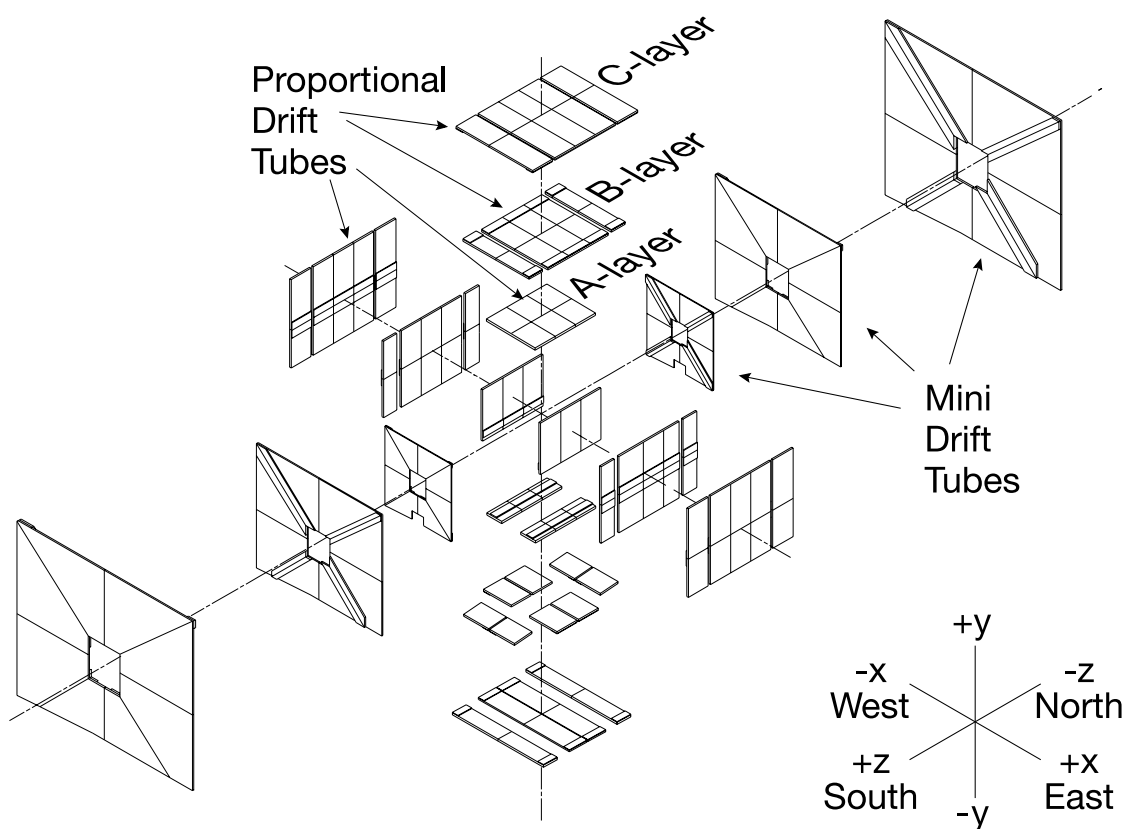
FIGURE 3.7. Exploded view of the wire chambers in the DØ muon spectrometer [36].
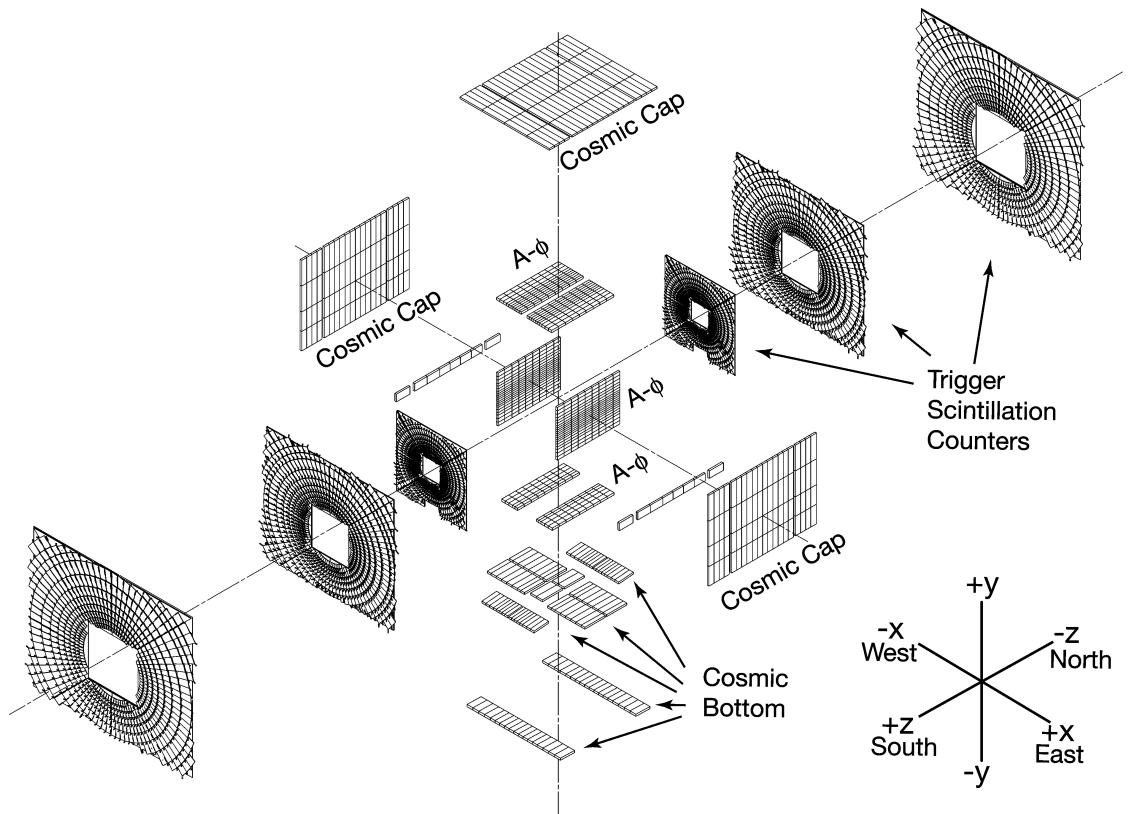
FIGURE 3.8. Exploded view of the scintillation counters in the DØ muon spectrometer [36].

3.2.5 Luminosity Monitor

The luminosity monitor uses two arrays of 24 plastic scintillation counters to measure the luminosity delivered by the Tevatron at the DØ interaction region. The arrays are located in front of the endcap calorimeters at $z\pm$ 140 cm in the radial space between the beampipe and forward preshower detectors. They detect inelastic $p\bar{p}$ collisions in the region $2.7 < |\eta| < 4.4$. The individual counters are 15 cm long and coupled to photomultiplier tubes that send signals to digitization and readout electronics. The luminosity is calculated as:

$$\mathcal{L} = \frac{f\bar{N}_{LM}}{\sigma_{LM}} \tag{3.2}$$

where f is the beam crossing frequency, $\bar{N}_{LM}$ is the average number of inelastic collisions per beam crossing calculated with Poisson statistics from the fraction of beam crossings for which the luminosity monitor detects no collisions, and σ_{LM} is the effective luminosity cross section accounting for the acceptance and the efficiency of the luminosity monitoring detector.

In 2005, the luminosity monitor's readout electronics were substantially upgraded to provide more precise information about hits in the scintillation arrays–specifically timing and pulse height data for individual channels for each triggered bunch crossing– to the data acquisition system [41]. These improvements led to a better measurement of the luminosity monitor's efficiency and acceptance, and ultimately to a modification in the value of σ_{LM} from 54 ± 3.5 mb to 48 ± 3 mb for Run II [41]. This implied an overall increase in the previously assumed value of DØ's Run II integrated luminosity by approximately 15% [41]. This correponds to an integrated luminosity of 421.4±25.7 for this analysis instead of 362.6 ± 23.6 [78, 79].

During operation, data are grouped into 'lumiblocks' that are incremented at every run or store transition, at certain subdetector initializations, or every 60 s. Since the DØ instantaneous luminosity is approximately constant for each lumiblock,

lumiblocks are used as the unit of time for the luminosity measurement.

3.2.6   Trigger System

Because only a small fraction of detector events can be recorded for offline analysis, a triggering system must be used to select interesting physics events. At DØ, this triggering system is three-tiered, with each successive level examining less events but taking into account more information to make its triggering decision.

As discussed in Section 3.1, proton-antiproton collisions occur at the DØ detector every 396 ns, which corresponds to a frequency of over 2 MHz. The Level 1 triggering system reduces this event rate to $\approx$ 2 kHz, using hardware-based triggers that make basic cuts on detector events. Figure 3.9 displays the four Level 1 trigger systems and the subdetectors from which they receive inputs. For example, the Level 1 central track trigger (L1CTT) receives information from the central fiber tracker and central and forward preshower detectors. By requiring tracks in these detectors to have a P_T above a certain threshold, L1CTT can reduce the total number of events that are passed onto Level 2. In order to minimize experimental deadtime, all DØ events are pipelined until they receive a Level 1 trigger decision. Once made, these decisions are sent to the 'trigger framework', the system responsible for making global triggering decisions based on individual Level 1 triggers. A trigger decision is made for each 396 ns accelerator bunch crossing.

Events that pass Level 1 are sent to Level 2, which uses more detailed subdetector information to further reduce the rate by a factor of two to 1 kHz. The system is composed of detector specific pre-processors that combine data from the subdetectors with information from the Level 1 trigger system to form individual Level 2 triggers (Figure 3.9). A global processor, 'L2Global', forms the event-wide Level 2 decisions by identifying correlations in events across detector subsystems.

Events that pass the Level 2 trigger proceed to Level 3, where information about
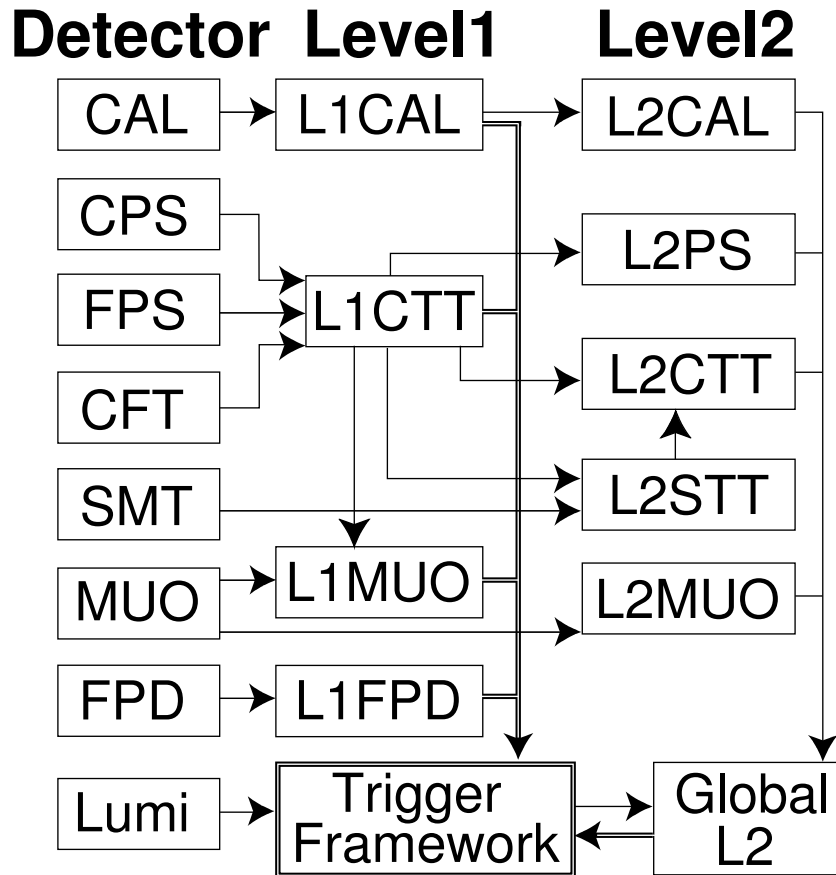
FIGURE 3.9. Two levels of the three-tiered DØ trigger system [36]. The FPD detector is not discussed in this chapter because it is not relevant to the measurement.

the event is reconstructed on a farm of microprocessors. The Level 3 data come directly from the subdetectors, collected and readout in 63 custom VME electronics readout crates. The online event reconstruction includes the reconstruction of four-momenta of physics objects such as electrons and muons as well as variables that relate these objects such as the invariant mass. Complex algorithms and selection criteria, often referred to as 'filters', reduce the event rate to 50 Hz. These remaining 50 Hz of data are then recorded to tape for offline reconstruction and analysis.

CHAPTER 4

EVENT RECONSTRUCTION AND SIMULATION

Before being used in an analysis, the raw data that has been recorded to tape must be reconstructed into physics events complete with defined tracks, a primary vertex, $\not{E}_T$, and the four-momenta of physics objects such as electrons and muons. These events must also be in a form compatible with the analysis framework. This chapter gives an overview of the process through which hit patterns and timing information in the detector become events considered for the measurement. The chapter begins with an overview of data collection and processing, identifying the basic data quality cuts and discussing the online trigger requirement. The offline reconstruction procedure is then detailed for tracks, the primary vertex, muons, jets, electrons, and $\not{E}_T$. Finally an overview of the Monte Carlo samples employed for signal efficiency studies and background yield estimation is presented.

4.1 Data Collection and Processing

The data set for this measurement consists of a total integrated luminosity of $421.4\,\mathrm{pb}^{-1}$ collected between June 2002 and August 2004. DØ*reco* (release version p14), an offline reconstruction program, reconstructed 971,187,179 events for this luminosity [42]. In order to reduce the number of extraneous events, the Common Samples Group at DØ produced several skims (or subsets) of the total data set, by applying different sets of basic selection criteria [43]. This measurement uses the '2MU' skim, which consists of 55,196,992 events that have two or more reconstructed muons [44]. Since the event signature of $t\bar{t} \to \mu\mu$ production includes two high P_T muons, analyzing the 2MU skim instead of the total data set does not eliminate signal events.

Another tool, *top_analyze*, performed basic object identification and quality cuts

Stage	Luminosity (pb^{-1})	Relative %	Absolute %
Delivered	560.75	100%	100%
Recorded	505.32	90.1%	90.1%
Good	425.63	84.2%	76.0%
Reconstructed	421.39	99.0%	75.1%

TABLE 4.1. Integrated luminosity for 2MU data skim [47]. All luminosity values have a 6.1% uncertainty.

on the skim and converted the data into 'rootuples', a form consistent with the analysis framework [45, 46]. The *top_analyze* package was also used for Monte Carlo events, where it performed object smearing and other corrections to account for discrepancies between data and Monte Carlo events. Section 4.3 details the basic object identification criteria and these data and Monte Carlo corrections.

4.1.1 Data Quality

Two code packages were used to perform overall data quality cuts on the 2MU skim: *top_dq* and *top_dq_data* respectively [78]. These packages flag runs, subsets of the data set typically representative of a few hours of data collection, and luminosity blocks (Section 3.2.5) that are considered unsuitable for analysis.

Runs are evaluated with DØ's run quality database, in which hardware experts label each run 'good', 'reasonable', 'unknown', or 'bad' based on how their subdetector was functioning at the time the run was recorded [48]. For this measurement, runs are excluded from the data set if any subdetector (SMT, CFT, CAL, MUO) marked them as bad or if the muon subdetector failed to actively mark them as good or reasonable, where reasonable indicates a basic level of acceptability for for analysis.

Luminosity blocks are marked as bad if specific patterns of calorimeter noise are present or if other known problems that significantly impact $\not{E}_T$ reconstruction (Section 4.3.6) are detected. Rejection by luminosity block is preferable to run rejection because a luminosity block represents a smaller increment of time, and therefore,

Trigger List	Luminosity (pb^{-1})
v10 and earlier	59.54
v11	66.54
v12	243.82
v13	51.49
total	421.39

TABLE 4.2. Integrated luminosity by trigger list version. [38, 49]. All luminosity values have a 6.1% uncertainty.

rejection by lumiblock preserves a significantly higher fraction of the data [45]. Table 4.1 shows the breakdown of luminosity delivered, recorded, and reconstructed after data quality cuts have been applied for the 2MU skim.

The final data quality cut, applied after *top_dq* and *top_dq_data* is the removal of any duplicate events.

4.2 Trigger Requirement

Events considered for this measurement are required to have fired one of a list of muon triggers, each of which has a different set of Level 1, Level 2, and Level 3 trigger requirements (Section 3.9). In general, two groups of triggers are considered: single muon triggers and dimuon triggers. As expected, they require one or two muons to be present in the event to fire respectively. Triggers are further grouped according to 'trigger list version'. Trigger list version numbers were incremented monotonically during Run II each time a change in the trigger requirements was made. Such changes occurred regularly to accommodate varying beam conditions, and often resulted in the set of triggers available for the analysis changing. For the data set we consider, triggers are grouped into four trigger lists: v10 and earlier, v11, v12, and v13. The integrated luminosity associated with each trigger list is given in Table 4.2.

Since this analysis requires two reconstructed muons, it is intuitive to require dimuon triggers to fire in order for the event to be considered for the measurement.

Previous passes of the analysis all included this requirement [49, 50, 51]. However, this measurement implements a looser set of offline muon identification requirements than the previous ones, which renders the dimuon triggers disadvantageous. Specifically, the muons required for this measurement can be formed from detector hits either inside or outside the muon toroid as opposed to both (Section 4.3.3). By contrast, the dimuon triggers require two muons formed from matches in hits both inside and outside the toroid. Thus, the dimuon trigger imposes unnecessarily tight muon identification criteria, resulting in a loss of signal efficiency.

Single muon triggers also require tight muon identification requirements. However, single muon triggers only require one muon to fire so the efficiency loss is less severe. Unfortunately, single muon triggers also have a disadvantage. The trigger rate of single muon triggers can be sufficiently high that a scale factor has to be applied during data acquisition in order to satisfy the bandwidth of the Level 1 trigger system. Such triggers are said to be 'prescaled'. Prescaled triggers are undesirable because a large fraction of good events are not accepted. In this analysis, the following compromise is made. For a given event, if the designated single muon trigger is unprescaled, it is required to fire for the event to pass data selection. Otherwise, the specified dimuon trigger is required to fire.

4.2.1 Single Muon Triggers

In order to minimize the luminosity for which the more restrictive dimuon trigger is required, the set of least prescaled single muon triggers is chosen. Identifying these triggers is a multi-step process. First, a comprehensive set of likely single muon triggers is constructed for each of several groupings of trigger list versions. Next, the *top_trigger* package is used to determine the set of runs for which each trigger is unprescaled [52]. Finally, the luminosity associated with each set of runs is calculated with the *top_dq_data* package, and the single muon trigger with the greatest

unprescaled luminosity is chosen for each trigger list grouping.

In total, nine v11 and earlier triggers, fifteen v12 triggers, and eleven v13 triggers are examined. Two triggers in the v13 trigger list have the same unprescaled luminosity so the trigger that is simpler to simulate is selected. The trigger with the greatest unprescaled luminosity in the v11 and earlier trigger lists and the v12 trigger list is the same and is therefore selected for both trigger lists. The requirements of the two selected single muon triggers are summarized in Table 4.3.

At Level 1, both triggers require a muon with scintillator hits both inside and outside the toroid (referred to as 'tight' scintillator triggers). These scintillator hits must also be confirmed by wire hits inside the toroid magnet ('loose' wire triggers) [54]. For the MUW_W_L2M3_TRK10 trigger, hits in the muon detectors must take place within $|\eta| = 1.6$ (the 'wide' range), while for MUH2_LM15, hits can occur to $|\eta| = 2$ (the 'all' region). A 10 GeV central track is also required for the MUH2_LM15 trigger to fire. At Level 2, both triggers require a medium muon (Section 4.3.3) with a minimum P_T of 3 GeV. At Level 3, a 10 GeV track or 15 GeV muon is required.

4.2.2 Dimuon Triggers

When the the designated single muon trigger is prescaled, the trigger requirement reverts to the dimuon trigger. The dimuon trigger requires two muons at Level 1 that have been formed from scintillator hits inside and outside the muon toroid, but unlike the single muon triggers, no wire hits are required. At Level 2, a medium muon is required. For the version 10 trigger list, the dimuon trigger has no Level 3 requirements. For trigger lists v11-v13, Level 3 requirements are added to this trigger in order to keep rates sufficiently low that the triggers can remain unprescaled. A logical *OR* of complementary triggers with different Level 3 requirements is implemented to keep the overall trigger efficiency in signal events as high as possible. Table 4.4 summarizes the requirements of the dimuon trigger.

Trigger List	Name	Level 1	Level 2	Level 3
$\leq$ v12	MUW_W_L2M3_TRK10	mu1ptxwtlx	1 medium μ $P_T >$3 GeV	1 track, $P_T >$10 GeV
v13	MUH2_LM15	mu1ptxatlx + 1 track $P_T >$ 10 GeV	1 medium μ $P_T >$3 GeV	1 μ, $P_T >$15 GeV

TABLE 4.3. Single muon trigger requirements. Level 1 terms are expressed as mu{N}pt{V}{R}{S}{W}x where N=1 for single muon triggers and N=2 for dimuon triggers, V is the P_T threshold, R is the η region of the trigger ('wide' or 'all'), S is the scintillator requirement ('tight' or 'loose'), W is the wire hit requirement ('tight' or 'loose') [53].

Trigger List	Name	Level 1	Level 2	Level 3
v10 and earlier	2MU_A_L2M0	mu2ptxatxx	1 medium μ	*none*
v11	2MU_A_L2M0_L3_l15	mu2ptxatxx	1 medium μ	1 μ, $P_T > 15$ GeV
	OR			
	2MU_A_L2M0_L3TRK10	mu2ptxatxx	1 medium μ	1 track, $P_T > 10$ GeV
v12	2MU_A_L2M0_L3l6	mu2ptxatxx	1 medium μ	1 μ, $P_T > 6$ GeV
	OR			
	2MU_A_L2M0_L3TRK5	mu2ptxatxx	1 medium μ	1 track, $P_T > 5$ GeV
v13	DMU1_LM6	mu2ptxatxx	1 medium μ	1 μ, $P_T > 6$ GeV
	OR			
	DMU1_TK5	mu2ptxatxx	1 medium μ	1 track, $P_T > 5$ GeV

TABLE 4.4. Dimuon trigger requirements. Level 1 terms are expressed as mu{N}pt{V}{R}{S}{W}x where N=1 for single muon triggers and N=2 for dimuon triggers, V is the P_T threshold, R is the η region of the trigger ('wide' or 'all'), S is the scintillator requirement ('tight' or 'loose'), W is the wire hit requirement ('tight' or 'loose') [53].

4.3   Object Reconstruction

The experimental signature of a $t\bar{t} \rightarrow \mu\mu$ event consists of two high P_T muons, two high P_T jets, and significant missing transverse energy from the neutrinos. In order to select signal events from data, each of these physics objects must be reconstructed. Reconstruction involves converting patterns of detector hits into four-momenta of physics objects and making the appropriate corrections in data. When significant disagreements occur between the resolution of these objects in data and Monte Carlo events, the Monte Carlo events must be smeared or scaled to match the data. The process of reconstruction and smearing for tracks, the primary vertex, muons, jets, and $\not{E}_T$ is now discussed. Although electrons are not directly used in the dimuon analysis, a veto on events containing electrons is applied in order to obtain orthogonality with the other two topological decay channels, $t\bar{t} \rightarrow ee$ and $t\bar{t} \rightarrow e\mu$. For this reason, a brief synopsis of electron identification is included here.

4.3.1   Track Reconstruction

Two complementary approaches are used to reconstruct energy deposits, or hits, from the central tracking detectors into charged particle trajectories, called tracks. The first is a histogramming method that performs well for high P_T tracks near the primary vertex. The second is an SMT cluster approach that has a better efficiency for low P_T tracks. Separate candidate lists are created for each method and then combined, with duplicate candidates removed before proceeding to the final step in track reconstruction, the track-fitting algorithm [55, 56].

The histogramming approach is based on the Hough Transform. This technique, first used to find tracks in bubble chambers, maps the (x,y) coordinates of hits in the central tracking detectors into a binned track parameter space defined by coordinates (ϕ, ρ), where ϕ is the direction of the track at the point of closet approach, and ρ is the curvature defined as $\rho = \frac{qB}{P_T}$ [57]. Here q is the charge of the particle, and B

is the strength of the magnetic field from the solenoid. Once mapped, a coordinate hit is represented by a band in parameter space. After all hits have been mapped with their uncertainties, the intersection of the resulting bands should correspond to the real track's parameters. This is quantified by histogramming the bands over the entire detector where candidate tracks appear as local maxima. In order to account for hits in stereo layers of the CFT or SMT disks (Section 3.2.2) the process is repeated, now mapping (r,z) coordinates to the parameter space and adding the resulting information to the track candidates.

The SMT cluster approach begins by fitting three $r - \phi$ hits in the SMT barrels or F-disks to a track hypothesis, and using the results of the fit to predict the location of other hits in the surrounding modules. This process is termed forming 'roads'. Hits in neighboring modules consistent with the fit are added to the track candidate. As in the histogramming approach, stereo hits associated with $r - \phi$ hits are used to reconstruct the tracks in three dimensions. Once a set of tracks is identified, the primary vertex is reconstructed. The primary vertex is then used to predict the location of hits in the CFT. If the predicted CFT hits are found, they are also added into the track.

The second step in track reconstruction is to input all track candidates into a track fitter that propagates them through the DØ detector, and modifies their momenta to account for interactions with detector material and curvature from the magnetic field. The Kalman Track fitter is used for this step [58]. The Kalman technique effectively produces optimal track parameters for any surface, making it ideal to simulate both the cylinders of the CFT and the planar geometry of the SMT.

4.3.2 Primary Vertex Reconstruction

Interaction vertices are constructed from tracks in a straightforward way. The challenge of reconstructing the 'primary event vertex' is to distinguish the vertex asso-

ciated with the hard scatter event from the vertices associated with superimposed minimum bias events that also result from $p\bar{p}$ collisions [59].

To complete this task, the list of candidate tracks (Section 4.3.1) are inputted to the DØ*root* primary vertex-finding algorithm [49]. Two variables are computed for the candidates tracks: the distance of closest approach, DCA, which is the $x - y$ planar distance of the track to the beam spot, and the significance, S, defined as:

$$S = \frac{DCA}{\sigma_{DCA}}. \tag{4.1}$$

where σ_{DCA} is the uncertainty in the DCA.

At first, only a loose cut on the tracks is made. Specifically, any track with $S \geq 100$ is cut from the candidate list. Event vertices are reconstructed for all remaining tracks. Since only a loose track cut was made, this provides a comprehensive set of primary event vertex candidates.

Next, the significance of each of the track candidates is computed with respect to each event vertex (as opposed to the beam spot). Any tracks with $S \geq 3$ or with less than two SMT hits are removed from the list of candidates. New vertices are then reconstructed from the updated, more refined track list. Finally, the transverse momenta of these tracks is used to calculate the probability that the vertex originated from a minimum bias event. The vertex with the lowest probability is chosen as the hard scatter vertex, and labeled the primary event vertex [59, 60].

For this analysis, several quality cuts are imposed on the primary vertex. It is required to have a certain number of associated tracks, and its z coordinate must be sufficiently close to the center of the detector.

These cuts can be summarized as:

- $N_{tracks} \geq 3$

- $|z_{PV}| < 60$ cm

- $|\Delta z(DØroot, DØreco)| < 5$ cm

4.3.3   Muon Reconstruction

As discussed in Section 3.2.4, muons are detected both in the central tracking detectors and in the muon spectrometer. Quality cuts are applied to reconstructed muons to ensure that the muons used in the analysis originated from the hard scatter process.

The starting point for muon reconstruction is the formation of stubs, straight-line segment hits in the muon system that contain both a wire chamber hit and a muon scintillator hit [38]. Stubs can be constructed on either side of the iron toroid, that is, in layer A or in layers BC. If A-layer stubs are consistent with BC-layer stubs, taking into account the trajectory bend and multiple scattering caused by passage of the muon through the toroid, the stubs are combined to form a 'local' muon. Local muons can be paired with tracks (Section 4.3.1) by matching the track's direction with the muon's direction as measured from the trajectory at the inner surface of the muon spectrometer and matching the track's momentum with the muon's momentum as measured independently in the muon spectrometer from the bend angle through the toroid.

Single layer stubs can also be matched to tracks. Since there is no momentum measurement available from the muon spectrometer for single layer stubs, A-layer stubs are matched based only on direction. BC-layer stubs are matched using direction and a rough estimate of momentum calculated by assuming the muons originated from the primary event vertex. A reconstructed muon, then, consists of either a local muon matched to a track, or a stub-track pair.

Reconstructed muons are categorized according to the location and types of hits in the muon system. These classifications are referred to as 'tight', 'medium', and 'loose'. The selection criteria for this analysis requires all signal events to have two loose quality muons, where the loose classification means that the wire and scintillator hits forming a stub can be either inside or outside the toroid. That is, the muon could have been constructed from a stub-track match rather than from a local muon-track

match. Tight muons, which are required for certain muon identification and trigger studies, are required to have wire and scintillator hits both inside and outside the toroid, and result from a local muon-track match [40]. The medium muons required by the single and dimuon triggers (Section 3.9) typically are formed from wire and scintillator hits outside the toroid, though this requirement is relaxed in the bottom region of the detector. A complete description of the muon classification system is given in [40].

As with the primary event vertex, a series of quality cuts are made on the muons, in this case to distinguish signal muons from non-signal muons. Signal muons originate from W boson decay. Other sources of muons include cosmic rays, heavy flavor decay (from bottom and charm quarks), π/K decay and combinatorics. Occasionally, hadronic energy is deposited in the muon system either because a hadron did not interact with the calorimeter or because of debris from a hadronic shower. Such deposits in the muon system are referred to as punchthroughs since the hadron or decay products had to punch through the calorimeter. The muon identification cuts are designed to target each of these alternate sources of muons.

To reduce cosmic ray contamination, the scintillator hits associated with the muon are required to have occurred at the appropriate amount of time after a live bunch crossing consistent with the time of flight of a muon originating at the primary event vertex. In order to ensure that the muons are associated with the hard scatter event, a maximum is imposed on the χ^2 of the track Kalman fit discussed in section 4.3.1. A cut is made on the significance of the distance-of-closest approach, defined in Section 4.3.2, and a limit is placed on the z distance between the muon and the primary vertex. To reduce the incidence of poorly reconstructed muons, muons are required not to have been reconstructed from the lower sections of the detector with poor coverage. These sections are referred to as the bottom hole (Figure 3.7 and Figure 3.8).

Finally, muons are required to be well isolated. There should not be significant energy deposits in the cone around the muon path, which could indicate a non-top

event such as a heavy flavor or π/K decay in a jet. Two isolation variables are defined. Both take the sum of the ratio of the energy in the area around the muon to the P_T of the muon. The first takes this sum in the tracking detectors and the second in cells in the calorimeter. The variables are defined as:

$$\mathcal{E}_{halo}^{trk} = \sum_{\Delta R < 0.5} \frac{p_T^{trk}}{p_T^{\mu}} \tag{4.2}$$

$$\mathcal{E}_{halo}^{cal} = \sum_{0.1 < \Delta R < 0.4} \frac{E_T^{cell}}{p_T^{\mu}} \tag{4.3}$$

where $\Delta R = \sqrt{\Delta\eta^2 + \Delta\phi^2}$. In a non-top event the energy surrounding the muon may be comparable to the energy of the muon. To suppress these backgrounds, a maximum value is imposed on these variables.

A summary of the muon identification cuts used in this analysis are:

- loose quality

- match to Level 1 and Level 2 trigger requirements (Section 4.2)

- timing cuts against cosmics

- central track match, $\chi^2_{track} < 4$

- low DCA significance: $|DCA|/\sigma_{DCA} < 3$

- $|\Delta z(\mu, PV)| < 1$ cm

- $\mathcal{E}_{halo}^{trk} < 0.12$

- $\mathcal{E}_{halo}^{cal} < 0.12$

- $|\eta_{detector}| < 2$

- bottom hole rejection, where the bottom hole is defined by: $4.25 < \phi < 5.15$ when $|\eta_{detector}| < 1.25$

In order to ensure that the muon momentum resolution is the same in data and the Monte Carlo events, Monte Carlo is smeared such that the mean position and width of the $Z \to \mu\mu$ peak is approximately the same in data and Monte Carlo (Section 4.4.2). The smearing is parameterized in inverse P_T according to:

$$\frac{1}{P'_T} = \frac{1}{\alpha P_T} + \xi \tag{4.4}$$

where α represents a scale factor, and ξ represents a random-variable Gaussian correction. The width of the Gaussian, σ_ξ, and α are determined using the Kolmogorov-Smirnov distribution separately for central and forward muons [45]. The smearing parameters chosen for central muons are $\sigma_\xi \simeq 0.0023$ GeV^{-1} and $\alpha = 0.991$. For forward muons, the smearing parameters are given by: $\sigma_\xi \simeq 0.0047$ GeV^{-1} and $\alpha = 0.999$.

4.3.4 Jet Reconstruction

This analysis requires two high P_T jets, which are reconstructed from energy deposits in calorimeter cells. The first step in jet reconstruction is to distinguish noisy cells in the calorimeter from cells with energy deposits from physics objects. This is accomplished with the 'T42' algorithm. The algorithm requires the energy deposited in a calorimeter cell to be at least 4σ (where σ is the mean width of noise in the cell) or to be 2.5σ with a direct neighbor cell that is 4σ [61]. Any cell failing these criteria is excluded from the calorimeter towers (Section 3.2.3).

After noisy cells are removed from the towers, the 'legacy cone algorithm is applied'. All calorimeter towers with transverse energy > 1 GeV and that are within a cone of radius $\Delta R = 0.3$ (where $\Delta R = \sqrt{(\Delta y)^2 + (\Delta \phi)^2}$) of each other are joined together in groups called pre-clusters. Next, the minimum distance, R_{min}, between these pre-cluster groups and a P_T−ordered list of calorimeter towers, termed proto-jets, is calculated. If $R_{min} < \frac{R_{cone}}{2}$ (for $R_{cone} = 0.5$), these towers are considered

seeds for the proto-jets and all the towers inside the cone with positive energy are included to form updated proto-jets. This procedure is repeated multiple times. Once stable proto-jets have been formed, the algorithm searches for new proto-jets in the midpoints between the existing proto-jets. This is termed 'midpoint addition'. In the final step, 'merging and splitting', decisions are made to either merge or split proto-jets that share energy in order to prevent double counting. If the shared P_T is less than 50% of the lower P_T jet, the energy is split, otherwise proto-jets are merged. These proto-jets become jet candidates [62, 63].

Several variables are defined in order to differentiate jets from electromagnetic (EM) objects, or fake jets that are reconstructed as candidate jets because of noise or other instrumental effects. Variables used to suppress fake jets include the following. The course hadronic fraction, f_{CH}, is the fraction of a jet's energy that is deposited in the outer layers of the calorimeter. The outer layers are noisier then the inner layers. The hot fraction, f_{hot}, is the fraction of energy of the most energetic jet cell to the next-most-energetic jet cell. A high value of f_{hot} could be an indication of a *hot* cell in the calorimeter that is frequently firing. N_{90} is the number of cells that together collect 90% of the jet's energy. If this number is one, it is likely a hot cell. Finally the ratio of energy readout by the L1Cal trigger (Section 3.2.6) to the precision readout of E_T is computed, $f_{L1 \sum E_T}$. If this number is small, it indicates a mismatch in the energy readout that could be an indication of noise.

In order to discriminate jets from EM objects and further discriminate them from noise, the ratio of the total energy in the EM layers to the total energy in the cluster, called the EM fraction, f_{EM}, is computed. Jets in the far forward region are removed in order to reduce the number of jets originating from low energy multiple interaction events.

Finally, it should be noted that all jets are also reconstructed as EM objects, and if they pass EM object identification, they are removed from the jet list in order to avoid double counting.

The specific selection criteria used for this analysis are summarized below:

- $f_{CH} < 0.4$

- $f_{hot} < 10$

- $N_{90} > 1$

- $f_{L1 \sum E_T} > 0.4$ ($|\eta| < 0.7$)

- $f_{L1 \sum E_T} > 0.2$ ($0.7 < |\eta| < 1.6$)

- $|\eta| < 2.5$

- $0.05 < f_{EM} < 0.95$

Several data and Monte Carlo corrections are also applied to jet candidates. One such correction is a data-to-Monte Carlo scale factor applied to Monte Carlo jet candidates to compensate for differences in jet identification and reconstruction efficiencies. This correction factor, termed 'Jet ID', is measured in $\gamma + jet$ events separately for jet candidates in the central calorimeter, endcap calorimeter, and the intercryostat detector regions. A second data-to-Monte Carlo scale factor is applied to account for differences in the jet energy resolution. This was measured using both dijet and $\gamma + jet$ events and is aptly referred to as 'jet energy resolution'.

The largest set of corrections, applied to both data and Monte Carlo, is made to restore the measured jet energy, E_{jet}^{meas}, to an estimate of the actual jet's energy, $E_{jet}^{particle}$. These corrections, called Jet Energy Scale corrections (JES), are applied as [64]:

$$E_{jet}^{particle} = \frac{E_{jet}^{meas} - O}{R \times S} \tag{4.5}$$

- **O** is the offset energy from electronic noise, noise from radioactive decay of the uranium in the calorimeter, multiple interactions, underlying event energy from the interactions of the non-hard scatter processes in proton-antiproton collisions, and energy from proton-antiproton collisions from other bunch crossings (pile-up).

- **R** is a measure of the calorimeter response for jets. This is less than one because of energy lost in the detector before the calorimeter, imperfections in the calorimeter, and the poorer response of calorimeters to hadrons than electrons.

- **S** accounts for jet energy that is deposited outside of the jet cone due to showering as well as energy deposited inside the jet cone from the showers of particles other than the jet.

These variables are measured in unbiased data events, specifically $\gamma + jet$ events and dijet events.

The jet energy scale corrections are the largest source of systematic uncertainty in this analysis. The corrections as functions of η_{jet} and uncorrected jet energy E_{jet}^{uncorr} are shown for both data and Monte Carlo in Figure 4.1. The *JetCorr* v5.3 package is used to apply jet energy scale corrections for this analysis [49].

4.3.5 Electron Reconstruction

Because electrons are identified in the calorimeter, their reconstruction is similar to that of jets. First, the T42 algorithm is applied to remove noisy cells from calorimeter towers (Section 4.3.4). The next step in electron reconstruction is the use of an algorithm that forms electromagnetic 'clusters' based on towers in the electromagnetic section of the calorimeter. These towers, referred to as 'seed' towers, have $P_T >$ 500 MeV. Neighboring towers with $P_T > 50$ MeV and within a cone of radius $R = 0.3$
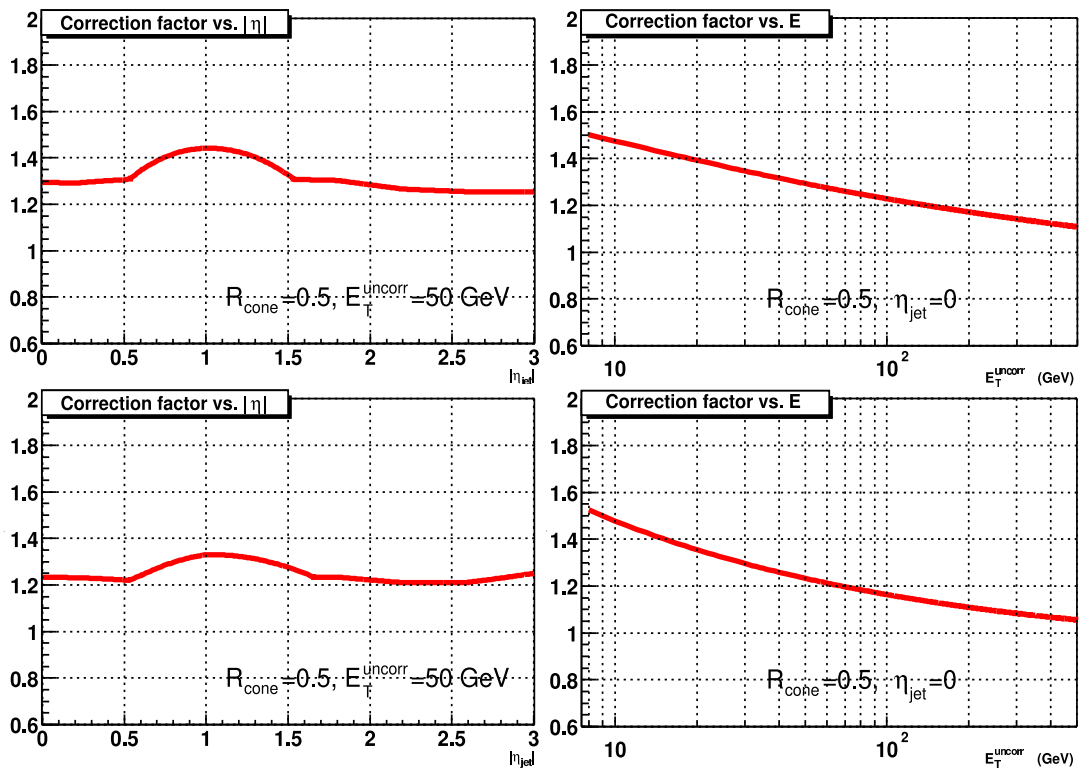
FIGURE 4.1. Examples of jet energy scale corrections for data (top) and Monte Carlo (bottom) [64]. The JES corrections are plotted as a function of η_{jet} (left) and E_{jet}^{uncorr} (right).

in the CC, where R is defined as $R = \sqrt{(\Delta\eta)^2 + (\Delta\phi)^2}$, are included in the cluster. Clusters with $P_T > 1$ GeV are used as inputs in a second algorithm that continues to add EM towers within a cone of $R = 0.4$.

A series of variables are defined to test the consistency of a cluster with an electron. The first is the EM fraction, f_{EM}, defined in Section 4.3.4. Another is the degree of isolation of an EM cluster, termed f_{iso}. A shower shape variable is defined that tests the consistency of the cluster's shower with the hypothesis that it is an electron. This is a χ^2 variable, termed hmx_8 because it combines information from eight variables. And finally, a probabilistic electron likelihood is defined based on seven variables including f_{EM}, the quality of the track match, the association likelihood of the track with the primary vertex, and the ratio of transverse energy in the calorimeter to the momentum of the track.

For the purpose of the electron veto in this analysis, the following requirements are made to define an electron:

- $f_{EM} > 0.9$

- $f_{iso} < 0.15$

- $hmx_8 > 50$

- Likelihood > 0.85 in both CC and EC

Finally, our electron candidates are also required to have a high transverse momentum, $P_T > 15$ GeV, and to have a track match.

The choice of values for each selection cut and the testing of electron reconstruction algorithms were conducted with various data samples. More detail can be found at [49, 65]. As for Monte Carlo muons, electron momenta are smeared in order to account for differences in the electron momentum resolutions between data and Monte Carlo events.

4.3.6 Missing E_T Reconstruction

Since neutrinos are weakly interacting particles, they are not directly measured in the detector. Instead the total transverse momentum of all visible particles in the event is vectorially summed. The P_T needed to balance this sum should represent the energy of the neutrino. Of course, imperfect object resolutions, detector noise, and other instrumental effects make this reconstruction imperfect.

Reconstructing $\not{E}_T$ starts by vectorially adding all the energy deposits in the electromagnetic and fine hadronic layers of the calorimeter for each tower above a certain minimum threshold [38]. This threshold helps reduce the amount of noise entering the sum. If energy deposited in the coarse hadronic layers is associated with a jet it is also included. The inverse of this first vector sum, that is a vector of the same magnitude pointing in the opposite direction, is referred to as the raw missing transverse energy, $\not{E}_{Traw}$.

Several adjustments are made to calculate the $\not{E}_T$ from $\not{E}_{Traw}$. As discussed in Section 4.3.4, the measured jet energy in the calorimeter is not the true jet energy so jet energy scale corrections are applied. Smaller, but similar corrections are made for EM objects. Therefore, in order for the $\not{E}_T$ to reflect the missing energy of the real jets and EM objects, these jet and EM energy scale corrections must be vectorially subtracted from the $\not{E}_{Traw}$. The updated quantity, referred to as calorimeter $\not{E}_T$, is closer to the true $\not{E}_T$. However, a sum based on calorimeter energy deposits does not account for muon momenta, since muons are minimally ionizing in the calorimeter. The final step, then, is to vectorially subtract the measured momenta of all muons passing identification cuts from the calorimeter $\not{E}_T$. This $\not{E}_T$ is the $\not{E}_T$ employed in selection criteria.

4.4   Event Simulation

This analysis depends on simulated events to calculate selection cut efficiencies in signal and estimate signal and background yields. Monte Carlo samples are employed for this purpose. Monte Carlo simulators contain parton generators that describe the physics, parton distribution functions that describe the momentum distribution of partons, and a hadronization scheme to turn partons into particles. These are then passed through a simulation of the DØ detector that models detector response and acceptance. This section provides a brief overview of the Monte Carlo samples utilized in this analysis.

4.4.1   Signal Monte Carlo

The signal sample of $t\bar{t} \rightarrow \mu\mu$ events is generated with the Alpgen Monte Carlo generator, which uses exact leading-order matrix elements [66]. The parton distribution functions are modeled with CTEQ5L [67] while parton showering, fragmentation, and decay are modeled with Pythia [68]. The parton level cuts used in generation are termed 'CAPS' for 'Common Alpgen + Pythia Study'. They are:

- $|\eta| < 10$ for leptons

- $P_T > 8$ GeV & $|\eta| < 3.5$ for jets

- $\Delta R(jet, jet) > 0.4$

- factorization scale: m_{top}^2

B-meson decays are simulated with EVTGEN [69], and the τ decays are modeled with TAUOLA [70].

This sample is normalized for selection cut studies assuming a $t\bar{t}$ production cross section of 7 pb. The sample also assumes a top quark mass, $m_{top} = 175$ GeV. Samples assuming different values of the mass are used to determine the dependence of the

Process	Generator	PDF	N_{events}	$\sigma \times BR$ (pb)
$t\bar{t} \to \ell\ell$	Alpgen	CTEQ5L	16,796	$7 \times 0.01571 \pm 0.00031$

TABLE 4.5. Monte Carlo $t\bar{t}$ sample used for measurement. Here N_{events} is the number of events that are tagged as decaying to dimuon final states. The original sample had 110,000 events. The cross section and the branching ratio ($\sigma \times BR$) are used to normalize the Monte Carlo yield for selection cut studies (Section 5.3.2) [33].

cross section measurement on the mass of the top quark (Figure 7.4). Table 4.5 describes the signal Monte Carlo sample.

4.4.2 Background Monte Carlo

The background processes considered in this analysis include:

- $WW + jets \to \mu\mu + \nu\nu + jets$, $WZ + jets \to \mu\mu + \nu + jets$

- $Z/\gamma^* + jets \to \tau\tau + jets \to \mu\mu + \nu\nu\nu\nu + jets$

- $Z/\gamma^* + jets \to \mu\mu + jets$

- multijet production and W+jets events

All but the last of these backgrounds is estimated with Monte Carlo (Chapter 6).

Diboson Processes All samples corresponding to the diboson processes, $WW + jets$ and $WZ + jets$ events (Table 4.6), are produced with the Alpgen generator. Parton distribution functions are modeled with CTEQ4L [67]. No parton cuts are applied. Otherwise parton modeling and decays are carried out in the same manner as for the signal Monte Carlo. Diboson samples are normalized to their theoretical next-to-leading order cross sections [51]. For the WW$jj \to \ell\nu\ell\nu jj$ sample, the NLO cross section is unavailable. Since the NLO cross section is 35% higher than the LO cross section for WW$\to \ell\nu\ell\nu$, the LO cross section of WW$jj \to \ell\nu\ell\nu jj$ is scaled up by 35% and an uncertainty of 35% is assigned [71].

Process	Generator	PDF	N_{events}	$\sigma \times BR$ (pb)
WW$jj \to \ell\nu\ell\nu jj$	Alpgen	CTEQ4L	19,500	0.29 ± 0.10
WZ$jj \to \ell\ell jj$	Alpgen	CTEQ4L	25,000	0.092 ± 0.032
WW$\to \ell\nu\ell\nu$	Alpgen	CTEQ4L	152,400	1.38 ± 0.03

TABLE 4.6. Diboson Monte Carlo samples. The cross section and the branching ratio ($\sigma \times BR$) are used to normalize the Monte Carlo yield (Section 6.1) [49].

$Z/\gamma^* + jets$ *Processes* Like the signal Monte Carlo, the $Z/\gamma^* + jets$ events used in the measurement are generated with the Alpgen Monte Carlo generator with CAPS settings and a renormalization scale given by $m_Z^2 + \sum P_T^2$. The parton showering, B-meson decay, and τ decay are also constructed in the same manner as signal Monte Carlo. Samples are generated in three mass bins, and given relative weights according to the the ratios of the next-to-next-to-leading-order cross sections. The overall normalization is constrained to data (Section 6.2.2).

For the $Z/\gamma^* jj \to \tau\tau jj$ samples, only events in which both τ's decay to an electron or muon are considered. The branching ratio for this process is calculated as $(BR_{\tau \to \mu + X} + BR_{\tau \to e + X})^2$, where the square reflects the fact that the two τ's decay independently. This gives a final branching ratio of 0.1238 ± 0.0025 [33].

Though not used in the actual measurement, inclusive jet samples generated with Pythia are employed to perform data-to-Monte Carlo cross-checks at early levels of selection. The $Z/\gamma^* \to \tau\tau$ sample is normalized with measured cross sections, whereas the $Z/\gamma^* \to \mu\mu$ samples are normalized with the theoretical cross section [49]. The parton cuts on the $Z/\gamma^* \to \tau\tau$ sample include a requirement for the P_T of each electron or muon be greater than 8 GeV and a requirement that the dilepton invariant mass be greater than 30 GeV. Cuts are are also made on dilepton invariant mass for the other Pythia samples. Details on these samples as well as the Alpgen Z/γ^* samples described above are given in Table 4.7.

Process	$M_{\mu\mu}(GeV)$	Generator	PDF	N_{events}	$\sigma \times BR\ (pb)$
$Z/\gamma^*jj \to \mu\mu jj$	15-60	Alpgen	CTEQ5L	233,500	24.7
$Z/\gamma^*jj \to \mu\mu jj$	60-130	Alpgen	CTEQ5L	269,500	23.4
$Z/\gamma^*jj \to \mu\mu jj$	>130	Alpgen	CTEQ5L	66,500	0.2
$Z/\gamma^*jj \to \tau\tau jj$	15-60	Alpgen	CTEQ5L	12,033	3.060
$Z/\gamma^*jj \to \tau\tau jj$	60-130	Alpgen	CTEQ5L	68,127	2.899
$Z/\gamma^*jj \to \tau\tau jj$	>130	Alpgen	CTEQ5L	2,042	0.025
$Z/\gamma^*j \to \mu\mu j$	15-60	Alpgen	CTEQ5L	248,750	60.9
$Z/\gamma^*j \to \mu\mu j$	60-130	Alpgen	CTEQ5L	328,745	68.8
$Z/\gamma^*j \to \mu\mu j$	>130	Alpgen	CTEQ5L	24,000	0.62
$Z/\gamma^* \to \mu\mu$	15-60	Pythia	CTEQ5L	101,500	478.8 ± 25
$Z/\gamma^* \to \mu\mu$	60-130	Pythia	CTEQ5L	162,000	253.0 ± 13
$Z/\gamma^* \to \tau\tau$	>30	Pythia	CTEQ5L	155,404	12.61 ± 1

TABLE 4.7. Z/γ^* Monte Carlo samples. The N_{events} for the Alpgen $Z/\gamma^* \to \tau\tau$ samples corresponds to the number of events for which the τ particles decay leptonically. The cross section and the branching ratio ($\sigma \times BR$) for the Alpgen samples is only used to calculate relative weights. The overall normalization is constrained to data (Section 6.2.2) [49].

4.4.3 Detector Simulation

The last step in event simulation is to pass the generated samples through a comprehensive model of the detector in order to mimic the effect of the detector response, acceptance, and loss through non-instrumented material. At DØ this is performed with two packages: DØgstar and DØSim. DØgstar, which stands for 'DØ GEANT Simulation of the Total Apparatus Response' is a GEANT-based simulator that provides a complete simulation of the DØ detector [72, 73]. As Monte Carlo samples are passed through, DØgstar determines how much energy is deposited in which parts of the detector. The output of DØgstar is fed into DØSim which adds in the effects of proton pileup and minimum bias events as well as accounting for various electronic noise and inefficiencies not modeled in DØgstar, including SMT noise, as well as that originating in the calorimeter and muon system [74].

$$\text{CHAPTER 5}$$

$$\text{SELECTION CRITERIA AND EFFICIENCIES}$$

Of the more than 50 million events in the dimuon data skim, only a small fraction are $t\bar{t} \to \mu\mu$ events. To identify these events and discriminate them from background a series of selection cuts is applied. Those cuts that require the presence of physics objects consistent with signal events are collectively termed preselection. Additional cuts, called background rejection, are optimized to specifically target non-signal events with signatures similar to those of top decays.

Recall, from Equation 1.2, that an accurate estimate of the efficiency for $t\bar{t} \to \mu\mu$ events to pass all selection criteria, ϵ_{sig}, is necessary for the cross section calculation. This cumulative signal efficiency is calculated as the product of the individual selection cut efficiencies and eight data-to-Monte Carlo correction scale factors. The selection cut efficiencies are measured in a $t\bar{t}$ Monte Carlo sample. The correction scale factors account for the different responses of data and Monte Carlo events to the selection criteria.

This chapter begins by summarizing the preselection cuts and corresponding scale factors. The second section details the optimization procedure used to define the background rejection cuts. The final section summarizes the methods used to calculate individual cut efficiencies and presents the final signal efficiency table.

5.1 Preselection

The signature of a $t\bar{t} \to \mu\mu$ event consists of two oppositely charged, high P_T muons originating from the primary vertex, two high P_T jets, and substantial missing transverse energy. Preselection cuts select events with muons and jets consistent with this signature. The cuts can be divided into the following categories: muon identification,

which requires two well reconstructed muons as specified in Section 4.3.3; the trigger requirement described in Section 4.2; jet identification, which requires two well reconstructed jets as defined in Section 4.3.4; primary vertex identification detailed in Section 4.3.2; muon promptness, which requires the consistency of the muons with originating from the primary event vertex (Section 4.3.3); and muon isolation, which requires the muons to be isolated from other activity in the detector (Section 4.3.3).

A final category, channel orthogonality, places a veto on any event that contains a well reconstructed electron, as specified in Section 4.3.5. This cut facilitates the combination of the cross section measurement with measurements in other dilepton channels. Though the electron veto is not strictly preselection as defined above, it is included here for convenience. Table 5.1 summarizes the preselection cuts.

Category	Cut	Scale Factors
Muon Identification	≥ 2 Muons	✓
	Track Match	✓
	Muon Track χ^2	✓
	Opposite Charge	
	Muon $P_T > 15$ GeV	
Channel Orthogonality	Electron Veto	
Trigger Requirement	Table 4.3 and Table 4.4	
Jet Identification	≥ 2 Jets with $P_T > 20$ GeV	
Primary Vertex Identification	$|z| < 60$ cm, $N_{trk} \geq 3$	✓
	$|z^{d0root} - z^{reco}| < 5$ cm	✓
Muon Promptness	$|z^{\mu} - z^{PV}| < 1$ cm	✓
	Muon DCA Significance	✓
Muon Isolation	$Rat11 < 0.12$ & $Rattrk < 0.12$	✓

TABLE 5.1. $t\bar{t} \rightarrow \mu\mu$ preselection criteria. Selections cuts with a corresponding data-to-Monte Carlo scale factor are signified with a checkmark. The order of the table reflects the order in which the cumulative signal efficiency is calculated, see Table 5.8.

5.1.1 Scale Factors

An Alpgen $t\bar{t}$ Monte Carlo sample (Section 4.4.1) is employed to estimate the fraction of signal events that pass the selection criteria. Eight data-to-Monte Carlo scale factors are used to correct individual cut efficiencies measured in Monte Carlo to reflect those associated with data.

The general procedure for calculating correction scale factors is to measure the relevant selection cut efficiency in both data and Monte Carlo samples and compute the ratio. Samples of $Z \rightarrow \mu\mu$ events are utilized for all but one scale factor calculation because they contain unbiased events with signatures similar to $t\bar{t}$: two high P_T muons and jets. Unless otherwise noted, the $Z \rightarrow \mu\mu$ Monte Carlo corresponds to the Pythia Monte Carlo sample detailed in Table 4.7.

Muon Reconstruction and Identification The first step to calculate the muon reconstruction and identification scale factor, $\kappa_{\mu ID}$, is to obtain an unbiased sample $Z \rightarrow \mu\mu$ events in data. The 'MURECOEFF' data skim is employed. Unlike the 2MU data skim used for the measurement, MURECOEFF requires only one fully reconstructed muon. This muon is labeled the tag muon and a second muon, required only to be reconstructed as a central track, is labeled the probe. In order to remove bias, the muon trigger used to select the event for the skim must be matched to the tag muon. Additionally, the invariant mass of the tag and probe muons is required to be compatible with a $Z \rightarrow \mu\mu$ event. The muon reconstruction and identification efficiency is then calculated as the fraction of events for which the probe muon is matched to a fully reconstructed muon. The same measurement is performed in $Z \rightarrow \mu\mu$ Monte Carlo and the ratio of data-to-Monte Carlo efficiencies is plotted, binned in track η, track ϕ, and track P_T, see Figure 5.1.

The scale factor is calculated from a flat fit to the data-to-Monte Carlo ratio of efficiency versus muon detector η, as shown in Figure 5.2. The result is $\kappa_{\mu ID} = 1.000 \pm 0.014$ per muon where the systematic error is taken to be statistical in origin
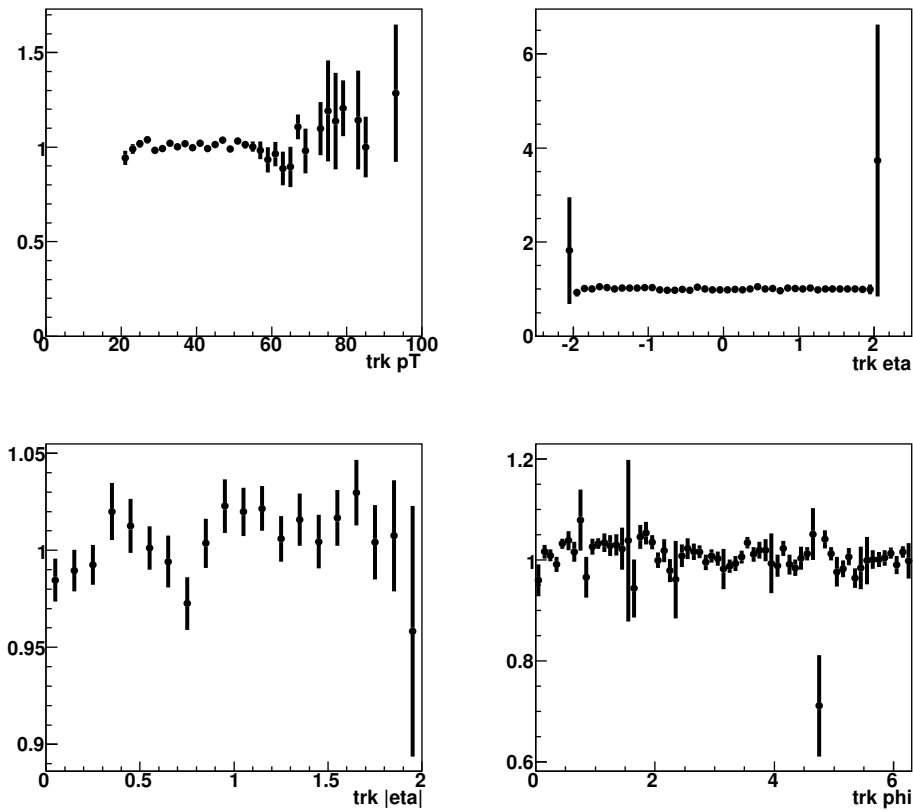
FIGURE 5.1. The ratio of data and Monte Carlo muon reconstruction and identification efficiencies as function of the track P_T, track η and track ϕ. No significant dependence on these quantities is observed.

(Section 7.2).
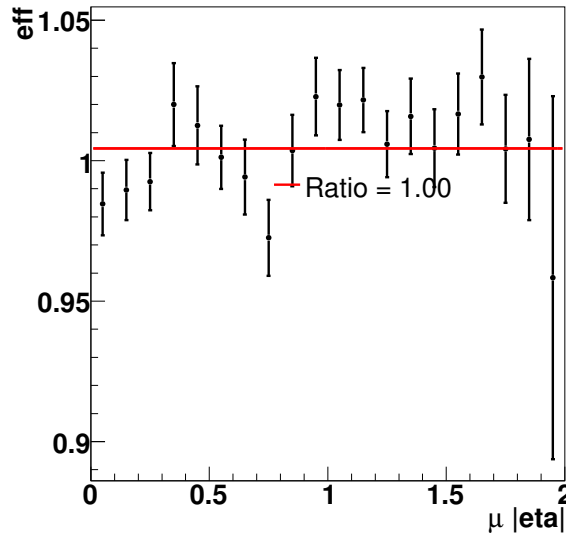
FIGURE 5.2. A flat fit to the muon reconstruction and identification scale factor as a function of muon detector η. The systematic error associated with the scale factor is calculated with a conservative approach, discussed in Section 7.2.

Muon Track Match The muon track match efficiency is calculated in a sample of select tight, isolated muons taken from the dimuon data skim. (The full selection criteria are described in [75].) For each muon in the sample, a 'matching' window is drawn as $0.6\eta \times 0.4\phi$ around the center of the muon position defined by its trace in the calorimeter. The raw track match efficiency, ϵ_{raw}, is measured as the fraction of muons with one or more tracks present in its matching window. However, this efficiency must be corrected for contamination from random tracks not associated with the muon. The random track efficiency, ϵ_{random}, is measured in a control window drawn adjacent in ϕ to the matching window. The true efficiency is then calculated as:

$$\epsilon_t = \frac{\epsilon_{raw} - \epsilon_{random}}{1 - \epsilon_{random}}. \tag{5.1}$$

A similar procedure is applied to $Z \to \mu\mu$ Monte Carlo samples. The efficiencies in data and Monte Carlo are parameterized in η and ϕ, and the correction scale factor, $\kappa_{trk-match}$, is extracted from the ratio of corrected and uncorrected efficiencies in $t\bar{t}$ Monte Carlo. The statistical error from each $\eta - \phi$ bin in the parameterization is used to quote an overall uncertainty [75]. Because it is parameterized, $\kappa_{trk-match}$ is applied as a per event weight rather than as a simple scale factor. For $t\bar{t}$, $\kappa_{trk-match} = 0.968 \pm 0.024$ taking into account both muons [49].

Track χ^2 The track χ^2 requirement is a cut on the quality of the muon track match. Like $\kappa_{trk-match}$, the data-to-Monte-Carlo scale factor associated with the track χ^2 requirement is measured in the dimuon data skim as well as in Monte Carlo samples of $Z \to \mu\mu$ events. Z selection is accomplished by requiring the dimuon invariant mass to be in the range of 70 to 110 GeV. The cut efficiency is calculated by measuring the event yields of two groups of events: one in which a basic set of cuts including full muon identification requirements, vertex quality, muon promptness, muon isolation, trigger, and electron veto is applied, and a second in which the same set of cuts is applied except for the track χ^2 cut. The ratio of the first group to the second gives the efficiency for the track χ^2 cut. This efficiency measurement is computed for each of three inclusive jet multiplicities in both data and Monte Carlo in order to test the dependence of the scale factor on the number of jets. The results are shown in Table 5.2. Since no obvious dependence is observed, $\kappa_{trk-\chi^2}$ is taken from the inclusive zero jet bin. The final scale factor is $\kappa_{trk-\chi^2} = 0.970 \pm 0.001$, where the error is assumed to be statistical in origin. The per muon scale factor can be calculated as the square root of the per event scale factor, and the associated error is the per event error divided by two. This gives 0.985 ± 0.001.

Primary Vertex Two cuts are associated with the reconstruction of the primary vertex: one cut restricts the maximum distance of the primary vertex from the origin

	$\epsilon_{data}(Z \to \mu\mu)$	$\epsilon_{MC}(Z \to \mu\mu)$	scale factor	$\epsilon_{t\bar{t} \times \kappa}^{\chi^2 < 4}$
$N_{jet} \geq 0$	0.967±0.001	0.998±0.000	0.970±.001	0.966±0.002
$N_{jet} \geq 1$	0.962±0.004	0.999±0.001	0.963±.004	0.959±0.005
$N_{jet} \geq 2$	0.958±0.012	0.997±0.003	0.960±.012	0.957±0.012

TABLE 5.2. Measured efficiencies of the track χ^2 cut in $Z \to \mu\mu$ data and Monte Carlo events for inclusive jet multiplicity bins and per dimuon event. The corresponding (per event) scale factors are shown in the third column. The last column shows the $t\bar{t}$ signal efficiency with the scale factor correction applied. The signal efficiency measurements are made with Alpgen $t\bar{t}$ Monte Carlo [49].

and requires it to have been reconstructed from a minimum of three tracks, and another requires consistency between two vertex reconstruction packages. A cut is also made on the muons in the event to ensure that each muon candidate is consistent with originating from the primary vertex (Section 4.3.3). This latter cut ensures that the muons are 'prompt' and is most appropriately discussed with the cut on DCA significance (Section 4.3.3). However, its scale factor is discussed here because it is calculated in the same way as the scale factors of the two primary vertex cuts. As with the track χ^2 cuts, the efficiencies of these three requirements are measured in $Z \to \mu\mu$ data and Monte Carlo samples by taking the ratio of the event yields of two groups: the first passing a set of preselection cuts including the relevant primary vertex cut and the second passing the same set of preselection cuts excluding the relevant primary vertex cut. The results are shown in Table 5.3.

This procedure was repeated with $Z \to ee$ events as part of the $t\bar{t} \to ee$ cross section measurement. Since there should not be significant variation between the $Z \to ee$ and $Z \to \mu\mu$-derived scale factors, the full statistics of both samples are leveraged and a combination of the scale factors is utilized. When both scale factors are consistent within error, the average result is used. When the results are inconsistent, these differences are assumed as systematic errors. The final scale factors are given in Table 5.4.

N_{jets}	$\epsilon_{data}(Z \to \mu\mu)$	$\epsilon_{MC}(Z \to \mu\mu)$	scale factor	$\epsilon^{PV}_{t\bar{t}\times\kappa}$
$z_{PV}\& N_{trk} \geq 3$				
≥ 0 jets	0.967± 0.001	0.986± 0.001	0.980± 0.001	0.970± 0.002
≥ 1 jet	0.979± 0.003	0.990± 0.002	0.989± 0.003	0.979± 0.004
≥ 2 jets	0.991± 0.004	0.996± 0.003	0.995± 0.005	0.986± 0.006
$\Delta z(D\emptyset root, D\emptyset reco)$				
≥ 0 jets	0.994± 0.001	0.999± 0.000	0.995± 0.001	0.994± 0.001
≥ 1 jet	0.995± 0.001	0.999± 0.001	0.996± 0.002	0.995± 0.002
≥ 2 jets	0.998± 0.002	0.998± 0.002	1.000± 0.003	0.999± 0.003
$\Delta z(PV, \mu)$				
≥ 0 jets	0.980± 0.001	0.994± 0.000	0.986± 0.001	0.982± 0.002
≥ 1 jet	0.979± 0.003	0.995± 0.001	0.984± 0.003	0.980± 0.003
≥ 2 jets	0.962± 0.009	0.996± 0.003	0.966± 0.010	0.963± 0.010

TABLE 5.3. Measured efficiencies of the primary vertex cuts in $Z \to \mu\mu$ data and Monte Carlo events for inclusive jet multiplicity bins and per dimuon event. The corresponding (per event) scale factors are shown in the third column. The last column shows the $t\bar{t}$ signal efficiency with the scale factor correction applied. The efficiency measurements are made with Alpgen $t\bar{t}$ Monte Carlo [49].

$\kappa^{PV}(\mathrm{N_{jet}} \geq 0)$	$0.981 \pm 0.001(stat)$
$\kappa^{PV}(\mathrm{N_{jet}} \geq 1, \mathrm{N_{jet}} \geq 2)$	$0.993 \pm 0.002(stat) \pm 0.004(syst)$
$\kappa^{D\varnothing root, D\varnothing reco}$	$0.998 \pm 0.001(stat) \pm 0.002(syst)$
$\kappa^{PV,\ell}$	$0.987 \pm 0.001(stat)$

TABLE 5.4. The (per event) scale factors. The ≥ 1 jet bin is used as the final scale factor for the first primary vertex cut. For the other scale factors, the ≥ 0 jet bin is used [49].

DCA Significance Like the primary vertex cuts, the efficiency of the DCA significance requirement is calculated as the ratio of two event yields in $Z \to \mu\mu$ events. The first event yield corresponds to events which pass muon identification, muon P_T, opposite charge, isolation, vertex quality, track matching, trigger, and DCA significance requirements, while the second event yield corresponds to events which pass all such cuts except for the DCA significance cut. The data and Monte Carlo efficiencies and the corresponding scale factors are given in Table 5.5 for three jet multiplicities. Because the scale factor calculated with the inclusive zero jet sample differs from the higher jet multiplicity cases, the scale factor on DCA significance is taken from the one jet inclusive sample. $\kappa_{DCA} = 0.991 \pm 0.005$, and the associated per muon correction factor is 0.994 ± 0.003 [49].

	$\epsilon_{data}(Z \to \mu\mu)$	$\epsilon_{MC}(Z \to \mu\mu)$	scale factor	$\epsilon_{t\bar{t}\times\kappa}^{DCA}$
$\geq$0 jet	0.924 ± 0.002	0.911 ± 0.002	1.014 ± 0.003	0.888 ± 0.007
$\geq$1 jet	0.967 ± 0.004	0.976 ± 0.003	0.991 ± 0.005	0.867 ± 0.008
$\geq$2 jets	0.965 ± 0.011	0.983 ± 0.007	0.981 ± 0.013	0.849 ± 0.014

TABLE 5.5. Measured efficiencies of the DCA significance cut in $Z \to \mu\mu$ data and Monte Carlo samples for inclusive jet multiplicity bins and per dimuon event. The corresponding (per event) scale factors are shown in the third column. The last column shows the $t\bar{t}$ signal efficiency with the scale factor correction applied. The signal efficiency measurements are made with Alpgen $t\bar{t}$ Monte Carlo [49].

Muon Isolation The muon isolation scale factor, κ_{iso}, is calculated in data and Monte Carlo samples of $Z \to \mu\mu$ events with all preselection cuts applied excluding the

isolation requirement. As for the muon identification scale factor, a tag and probe method is employed. In this instance, the tag muon corresponds to a muon that passes the isolation criteria and the rate at which the second muon, the probe, passes is taken to be the isolation efficiency. However, by requiring only one muon to be isolated, the test sample in data is susceptible to contamination by $W + jets$ events. This contamination is evident in Figure 5.3 when the leading P_T muon is used as the tag muon. The same figure shows that $W + jets$ contamination is less evident when the second-leading P_T muon is used as the tag, so this choice is made for the scale factor calculation.

The ratio of the isolation efficiencies in data and Monte Carlo is plotted in Figure 5.4 as a function of the distance to the closest jet, $\Delta R(\mu, jet)$, in order to test for dependence on this quantity. Despite lower statistics for muons close to a jet, a flat fit to the distribution is reasonable. The scale factor, κ_{iso}, is extracted from the fit, and the systematic error on the scale factor is taken from the fit's statistical uncertainty. The scale factor can also be calculated directly from the ratio of data and Monte Carlo efficiencies. In order to account for the potential mismeasurement of efficiencies in events with muons close to jets, muons are required to have $\Delta R(\mu, jet) > 0.5$. Both the flat fit and the direct calculation yield consistent results, and the final per muon scale factor is taken to be 1.00 ± 0.004 giving a per event scale factor $\kappa_{iso} = 1.00 \pm 0.008$ for two muons.

5.2 Background Rejection

The dominant background in the dimuon channel is $Z/\gamma^* + jets \to \mu\mu + jets$ where apparent $\not{E}_T$ arises from instrumental effects such as calorimeter noise or misreconstructed muons. After the preselection cuts are applied, this background is ≈ 170 times larger than the next most significant background and still ≈ 60 times more prevalent than signal. To specifically target the Z background, two additional selec-
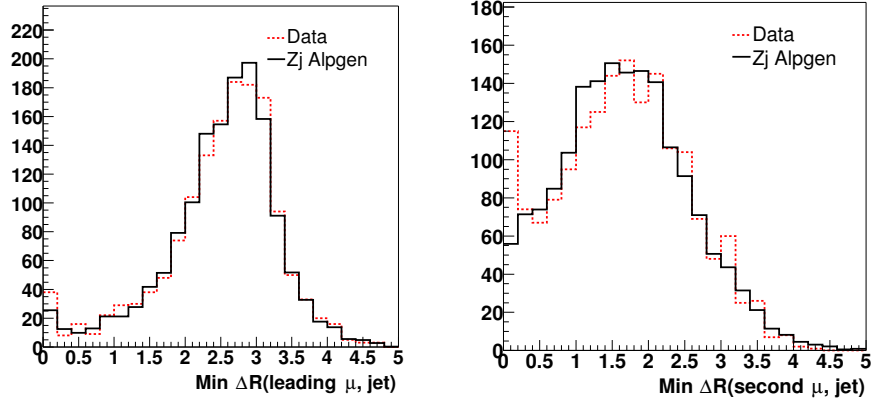
FIGURE 5.3. Distributions in $Z+j$ data and and Alpgen Monte Carlo samples of the distance between the leading muon (second leading) and the closest jet are shown in the left (right). In the left plot, the second leading muon is required to be isolated. In the right plot, the leading muon is required to be isolated. The first bin on the right plot shows evidence of non-Z background in data [51].
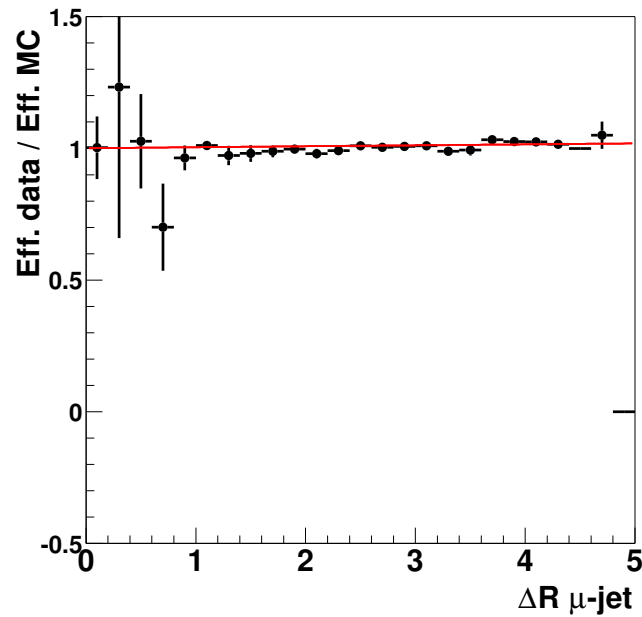
FIGURE 5.4. A flat fit to the muon isolation scale factor as a function of distance between the muon and the closest jet [51].

tion cuts are imposed: a χ^2_Z cut that tests the consistency of the event kinematics with a $Z/\gamma^* \to \mu\mu$ event and a contour cut that places a varying minimum requirement on $\not{E}_T$, based on an event's position in the plane formed by $\not{E}_T$ and the opening angle in ϕ between the highest P_T muon and the $\not{E}_T$ ($\Delta\phi(\mu_{leading}, \not{E}_T)$). These two cuts are optimized taking into account not only the expected Z background, but also the $WW + jets \to \mu\mu + \nu\nu + jets$ background described in Chapter 6.

5.2.1 The χ^2_Z Cut

The χ^2_Z variable, constructed from muon P_T, is effectively a one-dimensional fit to the dimuon invariant mass. Cutting on χ^2_Z is preferable to a simple mass cut that removes the Z peak because the χ^2_Z fit accounts for differences in the momentum resolution for different values of track P_T and η. The variable χ^2_Z is defined as:

$$\chi^2_Z(\kappa_1, \kappa_2) = \sum_{i=1}^{2} \left(\frac{\kappa_i - \kappa_i^0}{\sigma_i(P_T^i, \eta_i)} \right)^2 + (M_{\mu\mu} - M_Z) \tag{5.2}$$

where κ_i^0 are the measured values of the muons' inverse momenta, $\sigma_i(P_T^i, \eta_i)$ are the resolutions associated with the inverse momenta, $M_{\mu\mu}$ is the measured dimuon invariant mass, and M_Z is a mass constraint taken to be the Z mass [76, 51]. κ_i are refitted values of the muon's inverse momenta ($\kappa_i = \frac{1}{P_\mu^i}$), calculated by minimizing Equation 5.2. Both data and Monte Carlo samples of $Z \to \mu\mu$ events are used to derive the resolutions, $\sigma_i(P_T^i, \eta_i)$ [45].

Equation 5.2 can also be written as:

$$\chi^2_Z(\kappa_1) = \left(\frac{\kappa_1 - \kappa_1^0}{\sigma_1} \right)^2 + \left(\frac{\kappa_2 - \kappa_2^0}{\sigma_2} \right)^2 \tag{5.3}$$

where the momenta are related by the mass constraint:

$$\kappa_2 = \frac{2(1 - \cos\gamma)}{\kappa_1 M_Z^2} \tag{5.4}$$

and γ is the angle between the two muons.
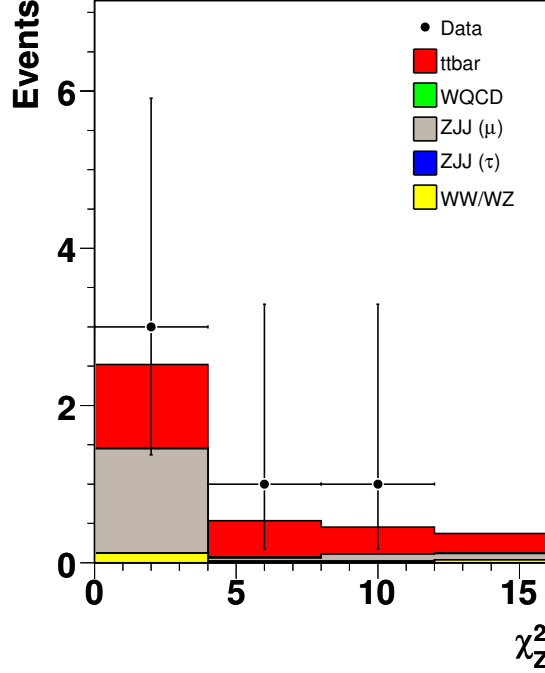
FIGURE 5.5. χ_Z^2 distribution in data and Monte Carlo with all selection criteria applied except the χ_Z^2 cut.

A distribution of χ_Z^2 is shown in Figure 5.5 for preselected events. The lower the value of χ_Z^2 of the event, the higher the chance of it being a $Z/\gamma^* \rightarrow \mu\mu$ event. In order to pass selection, the final event $\chi_Z^2 \geq 4$.

5.2.2 Contour Cut

Since $Z/\gamma^* \rightarrow \mu\mu$ events have no intrinsic $\not{E}_T$, missing transverse energy is an effective variable to discriminate between this background and signal. The $\not{E}_T$ cut applied in this analysis is a contour cut in the $\not{E}_T$ and $\Delta\phi(\mu_{leading}, \not{E}_T)$ plane, which was found to be more effective than a simple $\not{E}_T$ cut [51]. The motivation for the cut is illustrated in Figure 5.6, which shows the distribution of background and signal events in the $\not{E}_T$ and $\Delta\phi(\mu_{leading}, \not{E}_T)$ plane. The contour, drawn in black, is defined by three points:

'MET' is the minimum cut on $\not{E}_T$ pictured as the straight line segment, 'X_{High}' defines the upper limit of the triangular cut and 'X_{Low}' is the lower limit of the triangular cut. The corresponding limits in Y, 'Y_{High}' and 'Y_{Low}', are defined in terms of limits in X as:

$$Y_{High} = 175 - (X_{High} - MET) \tag{5.5}$$

$$Y_{Low} = X_{Low} - MET. \tag{5.6}$$

In order to pass selection, events must be to the right of the contour defined by: MET $= 45$, $X_{High} = 95$, and $X_{Low} = 90$. All events with $\Delta\phi(\mu_{leading}, \not{E}_T) > 175°$ are also removed because events for which $\not{E}_T$ and $\mu_{leading}$ are in opposite directions are more likely to have mismeasured muon momenta. Figure 5.7 shows the $\not{E}_T$ distributions in data and Monte Carlo before and after the contour cut is applied. The effect of the contour cut on background events can be clearly seen.
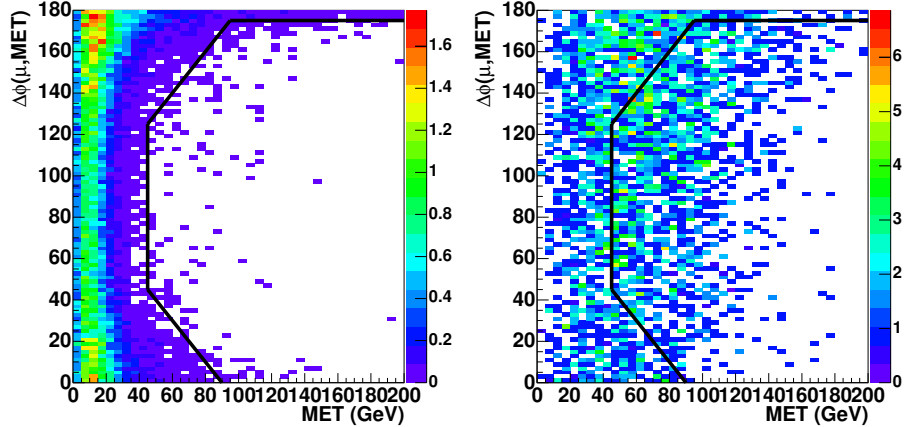
FIGURE 5.6. $\Delta\phi(\mu_{leading}, \not{E}_T)$ vs. $\not{E}_T$ distributions for a combination of $(Z/\gamma^* \to \mu\mu)jj$ and $(WW \to \mu\mu)jj$ background Monte Carlo (left plot) and $t\bar{t}$ signal (right plot). The contour cut is drawn in black.
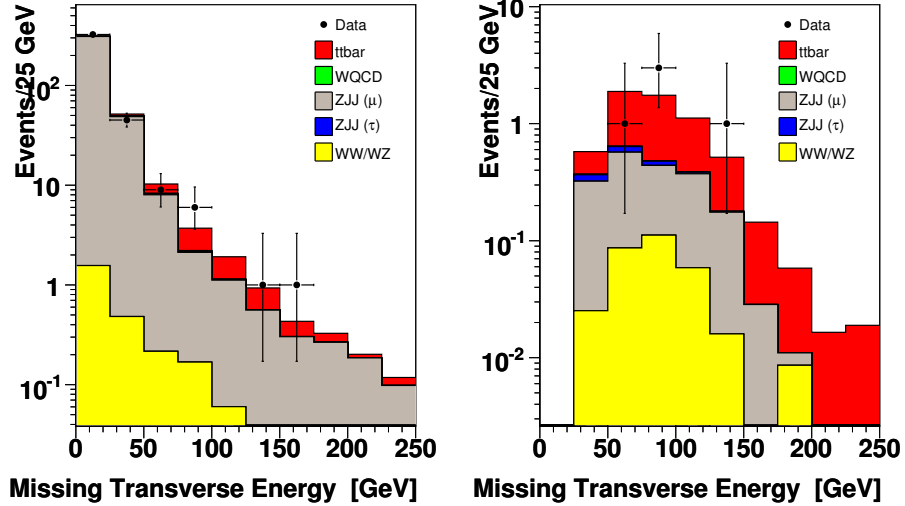
FIGURE 5.7. $\not{E}_T$ distributions in data and Monte Carlo before (left) and after (right) the contour cut.

5.2.3 Optimization

The values of the χ^2_Z cut and the contour cut are selected with a grid point optimization procedure using signal and background Monte Carlo. For the optimization, each variable is simultaneously varied between seven evenly incremented values, specifically: χ^2_Z from 0 to 6, MET from 15 to 45, X_{High} from 75 to 105, and X_{Low} from 75 to 105. This results in 2401 possible cut values. Figure 5.8 displays these points organized in a grid of expected signal and background yields for each cut value. Alpgen $t\bar{t}$, $(Z/\gamma^* \to \mu\mu)jj$, and $(WW \to \mu\mu)jj$ Monte Carlo samples are used to estimate these yields. For each point, a figure of merit is calculated. This figure of merit is a modification of the standard $\frac{\sqrt{S+B}}{S}$, where S is the expected signal yield and B is the expected background yield. The exact figure of merit used is:

$$FOM = \frac{\sqrt{S + 2B + (\frac{1}{4}B)^2}}{S} \qquad (5.7)$$

where the '$\frac{1}{4}B$' accounts for a 25% systematic uncertainty on the Z/γ^* background yield and the '$2B$' provides an extra penalty for high background yields. Extra

background suppression is desirable because the Z/γ^* background is not well-modeled. The combination of cuts associated with the lowest figure of merit is selected.

In order to reduce bias and increase statistics, isolation requirements are relaxed on the simulated $(Z/\gamma^* \to \mu\mu)jj$ sample. Events are otherwise required to pass the preselection requirements listed in Table 5.1. Table 5.6 shows the cut values before and after optimization together with the figure of merit and signal-to-background ratio. The before values correspond to the cut values chosen for a prior pass of the analysis, optimized for a smaller data set and a different muon identification requirements [51]. The signal-to-background ratio is substantially improved by the optimization.
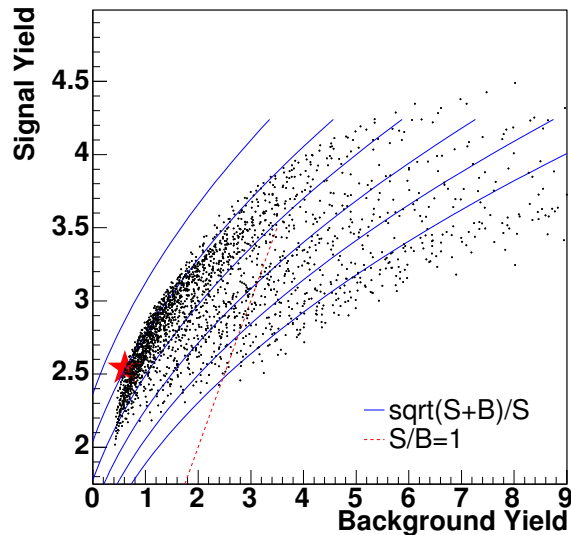
FIGURE 5.8. Grid search showing expected signal and background yields for the 2401 set of cuts considered. The red star marks the optimal set of cuts chosen by the figure of merit.

5.3   Efficiency Measurements

The per event signal efficiency for each selection cut is calculated in Alpgen $t\bar{t} \to \mu\mu$ Monte Carlo where the muons are required to originate from either W or τ decays.

Cut	Before Optimization	After Optimization	No χ^2_Z Cut
χ^2	2	4	0
$\not{E}_T$	35	45	45
X_High	85	95	95
X_Low	85	90	90
FOM	0.95	0.77	0.84
S/B	1.62	4.16	1.49

TABLE 5.6. A comparison of background rejection cuts before and after optimization for this data set. The optimized cuts are significantly tighter, resulting in a significant improvement of the signal-to-background ratio (S/B). The final column shows the figure of merit (FOM) and signal-to-background ratio for the optimized contour cut in the absence of the χ^2_Z cut. This demonstrates that the χ^2_Z cut plays an important role in background rejection not accounted for by the contour cut alone.

Individual cut efficiencies are calculated as:

$$\epsilon = \frac{N_{cut}}{N} \tag{5.8}$$

where N_{cut} is the number of events which pass all selection cuts up to and including the relevant cut (in the order displayed in Table 5.8) and N is the number of events which pass the selection cuts up to but not including the one for which the efficiency is being measured. This procedure is similar to that described in the calculation of scale factors such as $\kappa_{trk-\chi^2}$, κ_{DCA}, and the three primary vertex scale factors.

Because cut efficiencies are measured in Monte Carlo, and the trigger requirement as stated in Section 3.9 is defined only for data events, the trigger efficiency measurement is necessarily more complex. For this reason, it is described in more detail in Section 5.3.1. The cumulative signal efficiency is calculated by multiplying the individual cut efficiencies and the data-to-Monte Carlo scale factors described in Section 5.1.1. The final results are presented in Section 5.3.2.

5.3.1 Trigger Efficiency

Recall from Section 4.2 that the online trigger requirement consists of a combination of single muon triggers and dimuon triggers, each of which has Level 1, Level 2, and Level 3 criteria. The first step to measure the overall efficiency of the online trigger requirement is to measure the efficiencies of each trigger at all three levels. However, previous studies have shown the Level 3 requirements to be greater than 99.5% efficient for dimuon events. Therefore, these efficiencies are assumed to be 100% efficient for this analysis and are not remeasured [77].

Table 4.3 and Table 4.4 list the names and specifications of the single muon triggers and dimuon triggers, respectively. The two single muon triggers, MUW_W_L2M3-_TRK10 and MUH2_LM15, have different Level 1 and Level 2 terms, while all the dimuon triggers have the same Level 1 and Level 2 terms. This gives a total of three Level 1 trigger efficiencies that must be measured, and three Level 2 trigger efficiencies. The three Level 1 and Level 2 terms are summarized in Table 5.7.

A clean, unbiased sample of data events is needed for these measurements. As with the calculation of the muon identification scale factor, $Z \to \mu\mu$ events are chosen because they are signal-like, high P_T dimuon events. Several quality cuts are made to increase the purity of the sample by eliminating out-of-time cosmic ray muons, muons likely to have poor reconstruction quality, and muons outside of a tight Z mass window. They include:

- rejection of muons in the bottom hole (Section 4.3.3)

- tight timing cuts on tag muon & cuts to ensure consistency with the primary vertex

- acolinearity > 0.1 to reject cosmics

- $|\Delta z(\mu, \mu)| < 1$ cm

- 80 GeV $< M_{\mu\mu} <$ 100 GeV

- $P_T > 20$ GeV for tag muon, 15 GeV for probe muon

To measure the Level 1 efficiencies, a subsample of events is selected in which a muon is matched in both region and octant to the single muon trigger associated with the Level 1 requirements of the relevant trigger. This is the tag muon. Since the tag muon caused the event to be selected by the online trigger requirement, the second muon in the sample, the probe muon, is unbiased. The trigger efficiency is defined as the fraction of events for which the probe muon matches the Level 1 trigger requirements:

$$\epsilon_{Level1} = \frac{\text{\# probe muons with matching Level 1 trigger}}{\text{total number of probe muons}} \qquad (5.9)$$

Each muon in the event is a potential tag muon. Once a muon passes the requirements to be a tag muon, all other muons in the event become potential probe muons. Thus, multiple probe muons in each event may be included in the efficiency calculation.

For the Level 2 efficiency measurements, the same procedure is conducted on the sample of events for which the Level 1 trigger fired.

Measured Level 1 and Level 2 efficiencies are binned in η, P_T, and ϕ. These efficiencies are used to fit functions that mimic the individual Level 1 and Level 2 trigger requirements. Fit functions are binned in η since the P_T and ϕ distributions are approximately flat. The fits are restricted to the fiducial region, defined as $|\eta| < 2.0$ for the dimuon trigger and $|\eta| < 1.5$ for the two single muon triggers. Figures 5.9 and 5.10 show the Level 1 and Level 2 fit functions. Details on the fitting procedure can be found in [52].

The probability that a Monte Carlo event will pass an individual trigger requirement is computed by evaluating the Level 1 and Level 2 fit functions for that event. The overall efficiency is defined as:

$$\epsilon(\eta) = T_1(\eta)f_1 + T_2(\eta)f_2 + T_3(\eta)f_3 \qquad (5.10)$$
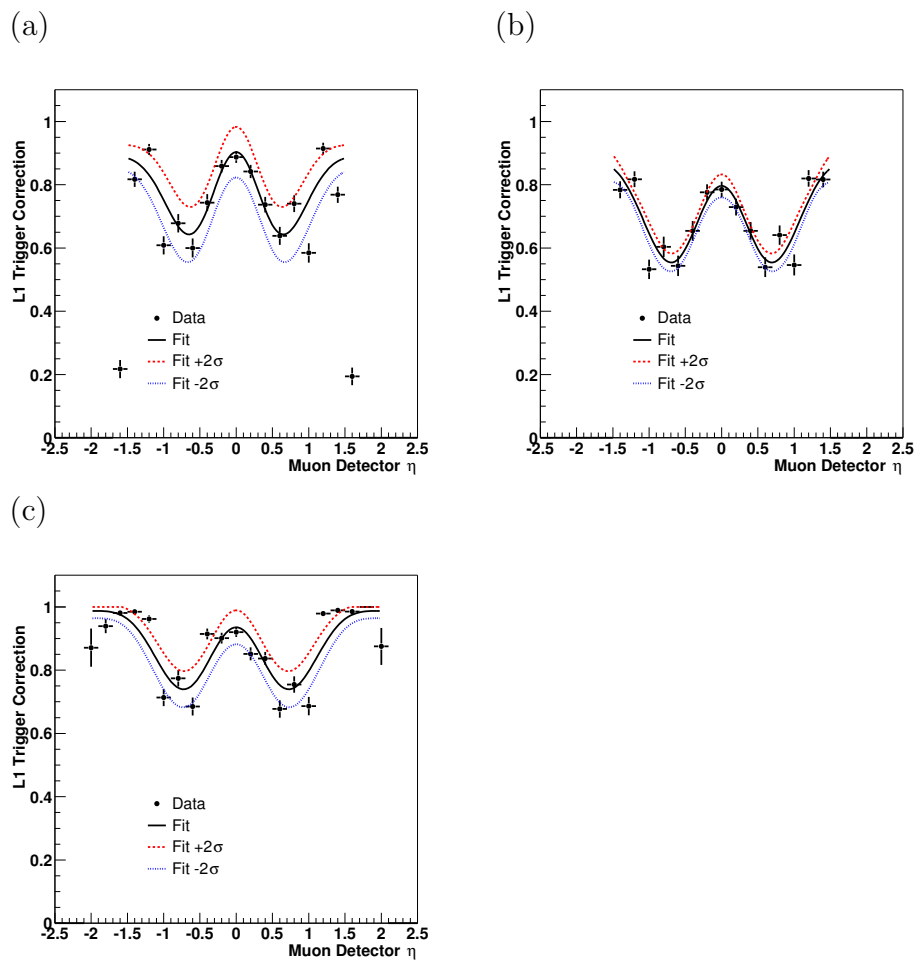
FIGURE 5.9. Per muon Level 1 trigger efficiencies with errors (a) MUW_W-_L2M3_TRK10 (b) MUH2_LM15 (c) Dimuon Trigger. Dotted curves represent a conservative error estimate discussed in Section 7.2. Note that for the dimuon trigger, the per muon efficiency corresponds to the Level 1 term mu1ptxatxx. The dimuon trigger efficiency assumes that each muon fires mu1ptxatxx.

(a)

(b)

(c)
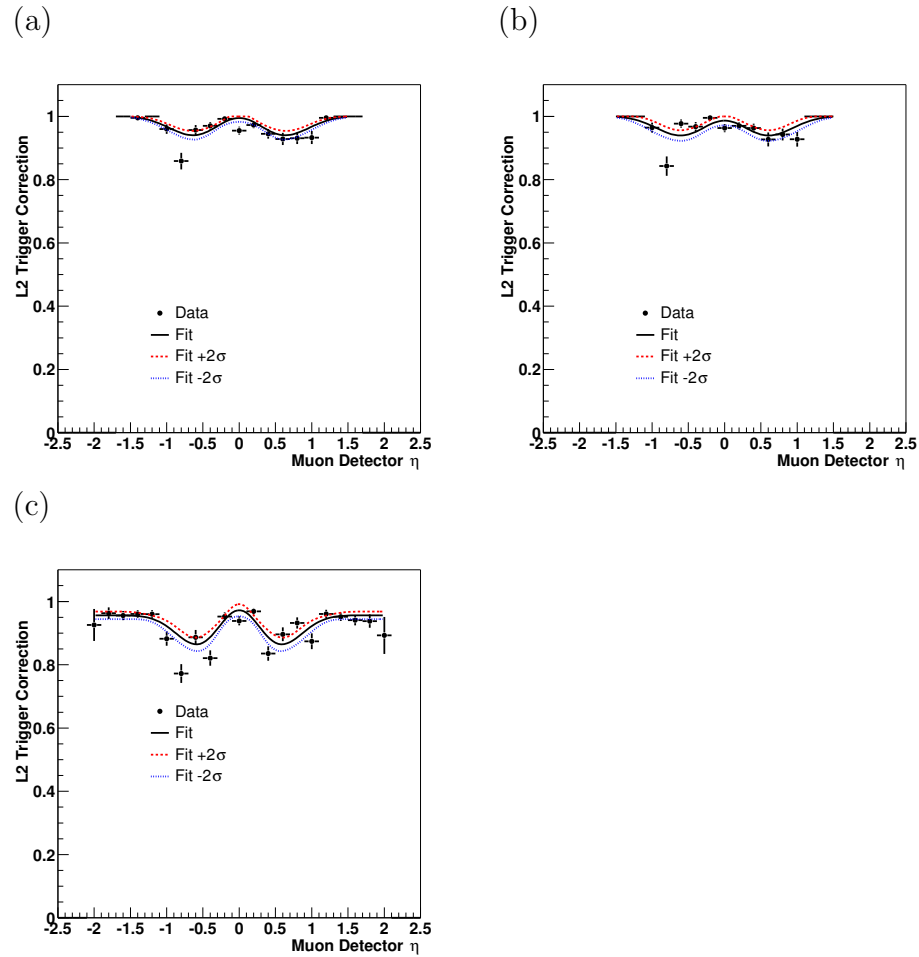
FIGURE 5.10.   Per muon Level 2 trigger efficiencies with errors (a) MUW_W-_L2M3_TRK10 (b) MUH2_LM15 (c) Dimuon Trigger.   Dotted curves represent a conservative error estimate discussed in Section 7.2.

Trigger Name	Level 1 Term	Level 2 Term	Luminosity Fraction
MUW_W_L2M3_TRK10	mu1ptxwtlx	1 medium μ P_T >3 GeV	0.74
MUH2_LM15	mu1ptxatlx + 1 track P_T > 10 GeV	1 medium μ P_T >3 GeV	0.11
Dimuon Trigger	mu2ptxatxx	1 medium μ	0.15

TABLE 5.7. Level 1 and Level 2 trigger terms. The Level 1 terms are explained in Section 4.2. The last column shows the fraction of the total integrated luminosity of the data set associated with each trigger (Section 4.2).

where $T_i = \epsilon_1^i \times \epsilon_2^i$, and ϵ_1^i and ϵ_2^i are the Level 1 and Level 2 efficiencies of trigger i, respectively. f_i is the fraction of the total integrated luminosity associated with trigger i (Table 5.7). The overall efficiency is treated as a weight that is assigned to each Monte Carlo event.

5.3.2   Efficiency Results

The efficiency of each selection cut is listed in Table 5.8. The cumulative efficiency, measured as the product of the individual cut efficiencies and correction scale factors, is 6.4%, meaning that only 6.4 out of every 100 signal events passes the selection requirements. Though this number is low, it is comparable to or higher than the efficiency calculated in prior passes of this analysis [51, 49]. In fact, the preselection efficiency is 31% higher than the most recent version of the analysis due to a relaxation of the muon identification criteria and corresponding trigger requirement update (Section 4.2). Unfortunately, this relative gain in efficiency is lost by the less efficient, tighter background rejection cuts, optimized to reduce the dominant $Z \to \mu\mu$ background.

Other culprits for the low signal efficiency include the muon isolation requirement at 76%, the jet identification requirement at 80%, and the muon P_T requirement at 69%. As a comparison, the cumulative efficiency in the dielectron decay channel is

$\approx 8\%$ and in the electron muon channel is 14% [79]. Although the efficiency for electron reconstruction is lower than that for muons, these channels do not suffer from such tight background rejection cuts.

Category	Cut	Efficiency	Cum. Efficiency
Muon Identification	Muon ID & Track Match	0.695 ± 0.004	0.695
	$\kappa_{\mu ID}$	1.000	0.695
	Muon Track-χ^2	0.996 ± 0.001	0.692
	$\kappa_{trk-match}$	0.968	0.670
	$\kappa_{trk-\chi^2}$	0.970	0.650
	Opposite Charge	0.868 ± 0.003	0.564
	Muon $p_T > 15$ GeV	0.687 ± 0.005	0.388
Channel Orthogonality	Electron Veto	0.998 ± 0.001	0.387
Trigger		0.911 ± 0.004	0.353
Jets	≥ 2 Jets	0.795 ± 0.005	0.280
	≥ 2 Jets with $p_T > 20$ GeV	0.940 ± 0.003	0.264
Primary Vertex	$|z| < 60$ cm, $N_{trk} \geq 3$	0.986 ± 0.002	0.260
	κ_{PV}	0.993	0.258
	$|z^{D\emptyset root} - z^{D\emptyset reco}| < 5$ cm	0.998 ± 0.001	0.258
	$\kappa_{root-reco}$	0.998	0.257
Muon Promptness	$|z^\mu - z^{PV}| < 1$ cm & $|z^\mu - z^{PV}| < 1$ cm	0.999 ± 0.001	0.257
	$\kappa_{PV,l}$	0.987	0.253
	Muon DCA Significance	0.852 ± 0.005	0.216
	κ_{DCA}	0.991	0.214
Muon Isolation	$Rat11 < 0.12$ & $Rattrk < 0.12$	0.757 ± 0.007	0.162
	κ_{Iso}	1.000	0.162
χ_Z^2	$\chi_Z^2 > 4$	0.722 ± 0.008	0.117
Contour Cut		0.546 ± 0.011	0.064 ± 0.002

TABLE 5.8. Efficiencies for $t\bar{t} \rightarrow \mu\mu$ selection cuts, measured in Monte Carlo events where the muon is allowed to come from W or τ decays, together with correction scale factors (κ). The correction factors and efficiencies shown are per event. Scale factor uncertainties, not shown here, are discussed in Section 7.2.

The expected signal yield after all selection criteria are applied can be calculated from the overall signal efficiency, ϵ_{sig}, the integrated luminosity of the data set, $\mathcal{L}_{Int}$, the total branching fraction of $t\bar{t} \rightarrow \mu\mu$ events (including $W \rightarrow \tau\nu$ decay), $BR(t\bar{t} \rightarrow \mu\mu) = 0.01571 \pm 0.00031$, and an assumed production cross section of $\sigma_{t\bar{t}} = 7$ pb as:

$$N_{t\bar{t}} = \sigma_{t\bar{t}} \times \mathcal{L}_{Int} \times \epsilon_{sig} \times BR(t\bar{t} \rightarrow \mu\mu) \qquad (5.11)$$

This gives:

$$N_{t\bar{t}} = 2.96 \pm 0.08(stat)^{+0.30}_{-0.34}(sys). \qquad (5.12)$$

The sources of systematic uncertainty on this yield are discussed in Section 7.2. The

expected signal yields at different selection cut levels, used for data and Monte Carlo cross-checks and selection cut studies, are given in Chapter 6.

Chapter 6

Background Estimation

Despite the background rejection cuts described in Section 5.2, some non-$t\bar{t}$ events may be present in the final data set. These background events can be categorized as either physics backgrounds or instrumental backgrounds. Physics backgrounds share the same event signature as signal events, with two reconstructed muons, two jets, and $\not{E}_T$ from neutrinos. Such backgrounds include the two diboson backgrounds, $WW+jets \rightarrow \mu\mu+\nu\nu+jets$ and $WZ+jets \rightarrow \mu\mu+\nu+jets$, as well as $Z/\gamma^*+jets \rightarrow \tau\tau + jets \rightarrow \mu\mu + \nu\nu\nu\nu + jets$ events. By contrast, the dominant background, $Z/\gamma^* + jets \rightarrow \mu\mu + jets$, is an instrumental background. Its event signature differs from the $t\bar{t}$ signature in that it has no real $\not{E}_T$ from neutrinos. However, event misreconstruction may give rise to enough fake $\not{E}_T$ to allow some of these events to pass selection criteria. Finally, QCD multijet production and W+jets events comprise another type of instrumental background. Although these events have at most one real isolated muon, they could appear in the final data sample if one or more muons from a jet fakes isolation.

This chapter describes each of the above backgrounds and the procedure used to estimate their yields. At the end of chapter, data and Monte Carlo comparison plots for relevant kinematic and topological distributions are displayed to test the consistency of the background estimation with data. The total expected signal and background yields are also presented and compared to the total number of observed events.

6.1   Diboson Events

$WW + jets \rightarrow \mu\mu + \nu\nu + jets$ (WW) and $WZ + jets \rightarrow \mu\mu + \nu + jets$ (WZ), collectively referred to as diboson backgrounds, have two isolated muons, at least two jets, and real $\not{E}_T$. Thus, these backgrounds have the same event signature as $t\bar{t} \rightarrow \mu\mu + \nu\nu + jets$ and are physics backgrounds.

The diboson background yields are estimated using the Monte Carlo samples detailed in Section 4.4.2. Events in these samples are required to pass the same set of selection criteria as signal events (Chapter 5). The Monte Carlo yield after all selection cuts have been applied is written N_{Raw}. However, in order to fairly compare this yield to selected data events, it must be normalized. The normalized yield, N_{Norm} is computed from N_{Raw} as:

$$N_{Norm} = \left(\frac{\sigma \times BR \times \kappa \times \mathcal{L}_{Int}}{N_{events}} \right) \times N_{Raw}. \tag{6.1}$$

Here, $\mathcal{L}_{Int}$ is the integrated luminosity of the data used for the measurement, and N_{events} is the number of events in the Monte Carlo sample. The product of the theoretical cross section and the branching ratio of the Monte Carlo process, $\sigma \times BR$, is given in Table 4.6. Finally, κ is an overall data-to-Monte Carlo scale factor, defined as:

$$\kappa = \kappa_{\mu ID} \times \kappa_{trk-match} \times \kappa_{trk-\chi^2} \times \kappa_{PV} \times \kappa_{root-reco} \times \kappa_{lv} \times \kappa_{DCA} \times \kappa_{Iso} \tag{6.2}$$

where the individual factors are described in Section 5.1.1. For diboson events, $\kappa = 0.92$. Note that because $\kappa_{trk-match}$ is parameterized and treated as an event weight, its value differs slightly between diboson events and $t\bar{t}$ events.

The diboson yield after all cuts is:

$$N_{WW/WZ} = 0.19 \pm 0.03(stat)^{+0.09}_{-0.06}(sys) \tag{6.3}$$

where the statistical error is the Gaussian error on the number of selected Monte Carlo events and the systematic error is obtained by summing in quadrature all of the individual systematic uncertainties that are discussed in Section 7.2.

Cut	WW	WZ	Total
$N_\mu^{p_T>15} \geq 2$	19.280 ± 0.241	—	—
$+N_{jets}^{p_T>20} \geq 1$	1.631 ± 0.067	—	—
Preselection	0.784 ± 0.060	1.753 ± 0.046	2.537 ± 0.076
$+\chi_Z^2$ Cut	0.561 ± 0.049	0.119 ± 0.012	0.680 ± 0.051
+ Contour Cut	0.188 ± 0.030	0	0.188 ± 0.030

TABLE 6.1. Expected diboson background yields for several selection cut levels shown with statistical error. The WZ yield was not estimated for the first two lines in the table because an appropriate Monte Carlo sample was not available.

After all selection criteria, the diboson yield is 15 times smaller than the expected signal yield. In part, the relatively small contribution of this background is attributable to a low diboson production cross section. Also, requiring two high P_T jets suppresses the WW background since the jets in this background tend to have a softer P_T spectrum than those in signal events. Table 6.1 shows the expected diboson background yields for several successive selection cut levels. As expected, there is a sharp decrease in WW yield between lines 1 and line 2, corresponding to the requirement of the first high P_T jet.

Despite a harder jet P_T spectrum and larger branching fraction than the WW background, the WZ background is negligible after all selection cuts are applied. This is because the χ_Z^2 cut (Section 5.2.1) targets the Z boson's decay, suppressing this background.

6.2 Z/γ^* Background

Another background that shares the $t\bar{t} \rightarrow \mu\mu + \nu\nu + jets$ signal is $Z/\gamma^* + jets \rightarrow$ $\tau\tau + jets \rightarrow \mu\mu + \nu\nu\nu\nu + jets$ $(Z/\gamma^* \rightarrow \tau\tau)$. These events have two isolated muons and significant $\not{E}_T$. However, the low branching ratio of $(\approx 17\%)$ for each τ lepton to decay to a muon helps to suppress the overall background yield [33]. Also, the P_T spectrum of the resulting muons is softer than that in signal so requiring two high P_T

muons further reduces this background.

A more significant background is direct $Z/\gamma^* + jets \rightarrow \mu\mu + jets$ decay ($Z/\gamma^* \rightarrow \mu\mu$). These events have two high P_T, isolated muons and can have two jets, but do not have any real $\not{E}_T$ from neutrinos. Therefore, fake $\not{E}_T$ from instrumental effects must be present for $Z/\gamma^* \rightarrow \mu\mu$ events to pass selection criteria. Such effects include calorimeter noise, poor jet energy resolution, hardware malfunctions in calorimeter readout, and poor muon momentum resolution (Section 4.3.6). Despite the χ^2_Z cut and contour cut described in (Section 5.2) specifically targeting this background, it remains the dominant background to the measurement. Its yield is nearly twice as large as the next most significant background.

Both the $Z/\gamma^* + jets \rightarrow \tau\tau + jets$ and $Z/\gamma^* + jets \rightarrow \mu\mu + jets$ backgrounds are estimated with the Monte Carlo samples described in Section 4.4.2. The P_T of the jets are reweighted in order to better describe the jets' transverse momenta in data (Section 6.2.1). Also, since the backgrounds are estimated with Monte Carlo, the raw yields must be normalized according to Equation 6.1. However, the data-to-Monte Carlo correction factor is not identical to the κ applied to diboson backgrounds and signal events. Instead, it is estimated independently because of the availability of a Z/γ^* control sample in data. This scale factor is called K_Z and is described in Section 6.2.2.

6.2.1   Jet P_T Reweighting

In the Alpgen $Z/\gamma^* \rightarrow \tau\tau$ and $Z/\gamma^* \rightarrow \mu\mu$ Monte Carlo samples (Table 4.7), the jet P_T distributions of preselected events in the Z boson mass window of 75 to 105 GeV are softer than those in the corresponding data sample [49]. To account for this, Monte Carlo samples are reweighted with respect to the transverse momenta distributions of the highest P_T and second-highest P_T jet. Because the jet identification corrections (Section 4.3.4) would increase the jet P_T discrepancies between data and Monte Carlo,

they are not applied for these samples [51]. Figure 6.1 shows the jet P_T distributions and also the $\not{E}_T$ distributions for both reweighted and unreweighted Monte Carlo. It can be easily seen that the reweighted samples more accurately reproduce the behavior of data.
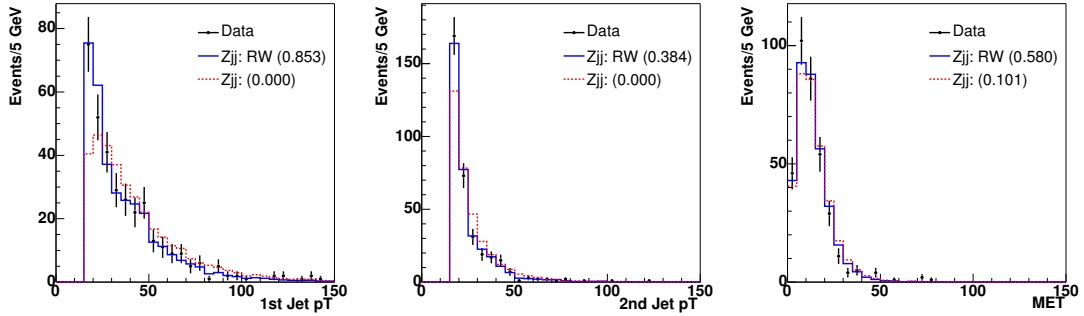
FIGURE 6.1. Data and normalized Monte Carlo distributions of the highest P_T and second-highest P_T jet, as well as the $\not{E}_T$ distribution. The dashed lines represent unreweighted Monte Carlo, while the solid histograms represent reweighted Monte Carlo. Kolmogorov statistics that test the compatibility of data and Monte Carlo distributions are displayed in parentheses [51].

6.2.2 K_Z Factor

The K_Z factor is a data-to-Monte Carlo scale factor used to normalize the Alpgen $Z/\gamma^* \to \tau\tau$ and $Z/\gamma^* \to \mu\mu$ Monte Carlo samples. It is calculated by taking the ratio of the number of data and normalized $Z/\gamma^* \to \mu\mu$ Monte Carlo events that have passed preselection requirements (Section 5.1) and have a dimuon invariant mass in the window of 70 to 110 GeV. Since the Alpgen $(Z/\gamma^* \to \mu\mu)$jj Monte Carlo samples are separated into three exclusive mass bins (Table 4.7), the sum of events meeting the above requirement in each sample is taken as the Monte Carlo yield. The data-to-Monte Carlo ratio is the K_Z factor for Z/γ^* events with two or more jets.

This process is repeated for the three $(Z/\gamma^* \to \mu\mu)$j samples (Table 4.7), with the exception that the preselection requirements are loosened to only require one jet.

This gives a second K_Z factor that is used to normalize the $Z/\gamma^* \to \mu\mu$ background at the ≥ 1 jet selection level. Both K_Z factors are given in Table 6.2.

Since the K_Z factor is estimated from preselected yields, it implicitly accounts for most of the data-to-Monte Carlo scale factors described in Section 5.1.1. Therefore, for samples normalized with the K_Z factor, only $\kappa_{trk-match}$ and $\kappa_{trk-\chi^2}$ have been applied.

Note that the K_Z factor is not used to normalize the Pythia Monte Carlo samples employed in data-to-Monte Carlo cross-checks. Rather, these samples are normalized with the same scale factor as the diboson background (Section 6.1).

Jet Multiplicity	Observed Yield	Expected Yield	K_Z
≥ 1	2349	2106.96	1.115 ± 0.026
≥ 2	305	342.18	0.891 ± 0.052

TABLE 6.2. The K_Z factors, and the number of observed and predicted yields used to derive them in the ≥ 1 and ≥ 2 jet bins.

6.2.3 Z/γ^* Yields

The Z/γ^* Monte Carlo samples are used to estimate the fraction of Z/γ^* events that pass selection cuts. The final normalized yields of $Z/\gamma^* \to \tau\tau$ and $Z/\gamma^* \to \mu\mu$, after all selection criteria have been applied, are given in Table 6.3 and Table 6.4, respectively. In each table, the product of the cross section and branching ratio used for Monte Carlo normalization is listed for reference. Note that 'Selected Events' corresponds to the sum of the jet P_T weights described in Section 6.2.1, while the final expected yields takes into account all scale factors including the K_Z factor, described in Section 6.2.2. Including the systematic uncertainties discussed in Section 7.2, the final combined yield of Z/γ^* backgrounds is:

$$N_{Z/\gamma^*(\tau,\mu)} = 0.47 \pm 0.08(stat)^{+0.14}_{-0.16}(sys). \tag{6.4}$$

The combined yield at various cut levels can be found in Table 6.6.

	$M_{\mu\mu}(GeV)$	$\sigma \times BR$ (pb)	Generated Events	Selected Events	Expected Yield
$Z/\gamma^* \to \tau\tau$	15-60	3.060	12033	0	0
	60-130	2.899	68127	9.3	0.149 ± 0.033
	>130	0.025	2042	2.1	0.010 ± 0.006
				Total $Z/\gamma^* \to \tau\tau$	0.158 ± 0.033

TABLE 6.3. Total expected background from $Z/\gamma^* \to \tau\tau$ after all cuts have been applied, separated by mass bin, together with statistical uncertainty. The number of generated events refers to the number of events in the Monte Carlo sample that decayed leptonically.

	$M_{\mu\mu}(GeV)$	$\sigma \times BR$ (pb)	Generated Events	Selected Events	Expected Yield
$Z/\gamma^* \to \mu\mu$	15-60	24.7	233500	1.8	0.071 ± 0.051
	60-130	23.4	269500	4.2	0.138 ± 0.054
	>130	0.2	66500	91.7	0.104 ± 0.010
				Total $Z/\gamma^* \to \mu\mu$	0.313 ± 0.075

TABLE 6.4. Total expected background from $Z/\gamma^* \to \mu\mu$ after all cuts have been applied, separated by mass bin, together with statistical uncertainty.

6.3   Fake Isolated Muon Background

Other types of instrumental background include QCD multijet production, primarily the heavy flavor decay of $b\bar{b}$ and $c\bar{c}$ events, and W + jets production. Events in these backgrounds have at most one isolated muon that does not originate from a jet. However, muons from semileptonic flavor decays may sometimes pass isolation criteria (Section 4.3.3). In order to pass all selection cuts, W + jets events need at least one such fake isolated muon, while QCD multijet production requires at least two fake isolated muons as well as fake $\not{E}_T$. Despite the high production cross section of multijet events at the Tevatron, both these and W + jets events constitute very small backgrounds to $t\bar{t} \to \mu\mu$ decays.

The fake isolated muon yield is unique among the background yields in that it is

estimated using primarily data. A 'matrix method', consisting of two equations with four inputs, is used [49]. The first input is the efficiency for real isolated muons to pass the isolation criteria, ϵ_{iso}. Note that ϵ_{iso} includes both muons from signal events and those in the Z/γ^* backgrounds since each of these sources has real isolated muons. ϵ_{iso} is measured in a Pythia $Z/\gamma^* \to \mu\mu$ sample for the zero and one inclusive jet multiplicities. For ≥ 2 jets, Alpgen $t\bar{t}$ Monte Carlo is used. The results are listed in Table 6.5.

Jet Multiplicity	$\epsilon_{iso}(\%)$	f_μ (%)
≥ 0	96.4 ± 0.1	0.56 ± 0.07
≥ 1	91.9 ± 0.3	0.34 ± 0.05
≥ 2	87.0 ± 0.4	0.18 ± 0.05

TABLE 6.5. Efficiency for real isolated muons to pass isolation criteria, ϵ_{iso}, and the rate that non-isolated muons pass the isolation criteria, f_μ for three inclusive jet multiplicity bins.

The second input to the matrix method is the rate at which non-isolated muons pass the isolation criteria, f_μ [49]. This is known as the fake rate. Like ϵ_{iso}, f_μ is measured for each of three inclusive jet multiplicities, but the fake rate is measured in signal-triggered data events rather than in Monte Carlo. Since the goal is to measure the isolation probability for muons which are actually non-isolated (from QCD multijet and W + jets production), the measurement is done for events in which the highest P_T muon fails the isolation requirements (Section 4.3.3). The fake rate is then extracted by measuring the isolation efficiency of the second-highest P_T muon. Special care is taken to suppress contamination from Z/γ^* events, by requiring the dimuon invariant mass to be less than 70 GeV, significantly below the mass of the Z boson.

Figure 6.2 shows a scatter plot from data events of the two isolation variables defined in Section 4.3.3, E_{halo}^{trk} ('Track Halo') and E_{halo}^{cal} ('Cal Halo'), for the highest P_T muon, with lines marking the maximum allowable values for a muon to be considered

isolated (0.12). Events in which the second-highest P_T muon is isolated are denoted with circles. Figure 6.3 illustrates the fake rate calculation. The histogram shows the value E_{halo}^{cal} of the highest P_T muon for events in which this muon is non-isolated in E_{halo}^{trk}. The dark histograms represent events in which the second-highest P_T muon is isolated. The fake rate is calculated as the ratio of dark to light histograms in the region above the isolation criteria.

The fake rates for each jet multiplicity bin are given in Table 6.5.
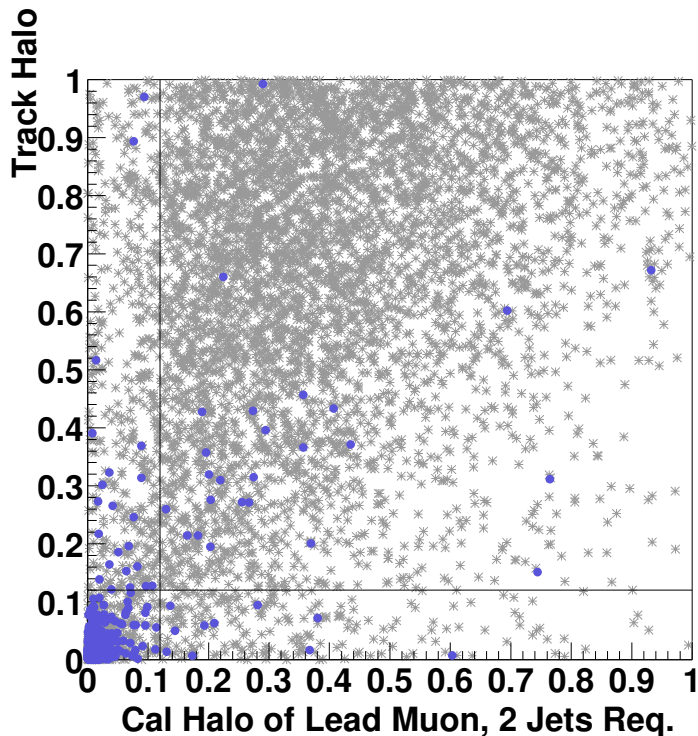
FIGURE 6.2. Scatter plot of the two isolation variables introduced in Section 4.3.3. The vertical lines indicate the isolation requirement. Asterisks include all events, while circles indicate events for which the second-highest P_T muon is isolated.

The remaining two inputs to the matrix method are the 'tight' and 'loose' data yields. The tight yield, N_T, contains signal-triggered events that pass all selection cuts including full isolation requirements. Two events make up the tight yield. The loose yield, N_L, includes events for which only one muon is required to pass isolation
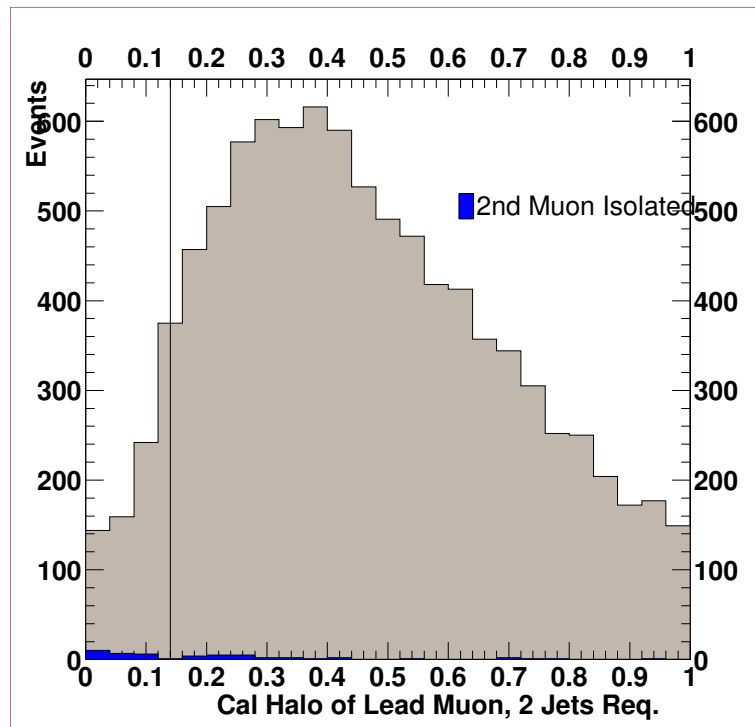
FIGURE 6.3. Distribution of E_{halo}^{cal} for the highest P_T muon. The light histogram represents all events for which $E_{halo}^{track} > 0.12$ for the highest P_T muon, while the dark histogram shows only those events where the second-highest P_T muon is isolated.

criteria. Ten such events make up the loose yield. The two matrix equations are:

$$N_L = N^{Z+top} + N^{W+QCD} \tag{6.5}$$

$$N_T = \epsilon_{iso} N^{Z+top} + f_\mu N^{W+QCD} \tag{6.6}$$

where N^{Z+top} is the number of events with real isolated muons, and N^{W+QCD} is the number of events with fake isolated muons.

Eliminating N^{Z+top}, and solving for N^{W+QCD} gives:

$$N^{W+QCD} = \frac{N_T - \epsilon_{iso} N_L}{f_\mu - \epsilon_{iso}} \tag{6.7}$$

The total number of QCD multijet and W+jets events expected in the final data sample is given by the number of fake isolated muon events multiplied by the rate at which they pass isolation criteria, $N^{W+QCD} \times f_\mu$. The result is :

$$N_{QCD,W+jets} = 0.014 \pm 0.006(stat) \pm 0.004(syst)$$

where the systematic uncertainty on the yield is calculated from the statistical uncertainty on f_μ. The statistical uncertainty on the yield is calculated from a negative log-likelihood minimization using Poisson statistics to express the probability of observing the loose and tight data yields (Equation 6.5). The method is the same as the one used to calculate the statistical error for the cross section measurement (Chapter 7) and is further detailed in [77]. Of all the backgrounds, the fake isolated muon background has the smallest expected yield in the final data sample. It is effectively eliminated by the isolation requirements.

6.4   Data and Monte Carlo Comparisons

The total expected event yield is the sum of the predicted signal yield (Chapter 5) and the total predicted background yield, calculated by summing the individual background contributions (Section 6.1 to Section 6.3). The first two columns of Table 6.6

list the number of observed events and the total expected yield for five different selection cut levels. Agreement is within 2σ at the first level of selection after only muon identification requirements have been applied. Agreement is better in the next two lines, although these agree by construction (Section 6.2.2). At the fourth line, after the χ^2_Z cut is applied, the expected and observed yields differ by 2–3σ. Since the Gaussian probability for observing a 3σ difference is less than 1%, extensive tests were conducted in a high statistics control sample to verify that the χ^2_Z distribution is well modeled [80]. This was confirmed so the difference in expected and observed yields at this cut level is treated as a statistical fluctuation. Reasonable agreement is observed at the final level of selection, where Poisson statistics have to be taken into account.

In addition to comparing yields, it is important to ensure that the shape of kinematic distributions–particularly those relevant to the selection cuts–is consistent between observed and predicted events. To this end, nine such example distributions are shown for three different selection cut levels. In each plot, observed events are displayed as points, while histograms represent predicted signal and background yields. Figures 6.4 to 6.7 show distributions at the preselection level. Figures 6.8 to 6.11 show the distributions after all selection criteria have been required. Reasonable shape agreement is observed between data and prediction in the first set of plots. After full selection, there are only two data points in the sample, rendering it ineffective for comparing the distribution shapes. However, note that in the preselection figures the dominant yield is $Z/\gamma^*(\tau, \mu)$, while after full selection, $t\bar{t}$ events dominate.

6.5   Results

The yields after all selection criteria have been applied are summarized in Table 6.7. Two data events are observed for an expected yield of 3.6 events. As stated in Section 6.2, $Z/\gamma^*(\tau, \mu)$ constitutes the largest source of background events. However,

Cut	Data	All	Z/γ^* (μ or τ)	Fake Isolated Muon Bkg	WW/WZ	$t\bar{t}$
$N_\mu^{p_T>15} \geq 2$	21910	27383 $\pm$2922	27333$\pm$2919	20.22$\pm$2.56	19.28$\pm$6.06	10.29$\pm$0.91
$+N_{jets}^{p_T>20} \geq 1$	2938	2800$\pm$94.4	2782$\pm$94.1	6.47$\pm$0.96	1.63$\pm$0.58	10.19$\pm$0.90
Preselection	387	382.8$\pm$23.9	371.1$\pm$23.6	1.61$\pm$0.45	2.54 $\pm$0.84	7.56$\pm$0.69
$+\chi_Z^2$ cut	96	$74.8^{+7.48}_{-6.65}$	$67.13^{+7.14}_{-6.30}$	$1.54^{+0.43}_{-0.43}$	$0.68^{+0.24}_{-0.24}$	$5.45^{+0.48}_{-0.50}$
+ Contour Cut	2	$3.64^{+0.49}_{-0.51}$	$0.47^{+0.17}_{-0.18}$	$0.01^{+0.01}_{-0.01}$	$0.19^{+0.10}_{-0.07}$	$2.96^{+0.31}_{-0.35}$

TABLE 6.6. Observed and expected yields at five successive levels of selection. The errors shown are statistical and systematic uncertainties (Section 7.2) added in quadrature.
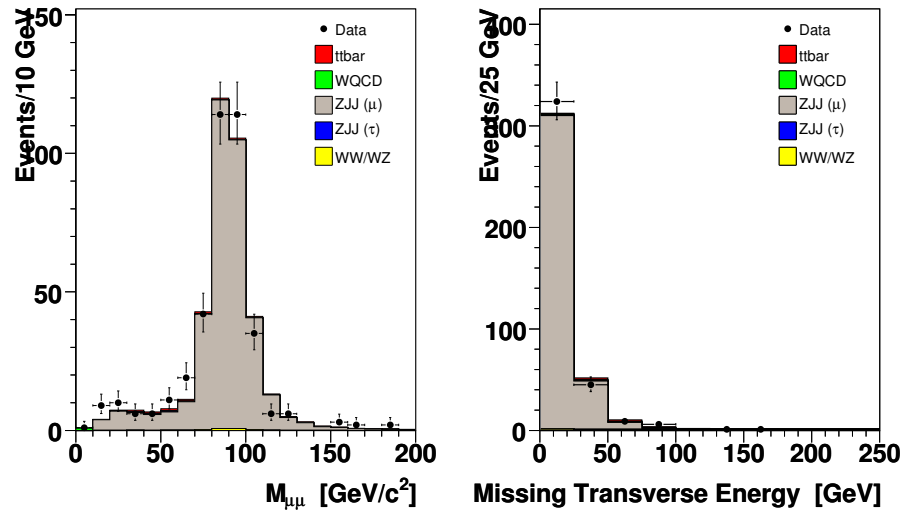
FIGURE 6.4. Expected and observed yields after preselection for the dimuon invariant mass distribution (left) and $\not{E}_T$ distribution (right).
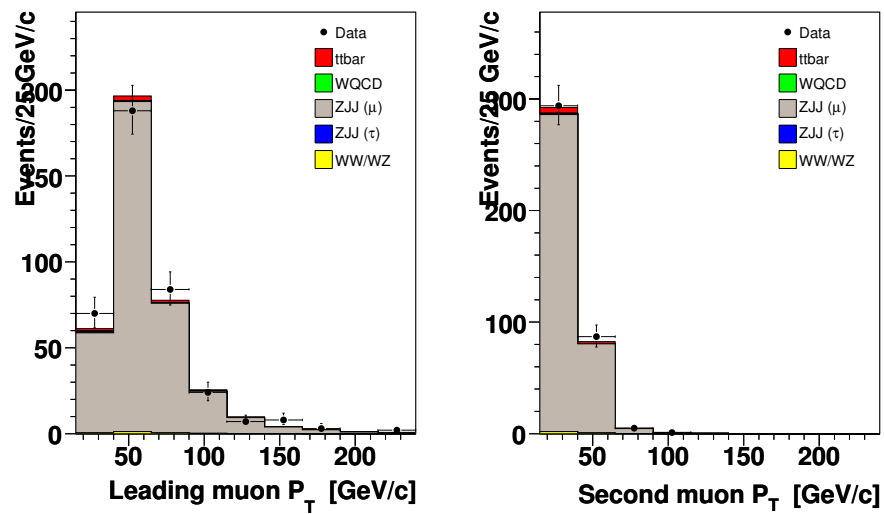
FIGURE 6.5. Expected and observed yields after preselection for the P_T distribution of the highest (left) and second-highest (right) P_T muon.
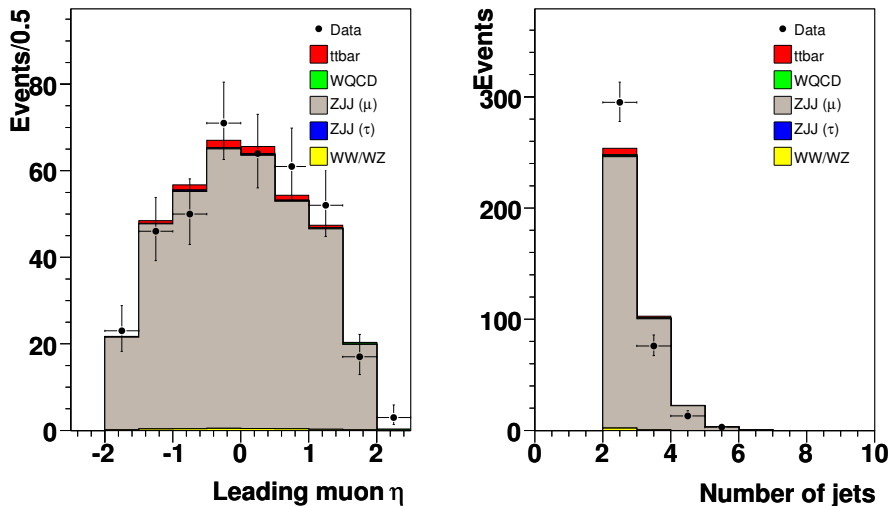
FIGURE 6.6. Expected and observed yields after preselection for the η distribution of the highest P_T muon (left) and the jet multiplicity distribution (right).
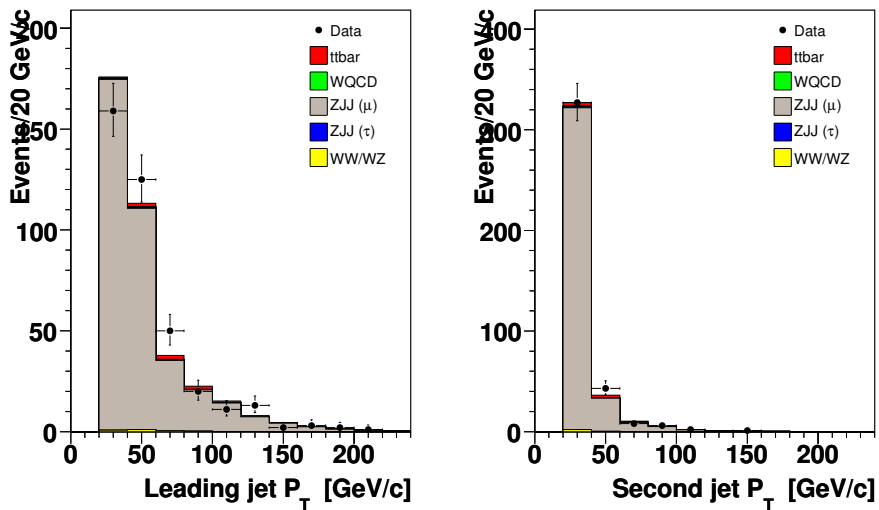
FIGURE 6.7. Expected and observed yields after preselection for the P_T distribution of the highest (left) and second-highest P_T jet (right).
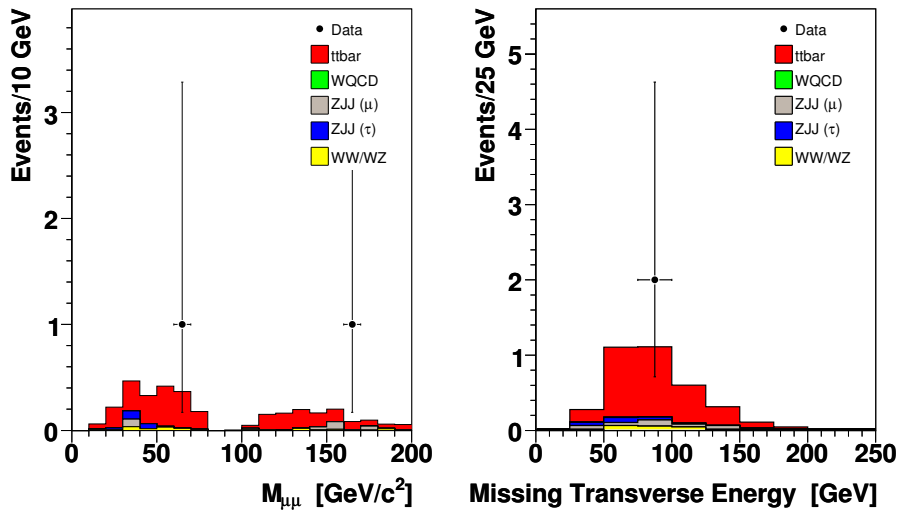
FIGURE 6.8. Expected and observed yields after full selection for the dimuon invariant mass distribution (left) and $\not{E}_T$ distribution (right).
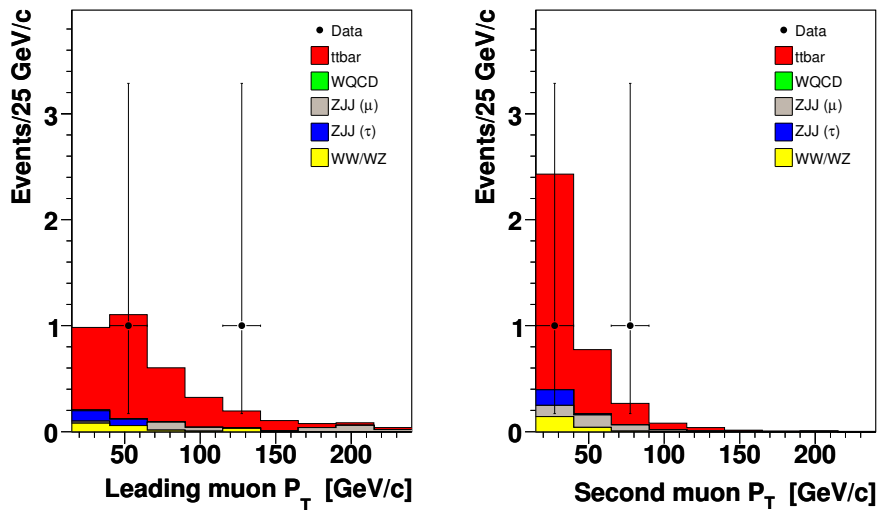
FIGURE 6.9. Expected and observed yields after full selection for the P_T distribution of the highest (left) and second-highest (right) P_T muon.
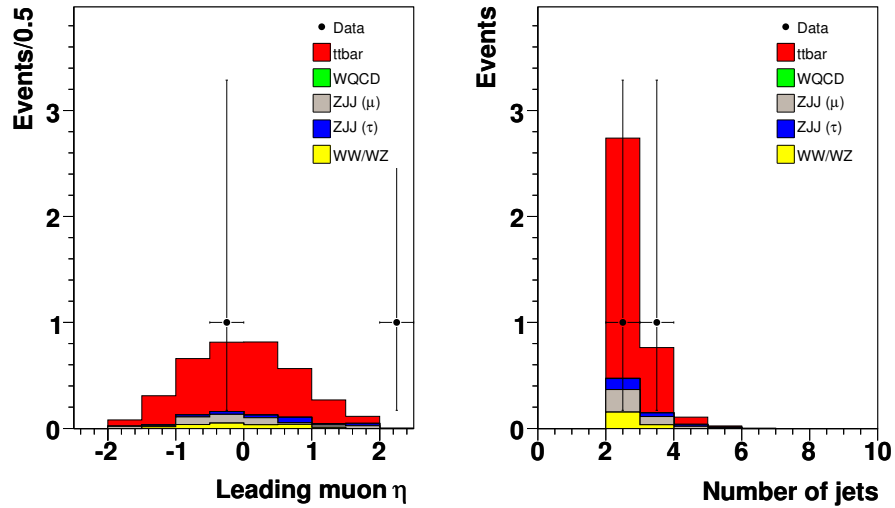
FIGURE 6.10. Expected and observed yields after full selection for the η distribution of the highest P_T muon (left) and the jet multiplicity distribution (right).
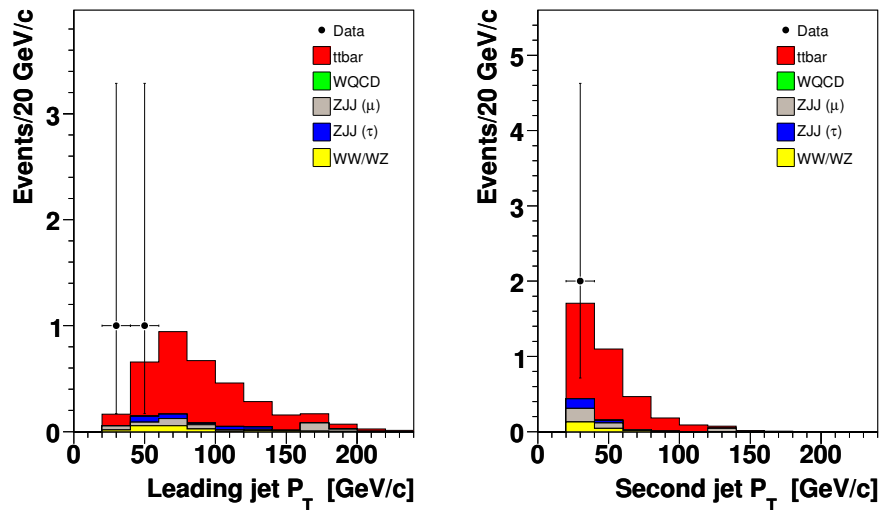
FIGURE 6.11. Expected and observed yields after full selection for the P_T distribution of the highest (left) and second-highest P_T jet (right).

the χ^2_Z and contour cut help suppress both these and the diboson backgrounds. After all selection criteria have been applied, the final expected signal-to-background ratio is more than four-to-one.

Figure 6.12 shows the expected and observed yields for exclusive jet multiplicity bins after all selection requirements have been applied. Including all three bins, two events are observed for an expected yield of just under seven events. Assuming a Poisson distribution, the probability of observing two events for this expected yield is around two percent. Of course, only the bin with at least two jets in Figure 6.12 is used in the measurement. Again assuming Poisson statistics, the probability for observing two events for an expected yield of 3.6 events is 18%.

Category	Yield	Stat Err	Sys Err
WW/WZ	0.188	0.030	$+0.092$ -0.062
Z/γ^* (μ or τ)	0.471	0.082	$+0.144$ -0.155
WQCD (Isolation Fakes)	0.014	0.006	$+0.004$ -0.004
Total Bkg	0.673	0.087	$+0.224$ -0.206
Expected signal	2.962	0.079	$+0.297$ -0.338
Selected Events	2	–	–

TABLE 6.7. Observed and expected signal and background yields after all selection criteria have been applied. The systematic uncertainties are discussed in Section 7.2.
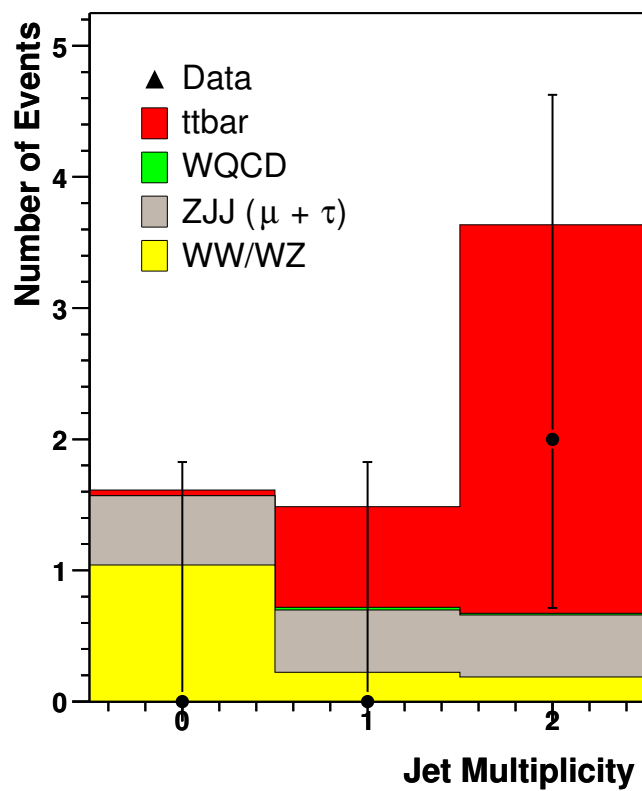
FIGURE 6.12. The expected and observed yields after all selection criteria are applied in the three jet multiplicity bins: 0 jets, 1 jet, and $\geq$ 2 jets.

Chapter 7

The Measurement

As stated in Chapter 1, the top quark pair production cross section is given by:

$$\sigma_{t\bar{t}} = \frac{(N_{obs} - N_{bkg})}{\epsilon_{sig} \times BR(t\bar{t} \to \mu\mu) \times \mathcal{L}_{Int}} \tag{7.1}$$

where N_{obs} is the number of observed events in the data after all selection cuts are applied, N_{bkg} is the estimated background yield, ϵ_{sig} is the efficiency of the selection cuts in signal events, $BR(t\bar{t} \to \mu\mu)$ is the branching ratio of the process (including $W \to \tau \to \mu$ decays), and $\mathcal{L}_{Int}$ is the integrated luminosity of the data set. These quantities have been measured and presented in Chapters 5 and 6. In this chapter, the cross section is determined. The sources of systematic uncertainty on the cross section are discussed. For completeness, event displays of the candidate events are shown. Finally, the cross section measurement is compared with theoretical predictions.

7.1   Measurement

Channel	N_{obs}	N_{bkg}	ϵ_{sig}	Br	$\mathcal{L}$ (pb^{-1})
$\mu\mu$	2	$0.67^{+0.24}_{-0.22}$	0.064 ± 0.002	0.01571 ± 0.00031	421.4 ± 25.7

TABLE 7.1. The inputs to the cross section measurement. The error on the estimated background yield includes statistical and systematic uncertainties (Section 7.2) added in quadrature. The error shown on the signal efficiency is statistical only.

The cross section can be calculated directly from Equation 7.1 with the inputs summarized in Table 7.1. However, it is advantageous to instead extract the cross section by minimizing a negative log-likelihood using Poisson statistics. This approach has an accepted prescription for calculating a meaningful statistical uncertainty for a

small data set and also facilitates a straightforward combination of individual sources of systematic uncertainty (Section 7.2).

Specifying μ to be $\mu = \sigma_{t\bar{t}} BR \mathcal{L} \epsilon_{sig} + N^{bkg}$, a likelihood function can be defined as [78]:

$$\mathrm{L}(\sigma, \{N^{obs}, N^{bkg}, BR, \mathcal{L}, \epsilon_{sig}\}) \;\; = \;\; \mathcal{P}(N^{obs}, \mu) = \frac{\mu^{N^{obs}}}{N^{obs}!} \, e^{-\mu}, \tag{7.2}$$

and $\mathcal{P}(N^{obs}, \mu)$ is the Poisson probability that the expected signal plus background yield is equal to μ.

The cross section can then be found by minimizing the negative logarithm of the above likelihood:

$$-\log \mathrm{L}(\sigma, \{N^{obs}, N^{bkg}, BR, \mathcal{L}, \epsilon\}) \;\; \approx \;\; -N^{obs} \log \mu + \mu \tag{7.3}$$

where the terms independent of the cross section have been dropped. Figure 7.1 illustrates the likelihood minimization. The statistical uncertainty is calculated by varying the negative log-likelihood by half a unit above the minimum, which corresponds to one standard deviation ($\pm 1\sigma$). In the figure, vertical lines mark the statistical uncertainty on the measurement.

The individual sources of systematic uncertainty on the background estimate, N_{bkg}, and the signal efficiency, ϵ_{sig}, are discussed in the next section (Section 7.2). In order to calculate the total systematic uncertainty on the cross section, N_{bkg} and ϵ_{sig} are each varied within their errors (Table 7.2 and Table 7.3), and the likelihood minimization is repeated. The variation is performed taking into account the correlations between the signal efficiency and the different background yields for individual sources of systematic uncertainty. Certain errors, such as the error on the fake isolated muon background and the error arising from limited Monte Carlo statistics, are uncorrelated [78].

The final cross section measurement, assuming a top mass of 175 GeV (Section 7.2), is:

$$\sigma_{t\bar{t}} = 3.13^{+4.17}_{-2.60}(stat)^{+0.92}_{-0.86}(sys) \pm 0.19(lumi)\mathrm{pb}. \tag{7.4}$$

The third error on the cross section is the uncertainty associated with estimating the integrated luminosity of the data set.
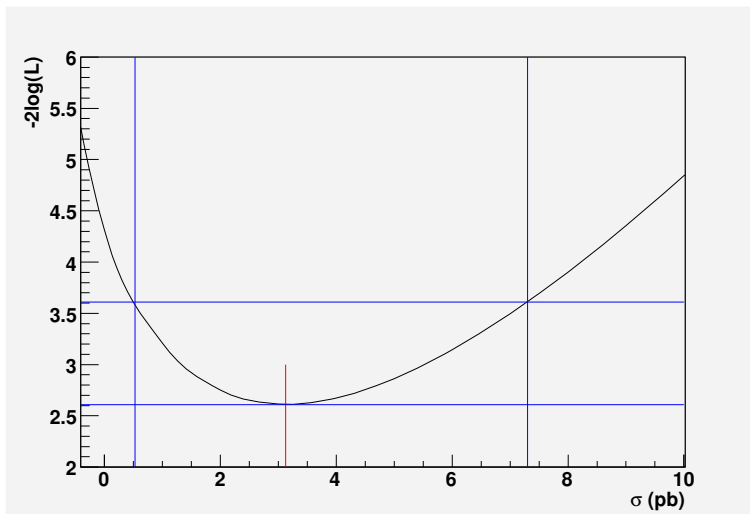
FIGURE 7.1. The negative log-likelihood used to extract the cross section. The minimum is marked with a short vertical line, while long vertical lines indicate the statistical uncertainties on the cross section. Since the figure displays the log likelihood multiplied by a factor of two, the statistical uncertainty (as pictured) corresponds to a variation of one unit above the minimum.

7.2   Systematic Uncertainty

The total systematic uncertainty on the cross section measurement, discussed in Section 7.1, includes the uncertainties on the the signal efficiency measurement as well as those on the background yield. These are presented in Table 7.2 and Table 7.3, respectively. The individual sources of systematic errors in the tables are described below and in [51]. For convenience, they are grouped into three categories based on the method used to estimate them. The dominant systematic uncertainties for both the signal efficiency and the background yield are from jet reconstruction and our limited understanding of these procedures, including the calibration of the jet energy scale and the jet energy resolution (Section 4.3.4).

Source	$t\bar{t}$
μ ID	± 3.0
μ tracking	± 2.5
χ^2	± 0.2
μ isolation	± 0.8
μ σ_{dca}	± 0.6
Primary vertex	± 0.4
$\Delta z(D\!\O reco, D\!\O root)$	± 0.2
Lepton promptness	± 0.1
μ smearing	-0.2 $+0.1$
Level 1 trigger	$+3.9$ -4.8
Level 2 trigger	$+0.2$ -0.4
JES	$+5.7$ -7.4
Jet ID	$+0.4$ -4.9
Jet energy resolution	-2.5 -1.4
Uncorrelated	$\pm$ 3.1

TABLE 7.2. Summary of the relative systematic uncertainties on the $t\bar{t} \rightarrow \mu\bar{\mu}$ signal efficiencies in %. When two uncertainties are quoted, the left uncertainty corresponds to a positive variation in the error (i.e. $+\sigma$) and the right corresponds to a negative variation in the error (i.e $-\sigma$).

Source	WW	Z/γ^* (μ or τ)
μ ID	±3.0	N/A
μ tracking	±2.5	N/A
χ^2	±0.2	N/A
μ isolation	±0.8	N/A
μ σ_{dca}	±0.6	N/A
Primary vertex	±0.4	N/A
$\Delta z(D\emptyset reco, D\emptyset root)$	±0.2	N/A
Lepton promptness	±0.1	N/A
μ smearing	$-3.9\ 0.0$	$+25.4\ -20.9$
Level 1 trigger	$+4.9\ -5.7$	$-1.3\ +1.4$
Level 2 trigger	$+0.3\ -0.5$	$-0.3\ +0.3$
JES	$+37.3\ -10.8$	$+15.9\ -24.7$
Jet ID	$+57.8\ +53$	N/A
Jet energy resolution	$+22.1\ +21.1$	$+26.3\ +13.2$
Theoretical cross sections/ Normalization	±35.0	±5.8
Uncorrelated	±13.0	

TABLE 7.3. Summary of the relative systematic (in %) uncertainties on background. When two uncertainties are quoted, the left uncertainty corresponds to a positive variation in the error (i.e. $+\sigma$) and the right corresponds to a negative variation in the error (i.e $-\sigma$).

The following systematic errors are those associated with the data-to-Monte Carlo scale factors presented in Section 5.1.1.

Muon Identification (μ ID) Recall from Section 5.1.1 that the scale factor, $\kappa_{\mu ID}$, is calculated from a flat fit to the ratio of muon identification efficiencies in data and Monte Carlo as a function of muon detector η. Figure 5.2 shows the distribution of these efficiency ratios. The root mean square deviation of this distribution is taken as the systematic error.

Muon Tracking (μ tracking) $\kappa_{trk-match}$ is derived from the ratio of data-to-Monte Carlo muon track matching efficiencies, parameterized in η and ϕ. The systematic error is computed by allowing the statistical error from each $\eta - \phi$ bin in the parameterization to fluctuate up and down by 1σ.

Track χ^2 The systematic error is taken as the statistical error on the scale factor, $\kappa_{trk-\chi^2}$.

Muon Isolation As above, the statistical uncertainty on the scale factor, κ_{iso}, is taken as the systematic uncertainty. This approach is considered reasonable since the scale factor is consistent with or without the $\Delta R(\mu, jet) > 0.5$ requirement, meaning it is well modeled.

μ σ_{DCA} The systematic is taken from the statistical uncertainty of the scale factor, κ_{DCA}, in the one jet multiplicity bin.

Primary Vertex Recall from Section 5.1.1, that a common primary vertex scale factor is used in the dimuon and dielectron channels. Since the scale factors calculated with $Z \rightarrow \mu\mu$ and $Z \rightarrow ee$ events are not consistent within errors, half of the difference between these scale factors is taken to be the systematic uncertainty on the combined scale factor (Table 5.4).

$\boldsymbol{\Delta z(D\varnothing_{reco}, D\varnothing_{root})}$ Again, the systematic is estimated as half the difference between $Z \to \mu\mu$ and $Z \to ee$ scale factors.

Lepton Promptness This error is taken from the statistical error on the scale factor, $\kappa_{PV,l}$, since there is no significant difference between the $Z \to \mu\mu$ and $Z \to ee$ scale factors for any of the jet multiplicities examined.
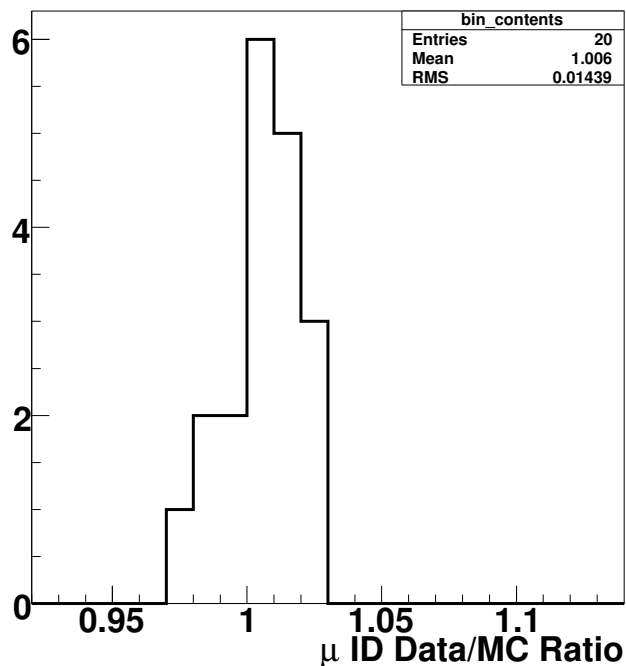
FIGURE 7.2. The distribution of data-to-Monte Carlo muon identification efficiencies, taken from Figure 5.2.

The following systematic errors are estimated by varying the appropriate parameters or curves by an integer number of standard deviations from the central value.

Muon Momentum Smearing The muon smearing (Section 4.3.3) systematic can be estimated by varying the smearing parameters by $\pm 1\sigma$.

Level 1 Trigger The statistical errors on trigger efficiency fit functions, Figure 5.9, are varied by $\pm 2\sigma$. Two standard deviations are chosen because one standard deviation does not adequately cover the fluctuations in the fit.

Level 2 Trigger Same as for Level 1. The corresponding figure is Figure 5.10.

Jet Energy Scale (JES) The jet energy scale parameters are varied by $\pm 1\sigma$ of the total uncertainty, which includes statistical and systematic components for both the data and Monte Carlo corrections as:

$$\sigma = \sqrt{\sigma_{data}^2 + \sigma_{MonteCarlo}^2}.$$

(7.5)

Figure 7.3 shows σ_{data} and $\sigma_{MonteCarlo}$ with the contributions of the three subcorrections (Section 4.3.4) to the uncertainties marked.

Jet Identification The jet identification scale factor is the ratio of the probability to reconstruct and identify a jet in data and Monte Carlo. It is calculated as a function of $\not{E}_T$, separately for jets reconstructed in the central calorimeter, endcap calorimeter, and inner-cryostat detectors [51]. The systematic error is estimated with separate Monte Carlo samples that incorporate a jet identification scale factor $\pm 1\sigma$ from the central value.

Jet Energy Resolution The jet energy smearing parameters are varied by $\pm 1\sigma$. As for jet identification, separate Monte Carlo samples with the σ variations implemented are used to estimate the systematic uncertainty.

The following is a description of additional sources of systematic uncertainty considered for the cross section measurement.

Uncorrelated The uncorrelated error accounts for uncertainty in the systematic errors due to limited Monte Carlo statistics. It is calculated for signal, as
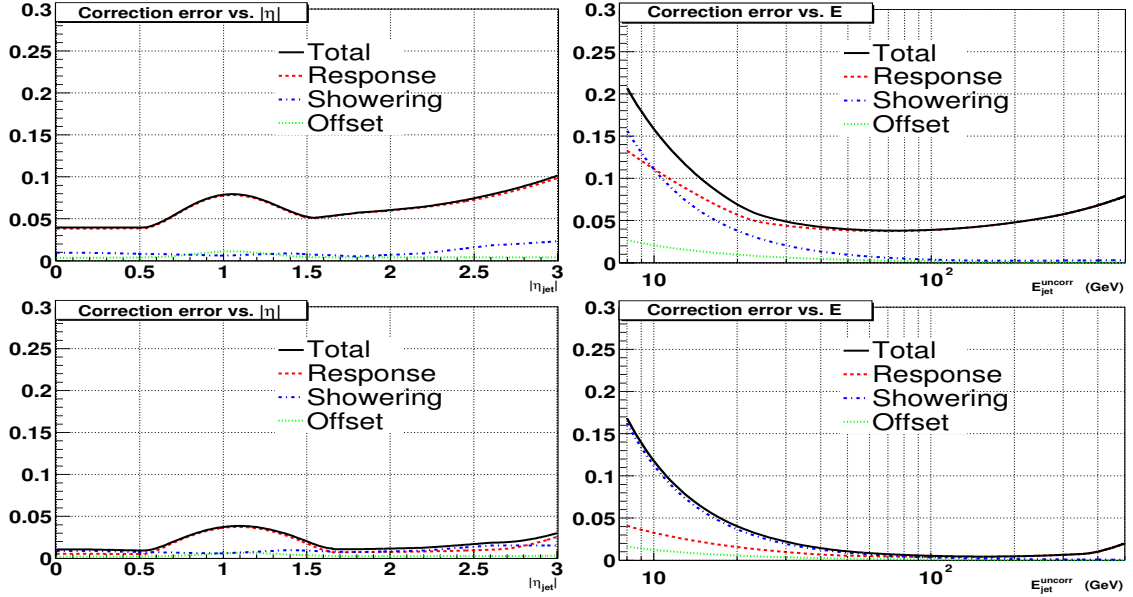
FIGURE 7.3. The 1σ uncertainties on the jet energy scale corrections for data (top) and Monte Carlo (bottom) [64]. The uncertainties are plotted as a function of η_{jet} (left) and E_{jet}^{uncorr} (right), and include both statistical and systematic components.

the statistical error on the signal efficiency divided by the efficiency. For background, it is calculated by adding in quadrature the statistical error on each source of background in Table 6.7 and dividing it by the total background yield.

Theoretical Cross Section As discussed in Section 4.4.2, no next-to-leading order theoretical production cross section is available to normalize the $WW +$ jets background. Since the leading order and next-to-leading order production cross section for the inclusive WW backgrounds differ by 35%, the leading order theoretical cross section for $WW +$ jets is scaled up by 35% and a systematic error of that amount is assigned to be conservative.

Normalization As discussed in Section 6.2.2, the $Z/\gamma^* + jets$ backgrounds are normalized with the K_Z factor. This systematic accounts for the limited statistics of the Monte Carlo samples used to calculate the K_Z factor. The error is calculated by dividing the statistical error on K_Z factor by the K_Z factor.

Both are given in Table 6.2.

A systematic is not quoted for the error associated with the top mass assumption, and this source of uncertainty is not included in the total systematic uncertainty on the measurement. Instead, the signal efficiency is plotted as a function of top mass in Figure 7.4. For each shift of the top mass by one GeV below (above) the central value, the cross section increases (decreases) by 0.05 pb in the mass range 160 GeV to 190 GeV, where the dependence is approximately linear.
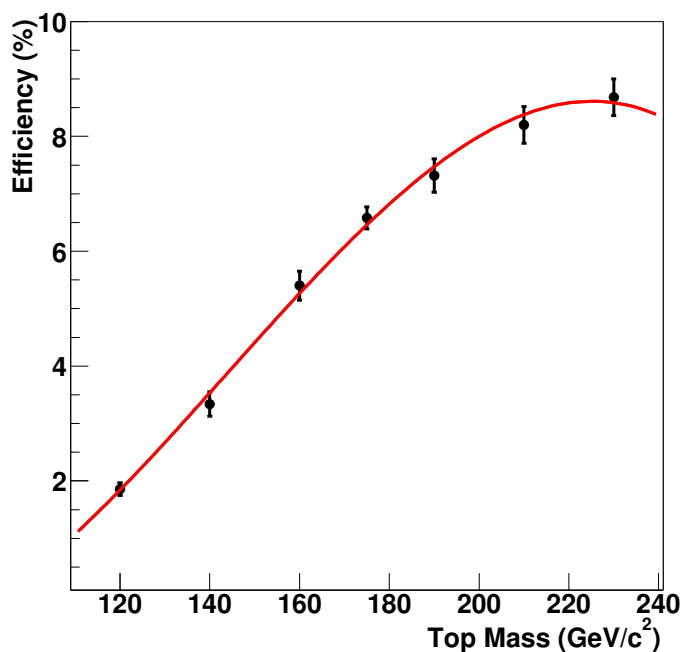
FIGURE 7.4. Signal efficiency as a function of top mass after all selection cuts have been applied. The efficiencies are estimated with $t\bar{t}$ Monte Carlo samples generated with different top mass assumptions. The errors shown are statistical errors on the Monte Carlo.

7.3 Candidate Events

A total of two candidate events pass all selection criteria. Table 7.4 summarizes the transverse momentum of the highest P_T muons and jets, as well as providing the $\not{E}_T$ and dimuon invariant mass for these events. Both candidates have a significant amount of $\not{E}_T$ and two high-P_T muons. However, the two-highest P_T muons in the 'Candidate 1' event are in the far forward region of the detector, which has poor coverage. Therefore, these muons are susceptible to misreconstruction, which could lead to an inflated value of $\not{E}_T$. The candidates are illustrated in Figure 7.5 and Figure 7.6. Three displays are shown for each candidate. Following is a brief description of the three displays.

RZ view In this view, the horizontal axis is along the direction of proton motion and the radial position (Section 3.2.1) is pictured on the vertical axis. The black lines within the inner rectangle correspond to tracks in the central tracking detectors (Section 3.2.2). Histograms, displayed between the rectangles, show energy deposits in the η slices of the calorimeter (Section 3.2.3). Red histograms represent energy deposited in the electromagnetic calorimeter, while blue represent energy deposits in the hadronic portions of the calorimeter. Note that the $\eta = 0$ line vertically bisects the figure. Hits in the three layers of the muon system (Section 3.2.4) are pictured outside the outer rectangle.

XY view This is termed the projection end view because it shows the view along the proton beam direction. Tracks are displayed within the inner circle, the energy deposited in the calorimeter is displayed in histograms between the circles, and muon hits are shown outside the figure. The color scheme is the same as in the RZ view, with the addition that calorimeter $\not{E}_T$ (Section 4.3.6) is portrayed in yellow. Muons and jets can be identified in the XY view by matching the ϕ position of each object, listed in Table 7.4, to the figure. Note that $\phi = 0$

corresponds to the three o'clock position in the XY view.

Lego plot This view is an $\eta - \phi$ plot of energy deposits in the calorimeter: red towers correspond to hits in the electromagnetic portions of the calorimeter, while blue towers correspond to hits in the hadronic sections of the calorimeter. One can easily match the jet towers in these plots to the η and ϕ positions in Table 7.4.

	Candidate 1			Candidate 2		
Object	p_T (GeV)	η	ϕ	p_T (GeV)	η	ϕ
μ_1	134.9	2.01	72°	56.59	-0.00	213°
μ_2	74.9	1.82	322°	28.76	-0.26	109°
jet_1	50.3	-0.87	225°	29.3	-0.25	111°
jet_2	20.7	1.26	173°	23.9	1.08	103°
$\not{E}_T$	87.0			87.1		
$M_{\mu\mu}$	166.1			64.3		

TABLE 7.4. Kinematic variables for the two candidate events.

7.4   Comparison to Theoretical Prediction and Other Measurements

In Chapter 2, the top pair production cross section is defined in terms of the cross sections of the gluon-gluon fusion and quark-antiquark annihilation processes and the quark and gluon distribution functions. Two theoretical calculations are discussed that predict the cross section for the current center-of-mass energy of the Tevatron, $\sqrt{s} = 1.96$ TeV. A NLO calculation that incorporates NLL corrections predicts a cross section of 6.7 ± 1 pb for $m_{top} = 175$ GeV [32]. A higher order calculation, NNLO with NNNLL corrections, predicts a cross section of 6.77 pb $\pm$ 0.42 pb [8, 9]. A measured cross section significantly below these values could indicate exotic top decays, while a measurement above prediction could indicate new top pair production mechanisms or $t\bar{t}$ resonances [10].

(a)

(b)

(c)
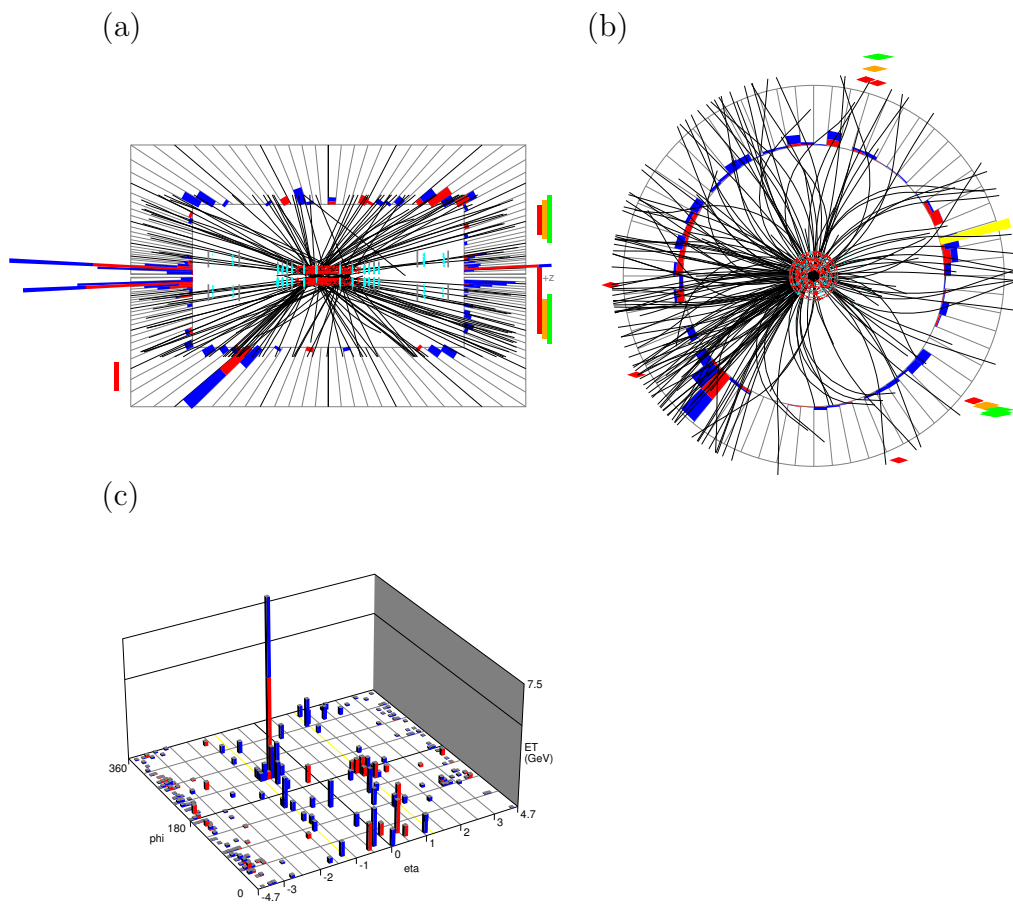
FIGURE 7.5. Candidate 1 (a) RZ view (b) XY view (c) Lego plot.

(a)

(b)

(c)

	EM
	ICD
	HAD
	CH
	missing Et
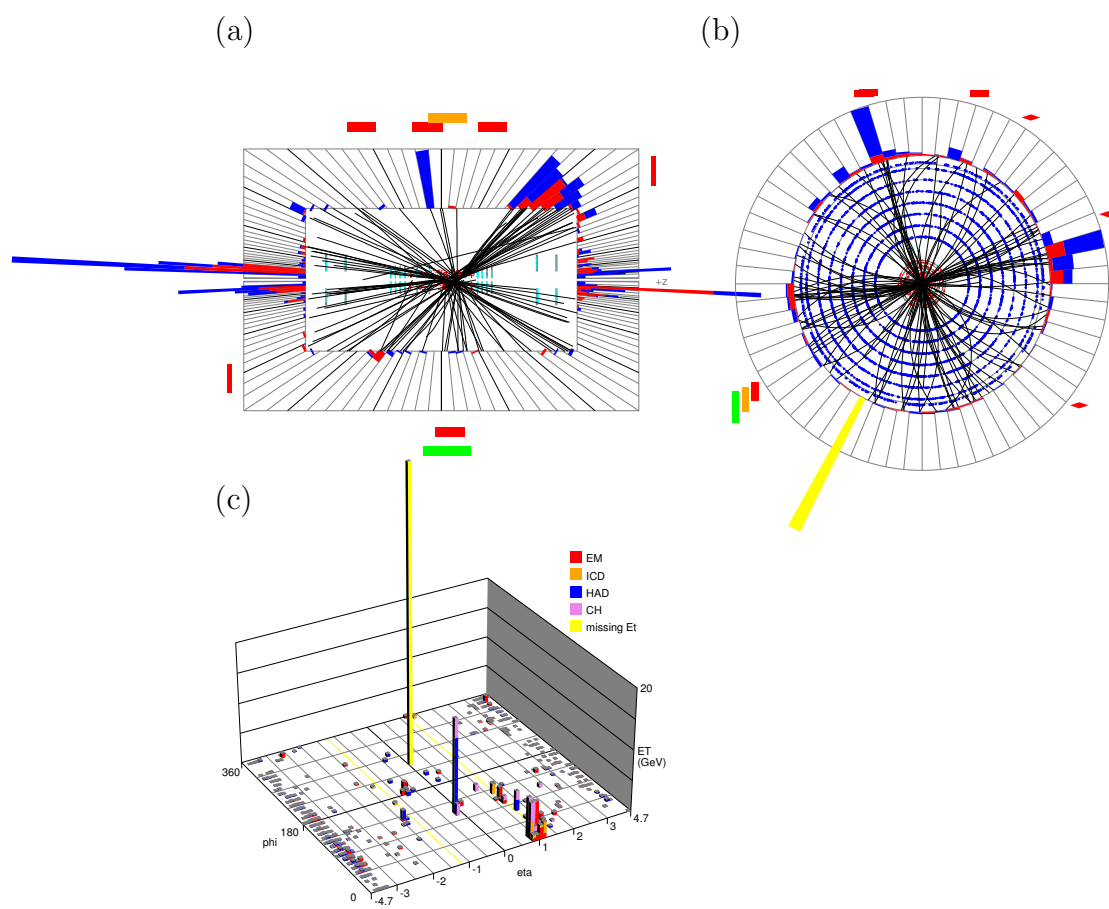
FIGURE 7.6. Candidate 2 (a) RZ view (b) XY view (c) Lego plot.

At $\sigma_{t\bar{t}} = 3.13^{+4.17}_{-2.60}(stat)^{+0.92}_{-0.86}(sys) \pm 0.19(lumi)$ pb, the measurement in this thesis is consistent with both Standard Model predictions. However, this measurement is statistically limited. So although the result does not provide evidence for physics beyond the Standard Model, it cannot exclude it.

A combination of this cross section measurement with measurements in the other two dilepton decay channels, $t\bar{t} \to e\mu$ and $t\bar{t} \to ee$, as well as with alternate-selection dilepton channels that require only one fully reconstructed electron or muon per event and one track, gives $\sigma_{t\bar{t}} = 7.4 \pm 1.4(stat) \pm 0.9(sys) \pm 0.5(lumi)$ pb [38]. This combined cross section measurement is consistent with the Standard Model predictions. However, even though its statistical error is subtantially smaller than for the dimuon-only measurement, this measurement is still statistically limited.

Measurements of the top pair production cross section in the dilepton decay channels using a higher integrated luminosity at the Tevatron or Large Hadron Collider will be more precise. In fact, one such measurement has already been conducted. Utilizing approximately 750^{-1} pb of data collected with the other multipurpose detector at Fermilab, the CDF collaboration has measured a combined cross section of $8.3 \pm 1.5(stat) \pm 1.00(sys) \pm 0.5(lumi)$ pb for the $t\bar{t} \to \mu\mu$, $t\bar{t} \to e\mu$, and $t\bar{t} \to ee$ decay channels [81]. The comparable measurement at DØ is underway utilizing a data set of approximately 1 fb^{-1}.

CHAPTER 8

CONCLUSION

This dissertation presented a measurement of the top pair production cross section in the dimuon decay channel. The measurement utilized approximately 420 pb^{-1} of data produced by Fermilab's Tevatron accelerator, which collides protons and antiprotons at a center-of-mass energy of $\sqrt{s} = 1.96$ TeV. The data was collected by the DØ detector between June 2002 and August 2004.

A series of cuts was designed to select the $t\bar{t} \rightarrow \mu\mu + \nu\nu + jj$ event signature, consisting of two muons and two jets with high transverse momenta, and significant $\not{E}_T$ from the neutrinos. Selection cuts were designed and optimized specifically to reject background events that include $Z/\gamma^* \rightarrow \tau\tau$ and $Z/\gamma^* \rightarrow \mu\mu$ events, diboson decays, and QCD multijet production and $W + jets$ events with fake isolated muons.

After all selection criteria are applied, two events are observed in data with a total expected signal plus background yield of 3.6 events. The measured cross section is:

$$\sigma_{t\bar{t}} = 3.13^{+4.17}_{-2.60}(stat)^{+0.92}_{-0.86}(sys) \pm 0.19(lumi)\text{pb} \tag{8.1}$$

assuming a top mass of 175 GeV. The dominant sources of systematic error on the measurement are the calibration of the jet energy scale and the uncertainty associated with the jet energy resolution (Section 4.3.4). This cross section measurement is consistent with recent theoretical calculations based on the Standard Model. However, it is statistics limited.

Several improvements could be made to the analysis to potentially increase statistics. The small number of observed events results, in part, from the low signal efficiency (6.4%) after all selection criteria have been applied. The most inefficient individual cuts include the muon identification requirements (70%), muon isolation

(76%), and the two background rejection cuts: χ^2_Z (72%) and the contour cut (55%). For this measurement, the muon identification cuts had already been relaxed with respect to an earlier version of the analysis, resulting in an improvement of the muon identification efficiency from $\approx 50\%$ to the current $\approx 70\%$ [49]. An alternate approach for relaxing the muon identification criteria is to require only one fully reconstructed muon per event and require an isolated track instead of the second muon. Since the isolated track could represent an electron, muon, or tau particle, both the branching ratio and signal efficiency should be higher than in the fully reconstructed dimuon analysis presented in this dissertation. A measurement using both this 'μ + track' selection and also an 'e + track' selection has already been conducted at DØ with the 420 pb^{-1} data set [82].

The muon isolation requirements could also be relaxed since the fake isolated muon background is by far the smallest source of background present in the final data sample. Studies to see if loosening the cut values from 0.12 would result in a substantial increase in signal efficiency without a significant increase in the combined QCD multijet and W+jets yield should be conducted. An even better approach might be to construct an isolation-based likelihood and fit the observed likelihood distribution to signal and background templates rather than making an isolation cut. A similar approach has been successful in the $t\bar{t} \rightarrow e\mu$ channel [79].

Several potential changes should be considered with respect to the background rejection cuts. First, the definition of the χ^2_Z variable could be extended to include $\not{E}_T$. This has been done in a different analysis, and could permit the removal of the highly inefficient contour cut [76]. Multivariate discriminates, such as likelihoods or neural nets, should also be considered as alternatives to the current background rejection cuts. Multivariate discriminants have established methods for simultaneously considering multiple variables. Additionally, neural nets are able to account for correlations between these variables.

Another powerful tool for background rejection is to require at least one jet in the

event to be tagged as originating from a b quark. 'b-tagging' is already being utilized by multiple top quark measurements at DØ and has been shown to effectively suppress the Z/γ^* background [82]. Jets are tagged as b-jets with a secondary vertex algorithm that accounts for the relatively long decay length of B hadrons. Both the primary and secondary vertices are reconstructed, and jets within a cone of $\Delta R < 0.5$ (Section 4.3.4) and with a decay length significance of more than seven ($L_{xy}/\sigma_{Lxy} > 7$) are b-tagged, where L_{xy}/σ_{Lxy} is calculated from the measured, transverse distance between the primary and secondary vertex and the associated uncertainty [83]. Although the efficiency to tag b-jets is both P_T- and η-dependent, a typical efficiency is approximately 40% for a 40 GeV jet originating from a top decay [38].

Of course, the most straightforward way to increase the event yield is to increase the luminosity. Analyses underway at DØ are currently utilizing approximately 1 fb^{-1} of data and up to 8 fb^{-1} is expected to be collected at DØ in the next few years. When the Large Hadron Collider is commissioned, more than 10 million $t\bar{t}$ pairs are expected to be produced each year, even in its low luminosity run. With this many top events, precision measurements of the top pair production cross section should be possible in all decay channels, including the $t\bar{t} \rightarrow \mu\mu$ channel. These measurements may also confirm Standard Model predictions or they could reveal new physics.

Appendix A

Level 1 Calorimeter-Track Trigger

The Level 1 Calorimeter-Track Trigger (L1CTK) was designed, built, and commissioned by the University of Arizona for DØ's Run IIb data-taking period that began in June 2006. L1CTK matches tracks from the Level 1 Central Track Trigger with electromagnetic objects and jets from the Level 1 Calorimeter Trigger. The matching is done in both position (using ϕ information) and energy (using the P_T of the tracks and the E_T of the electromagnetic objects and jets). L1CTK provides DØ's Level 1 trigger system with the additional rejection power necessary to accommodate the Tevatron's luminosity of more than 2×10^{32} cm^{-2}s^{-1} in Run IIb. L1CTK also increases DØ's triggering capability for electrons and taus. A description of L1CTK is included in this dissertation because my role in commissioning the trigger system between 2003–2007 represents my largest service work contribution to the DØ collaboration.

This appendix begins with an overview of the L1CTK trigger system, details the inputs and outputs of the system, briefly summarizes the trigger logic and performance, and ends with a review of the resources available to shifters and experts to monitor and troubleshoot the system. Since much of the L1CTK electronics and architecture is based on the Level 1 Muon Trigger (L1MUO), additional information about many of the technical details of the L1CTK trigger system can be found in L1MUO documentation such as [77]. The information included in this appendix is primarily from private communication and informal documentation, some of which is available online [84].

FIGURE A.1. L1CTK electronics crates, located in DØ's first floor movable counting house [85]. The top crate (CTKT) houses the octant trigger cards that receive detector inputs. The lower crate (CTKM) houses the manager card that forms global L1CTK trigger decisions and sends them to the Trigger Framework.

A.1   System Overview

The L1CTK trigger system consists of two custom VME electronics crates located in DØ's first floor movable counting house. The crates, shown in Figure A.1, are powered by a commercial 115 A Wiener PL500 power supply.

The formation of L1CTK triggers begins in the upper crate, the calorimeter-track trigger crate (CTKT), on eight of its nine custom VME electronics cards (Figure A.2). These eight cards, referred to as octant trigger cards, each receive information from one octant of the detector (Section A.2). This is equivalent to 10 of the 80 ϕ wedges

of the Level 1 Central Track Trigger (L1CTT) and four of the 32 ϕ wedges of the Level 1 Calorimeter Trigger (L1CAL). An additional eight ϕ wedges of data from adjacent L1CAL octants are sent to each card to aid in forming matched triggers (Section A.4). Input data are transmitted and received with Gbit/s serial links based on AMCC S2042 and S2403 fiber-optic transmitter and receiver pairs and travel over Times Microwave LMR 200 coaxial cables [86]. Each of the octant cards can accommodate up to 20 of the small daughter board receivers, though at present only 17 are used. The receivers have amplifier and equalizer circuits to account for the signal degradation that occurs in transit from the detector to the movable counting house.

Because data from the L1CAL and L1CTT inputs do not arrive at the octant trigger cards at the same time, the data must be synchronized before trigger decisions can be made. To accomplish this, receiver data are written into FIFO buffers on the trigger cards. When all FIFOs are non-empty, the data are sent to the Universal Flavor Board (UFB), a daughter card on each octant trigger card (Figure A.2). Each UFB uses a field programmable gate array (FPGA) to implement trigger logic and form trigger decisions for that octant (Section A.4). The FPGA used on the UFB is the Altera Stratix EP1S20F780.

Once octant trigger decisions are formed, they are sent via Gbit/s serial links to the lower crate, the calorimeter-track manager crate (CTKM). Here one trigger card, the manager (MTM), synchronizes the octant trigger decisions using FIFOs and combines the octant triggers to form global L1CTK triggers (Section A.4). Up to 256 such L1CTK triggers may be formed and 32 of them may be sent to the Trigger Framework (TF) to be included in the global trigger list (Section 3.2.6). Triggers are sent to the TF on two 40-wide twist-n-flat cables.

Data are buffered on both the octant trigger cards and the manager card in dual port memories (DPMs). Both input data and trigger decisions are written to these DPMs with a pointer in a FIFO keeping track of the data status. The pointer is

FIGURE A.2. L1CTK trigger card [85]. The rectangular daughter card in the center is the Universal Flavor Board on which trigger decisions are formed. The small daughter cards on the top and bottom are the serial link receivers.

initially placed in an empty FIFO. Once input data are received, the pointer moves to a 'pending Level 1 Accept' FIFO. If a Level 1 Accept is received, the pointer moves to a 'pending Level 2 Accept' FIFO. Similarly, if a Level 2 Accept is granted, the pointer moves to a 'pending transfer to Level 3' FIFO. Finally, if an event is rejected at Level 1 or Level 2, or after the event is sent to Level 3, the pointer moves back to empty [77].

Both the CTKT and CTKM crates have an additional VME electronics card, called the trigger crate manager card (MTCM). The MTCMs receive timing and global trigger information from the TF via a Muon Readout Crate (MRC 0x14) located on the third floor of DØ's movable counting house. The MTCMs send message data containing the results of the L1CTK trigger decisions to Level 3 via the same Muon Readout Crate. Timing information from the TF and Level 3 messages from the MTCM are transmitted on AMP astro cable using Cypress Hotlink chipset CY7B23/33 [86]. A twist-n-flat cable carries global trigger information to the MTCM and is used to inform the Muon Readout Crate when the L1CTK crates are front-end busy.

Finally each crate contains a VME processor used for communicating with the electronics cards. Such communication is necessary for configuring the crate after a power cycle, loading new logic to the trigger cards, and disabling inputs when they are not sending reliable data.

A.2 Inputs

Three trigger systems can send data to L1CTK: the Level 1 Central Track Trigger (L1CTT), the Level 1 Calorimeter Trigger (L1CAL), and the Level 1 Forward Preshower Trigger (L1FPS) [87]. For each of the octant trigger cards, the inputs are as follows:

- **L1CTT** The L1CTT is equally divided into 80 ϕ wedges or sectors. Each L1CTK octant trigger card receives data from 10 sectors on 10 cables. L1CTK inputs 0–9 are used for the inputs from the L1CTT. Information from the Central Preshower Detector (CPS) is also sent via these inputs.

- **L1CAL** The L1CAL is divided into 32 ϕ wedges. Each L1CTK octant trigger card receives data from 12 ϕ wedges on three cables. This corresponds to data from three octants, the primary octant as well as the neighboring octant on either side. The overlap information is utilized in the trigger logic (Section A.4) to allow for triggering on objects that cross octant boundaries. The three cables carrying L1CAL information are inputs 13–15 on the octant trigger cards.

- **L1FPS** Although not currently used in the trigger logic, L1CTK can receive inputs from the L1FPS system. L1FPS has a north and south detector, each with 16 ϕ wedges. Each octant trigger card receives inputs from one-eighth of the north detector and one-eighth of the south detector, for a total of four inputs on four cables. These cables are inputs 16–19 on the octant trigger cards.

Note that input slots 10, 11, and 12 on the octant trigger cards are currently empty. They can be used for testing or to include overlap information from L1CTT.

As mentioned in Section A.1, data from the trigger systems is transmitted with Gbit/s serial links. Each serial link can transmit 16 bits of data for each RF cycle of the Tevatron. There are seven such RF strobes for each 132 ns bunch crossing (bc) (Section 3.1). Thus, the transmitter could send as much data as [86]:

$$16 \frac{bits}{strobe} \times 7 \frac{strobe}{bc} = 112 \frac{bits}{bc}.$$

In practice, the seventh strobe is used to send longitudinal parity information. Parity is calculated on the receiver and compared to the parity generated on the transmitter. If the values differ, an error bit is raised indicating that there was a transmission problem that may affect the remaining data for this bunch crossing [77]. Excluding parity, each link transmits $96 \frac{bits}{bc}$ of data.

The input data is organized into 16-bit words. For the L1CTT inputs, each of the first six words contains information about one track. If there are less than six tracks for a given bunch crossing, some words are blank. Within each word, bits 0–5 are used to precisely define the ϕ position of each track within a sector. Bits 6–10 provide P_T information for the track. Bit 11 contains the curvature or bend direction of the track through the solenoid. Bit 12 indicates whether the track has been confirmed by hits in the CPS. Bit 13 is empty for words one to five. If a track is isolated, that is if it is the only track in that sector for that bunch crossing, this is indicated in bit 13 of the sixth word. Bit 14 is not used. Finally, bit 15 states whether the track is valid according to L1CTT information. The trigger logic requires all tracks be valid. Table A.1 summarizes this information.

For L1CAL inputs, the first and sixth words are empty. Words two through five each contain information on EM objects from one of the four ϕ slices that comprise an octant in the calorimeter. Within each of these words, bits 0–6 indicate whether an electromagnetic object (within an allowed η range) is above one of seven E_T

Word	Bit															
	0	1	2	3	4	5	6	7	8	9	10	11	12	13	14	15
1	ϕ						P_T					C	CPS			V
2	ϕ						P_T					C	CPS			V
3	ϕ						P_T					C	CPS			V
4	ϕ						P_T					C	CPS			V
5	ϕ						P_T					C	CPS			V
6	ϕ						P_T					C	CPS	ISO		V
7	Longitudinal Parity															

TABLE A.1. L1CTT inputs to L1CTK's octant trigger cards [88]. One 16-bit word is sent for each RF strobe of the Tevatron.

Word	Bit															
	0	1	2	3	4	5	6	7	8	9	10	11	12	13	14	15
1	0							0	0							0
2	EM object, ϕ slice $= 2$							0	Jet object, ϕ slice $= 2$							0
3	EM object, ϕ slice $= 3$							0	Jet object, ϕ slice $= 3$							0
4	EM object, ϕ slice $= 4$							0	Jet object, ϕ slice $= 4$							0
5	EM object, ϕ slice $= 5$							0	Jet object, ϕ slice $= 5$							0
6	0							0	0							0
7	Longitudinal Parity															

TABLE A.2. L1CAL inputs to L1CTK's octant trigger cards [89]. One 16-bit word is sent for each RF strobe of the Tevatron.

thresholds. Similarly, bits 8–14 indicate whether a jet (within an allowed η range) is above one of seven E_T thresholds. Bits 7 and 15 are not used. Table A.2 summarizes the L1CAL input information.

A.2.1 Octant Trigger Decisions

After receiving inputs from L1CTT and L1CAL (and potentially from L1FPS), each octant trigger card forms trigger decisions and sends them to the MTM. Like the input information (Section A.2), octant trigger decisions are organized into six 16-bit words.

Currently, the first word is being used to send diagnostic triggers. One example is the beginning-of-turn trigger (BOT) that should fire only on the seventh bunch crossing after the synch gap, yielding a rate of 47712 Hz. This rate and the rate of other diagnostic triggers can be monitored to quickly check synchronization and basic data quality.

For all but the first word, the 16 bits are organized into eight 2-bit counters that each contain one track-matched, single electron or jet trigger. Up to 40 such triggers can be formed, usually with specified minimum P_T and E_T thresholds for the tracks and electromagnetic objects, respectively. For certain triggers, additional requirements such as confirmation of the track from the CPS or track isolation are imposed. The 2-bit counter is used to indicate whether the trigger did not fire, fired once (a single object trigger), or more than once (a di-object trigger). In fact, the 2-bit counter scheme could be used to determine if a single object trigger fired three times, though this capability is not currently being used.

Table A.3 summarizes the octant trigger decisions sent to the MTM. Triggers have the following naming convention: CTK(Object, Multiplicity, P_T, E_T, η, Preshower, Isolation) where [90]:

- **Object** indicates whether the trigger is an electron (e), jet (j), BOT (b), or other diagnostic trigger (x). Note that although labeled only as jet triggers, the track-matched jet triggers primarily target taus (Section A.4).

- **Multiplicity** indicates the multiplicity of the trigger–either a single object trigger (1), a di-object trigger (2), or no requirement (x).

- $\boldsymbol{P_T}$ is the transverse momentum threshold the track is required to exceed. There are seven such thresholds. These are currently set to: 3 GeV, 5 GeV, 6.7 GeV, 8 GeV, 10 GeV, and 13 GeV.

- $\boldsymbol{E_T}$ is the transverse energy threshold the electron or jet is required to exceed.

There are eight possible thresholds, currently set to: 3 GeV, 4 GeV, 7 GeV, 10 GeV, 13 GeV, 15 GeV, 16 GeV, and 20 GeV.

- η indicates a regional detector requirement. The possible values are: the region covered by L1CTT (w), the region covered by the FPS detector (f), or no η requirement (x). Note that the region covered by L1CTT corresponds to $0.0 < |\eta| < 1.5$.

- **Preshower** indicates whether the track is required to be confirmed by the CPS (c) or not (x).

- **Isolation** indicates whether a track is required to be isolated as defined by L1CTT (i) or not (x).

A.3 Outputs

The MTM sums the trigger decisions received from the octant trigger cards (Section A.2.1) and sends up to 32 global L1CTK triggers to the Trigger Framework. Additionally, MTCM cards in each crate send information in the form of messages to Level 3. This section briefly summarizes the information contained in each of these two outputs from the L1CTK system.

A.3.1 MTM → Trigger Framework

The MTM sums the trigger decisions from the octant trigger cards using the same 2-bit counting scheme described in Section A.2.1. Up to 256 L1CTK triggers are formed on the MTM, and as many as 32 are sent to the TF for inclusion in the global trigger list. The set of 32 triggers sent to the TF is specified in a parameter file that can be easily modified (Section A.5.4). Table A.4 summarizes the 32 triggers L1CTK is currently sending to the TF. The naming scheme is the same as that described in Section A.2.1.

L1CTK		Octant Counters	
Word	Counter	bit 0	bit 1
0	0	ctk(b,x,x,x,x,x,x)	turn7
	1	ctk(b,x,x,x,x,x,x)&turn7	OR(cable12)
	2	l1cal test	l1ctt test
	3	ctk(x,1,10,x,w,x,x)	ctk(x,1,10,x,w,c,x)
	4	ctk(x,1,10,x,w,x,i)	ctk(x,1,10,x,w,x,i)
	5	ctk(e,1,x,10,x,x,x)	ctk(j,1,x,15,x,x,x)
	6	ctk(e,1,x,10,f,f,x)	l1fps test
	7	fpsn loose	fpss loose
1	0	ctk(e,1,5,7,w,x,x)	
	1	ctk(e,1,6.7,7,w,x,x)	
	2	ctk(e,1,6.7,10,w,x,x)	
	3	ctk(e,1,8,10,w,x,x)	
	4	ctk(e,1,10,10,w,x,x)	
	5	ctk(e,1,10,13,w,x,x)	
	6	ctk(e,1,13,16,w,x,x)	
	7	ctk(e,1,3,3,w,c,x)	
2	0	ctk(e,1,3,4,w,c,x)	
	1	ctk(e,1,5,7,w,c,x)	
	2	ctk(e,1,6.7,7,w,c,x)	
	3	ctk(e,1,6.7,10,w,c,x)	
	4	ctk(e,1,8,10,w,c,x)	
	5	ctk(e,1,3,3,w,x,i)	
	6	ctk(e,1,3,4,w,x,i)	
	7	ctk(e,1,5,7,w,x,i)	
3	0	ctk(e,1,6.7,7,w,x,i)	
	1	ctk(e,1,6.7,10,w,x,i)	
	2	ctk(e,1,8,10,w,x,i)	
	3	ctk(e,1,10,13,w,x,i)	
	4	ctk(e,1,3,3,w,c,i)	
	5	ctk(e,1,3,4,w,c,i)	
	6	ctk(e,1,5,7,w,c,i)	
	7	ctk(e,1,6.7,7,w,c,i)	
4	0	ctk(e,1,8,10,w,c,i)	
	1	ctk(j,1,5,8,w,x,x)	
	2	ctk(j,1,5,15,w,x,x)	
	3	ctk(j,1,6.7,15,w,x,x)	
	4	ctk(j,1,6.7,20,w,x,x)	
	5	ctk(j,1,8,15,w,x,x)	
	6	ctk(j,1,8,20,w,x,x)	
	7	ctk(j,1,5,5,w,x,i)	
5	0	ctk(j,1,5,8,w,x,i)	
	1	ctk(j,1,5,10,w,x,i)	
	2	ctk(j,1,5,15,w,x,i)	
	3	ctk(j,1,6.7,15,w,x,i)	
	4	ctk(j,1,6.7,20,w,x,i)	
	5	ctk(j,1,8,15,w,x,i)	
	6	ctk(j,1,8,20,w,x,i)	
	7	spare	

TABLE A.3. Trigger terms sent from the octant trigger cards to the MTM trigger card [90]. Triggers are named as CTK(Object, Multiplicity, P_T, E_T, η, Preshower, Isolation). Diagnostic and test trigger names do not necessarily conform to this naming scheme.

TF Term	Trigger
0	ctk(b,1,x,x,x,x,x)
1	ctk(b,2,x,x,x,x,x)
2	ctk(b,1,x,x,x,x,M)
3	ctk(e,1,13,16,w,x,x)
4	ctk(e,1,10,13,w,x,x)
5	ctk(e,1,10,10,w,x,x)
6	ctk(e,1,8,10,w,x,x)
7	ctk(e,1,6.7,7,w,x,x)
8	ctk(j,1,5,8,w,x,x)
9	ctk(j,1,5,15,w,x,x)
10	ctk(j,1,6.7,15,w,x,x)
11	ctk(j,1,8,20,w,x,x)
12	ctk(e,1,10,13,w,x,i)
13	ctk(e,1,8,10,w,x,i)
14	ctk(e,1,8,10,w,c,i)
15	ctk(e,2,5,7,w,x,x)
16	ctk(e,1,6.7,7,w,x,i)
17	ctk(e,1,5,7,w,c,i)
18	ctk(e,2,3,4,w,x,i)
19	ctk(e,2,3,4,w,c,i)
20	ctk(e,2,5,7,w,c,x)
21	ctk(e,1,3,4,w,c,i)
22	ctk(j,1,5,15,w,x,i)
23	ctk(e,1,6.7,7,w,c,x)
24	ctk(j,1,5,10,w,x,i)
25	ctk(e,1,6.7,7,w,c,i)
26	ctk(j,1,6.7,20,w,x,x)
27	ctk(j,1,8,15,w,x,i)
28	ctk(j,2,5,15,w,x,x)
29	ctk(j,2,8,20,w,x,x)
30	ctk(j,2,6.7,15,w,x,x)
31	ctk(j,1,8,20,w,x,i)

TABLE A.4. L1CTK triggers sent from the MTM to the Trigger Framework (TF) on TF terms 0–31 [90]. Note that these triggers are subject to change. Triggers are named as CTK(Object, Multiplicity, P_T, E_T, η, Preshower, Isolation). The trigger on term 2 is the BOT formed locally on the MTM card. The BOTs in terms 0 and 1 are the AND and OR of the BOTs formed on the octant trigger cards (Section A.2.1).

A.3.2 MTCM → Level 3

Upon receiving a Level 2 Accept, each MTCM transmits data to Level 3 in the form of a message. These messages are termed short or long based on how much information they include. The short messages contain synchronization information and the trigger decisions, while the long messages additionally include information used for monitoring and debugging the system such as copies of input data. Currently, one out of every 10 messages sent from the MTCM in the trigger crate (CTKT) is long. In the manager crate (CTKM), the short and long message are identical.

The three messages (CTKT short, CTKT long, CTKM) each share the following structure. Data are packed into blocks of 16-bit words. For all three messages, the first block is a header consisting of six words with information such as the event crossing and turn numbers. The next block of 12 words carries information about the MTCM including its serial number, readout and trigger mask registers and any latched errors. This is followed by blocks of 13 words with error and register information for each trigger card in the crate (there are eight such blocks for the CTKT, only one for CTKM).

For both the CTKT short and the CTKT long message, the next part contains eight blocks, one per card, of the octant trigger decisions. Within each of these blocks, there are seven words. The first identifies the octant and the following six contain the same six 16-bit words described in Section A.2.1. This is the end of the short message. The long message additionally contains eight blocks of 11 words each with information about each octant trigger card (serial number, input mask, lock, and parity registers) and another eight blocks of 140 words each that have the input information for each strobe on each serial link receiver. While this detailed information takes too long to send for every event, it is extremely useful. The input information can be put into a simulator that forms octant trigger decisions with the same logic as that used by the octant trigger cards. Comparing these simulated triggers to those actually formed is

Short & Long Messages			
Block Name	# of Blocks	Information	# of Words
Header	1	Crossing # & Turn #	6
CMInfo	1	MTCM Registers, Masks, and Latched Errors	12
TCErrorBlock	8	Trigger Card Latched Register and Errors	13
Trigger	8	Octant Trigger Decisions	7
Long Message Only			
TCInfo	8	Trigger Card Masks, Lock, and Parity	11
TCInput	8	Detailed Input Information	140

TABLE A.5. Contents of the Level 3 message sent by the MTCM in the CTKT crate [91]. Information specific to the trigger cards is organized into eight blocks, one per card. Information about the event or the MTCM only requires one block.

a good test of whether the octant trigger cards are working properly (Section A.5.9).

For the CTKM crate, the next part of the message after the initial three blocks also contains trigger information. The trigger term numbers that correspond to the 32 triggers sent to the TF are delivered in a block of 32 16-bit words. The next block of seven words contains information on the trigger decisions formed on the MTM (Section A.3.1). Next, an 11-word block with information on the MTM card (serial number, input mask, lock, and parity registers) is sent. Finally, a block of 56 words with all the input data from the octant trigger cards for each strobe and each receiver ends the message.

The messages for the CTKT crate and CTKM crates are summarized in Table A.5 and Table A.6, respectively.

A.4 Trigger Logic and Performance

As described in Section A.1, trigger logic implemented on the octant trigger cards' FPGAs matches L1CTT tracks with L1CAL electromagnetic objects. This matching is performed in ϕ with two simple algorithms, one for matching tracks with elec-

Short = Long Message		
Block	Information	# of Words
Header	Crossing # & Turn #	6
CMInfo	MTCM Registers, Masks, and Latched Errors	12
TCError	MTM Latched Register and Errors	13
CoorTerms	Triggers Term #'s	32
Trigger	Triggers Formed on MTM	7
TCInfo	MTM Mask, Lock and Parity	11
ReceiverPair	Detailed Input Information	56

TABLE A.6. Contents of the Level 3 message sent by the MTCM in the manager crate [91]. Since there is only one trigger card (MTM) in the CTKM crate, there is only one block for each type of information.

trons (track-matched electron triggers) and the other for matching tracks with taus (track-matched jet triggers). Matching is done in P_T and E_T by making threshold requirements (Section A.2.1). Both ϕ-matching algorithms were developed with Monte Carlo studies including single object Monte Carlo samples and those of assorted physics processes.

Figure A.3 is a scatter plot of electron hits in the 10 L1CTT sectors and four L1CAL slices per octant. It was generated with single electron Monte Carlo with a P_T range of 1–50 GeV. Hits from all eight octants are represented in the scatter plot. Electrons with hits in L1CTT sector 0 have L1CAL hits almost exclusively in slice 0. Therefore, when a track in sector 0 is reported to an L1CTK octant trigger card, the algorithm tries to match it to a L1CAL hit in slice 0. By contrast, sectors 1 and 2 in the scatter plot each have hits in two slices (slice 0 and slice 1). Thus, the algorithm looks for matching hits in two possible slices for these sectors. Table A.7 presents the full sector-slice matching algorithm derived from the Monte Carlo studies. Note that for the plot shown, a specific track P_T and electron E_T threshold were required. However, the scatter plots were studied for multiple P_T and E_T thresholds and the resulting matching algorithm was always the same.

Similarly, the matching algorithm for taus was developed based on studies with

FIGURE A.3. Scatter plot of L1CTT sectors and L1CAL slices made with single electron Monte Carlo [92]. Tracks are required to have $P_T > 3$ GeV, while electrons are required to have an $E_T > 4$ GeV. All octants are represented in the plot.

single tau Monte Carlo with a P_T range of 1–50 GeV. As seen in Figure A.4, tau hits in L1CTT sector 0 may be matched to hits in L1CAL's slice 0 or the slice 3 of the neighboring lower octant. By contrast, sector 2 hits are almost exclusively found in slice 0. These patterns are reflected in the matching algorithm for track-matched jet triggers, given in Table A.7. As with the electron algorithm, studies were conducted for multiple P_T and E_T thresholds, and no significant variation was found.

The relative efficiencies of the matching algorithms were measured with single object Monte Carlo by checking how often a L1CTT track above a certain P_T threshold would be matched to a L1CAL electron or jet above a certain E_T threshold. In all cases, this L1CTK matching efficiency was found to be greater than 99%. Figure A.5 and Figure A.6 show the relative efficiencies to match 3 GeV tracks with electrons and jets of several different E_T thresholds.
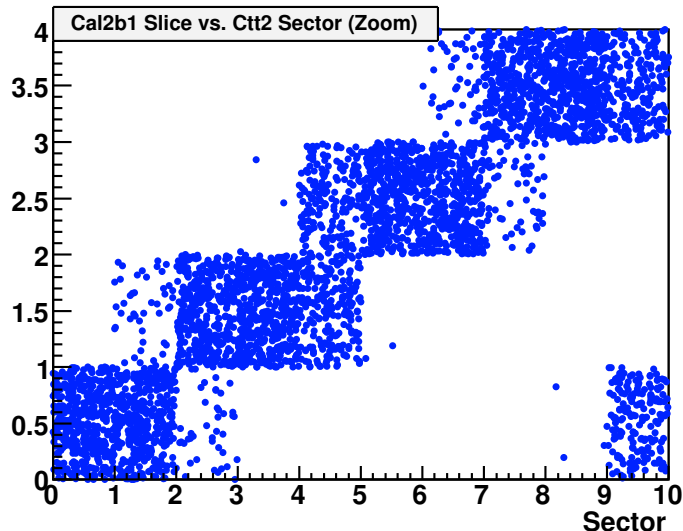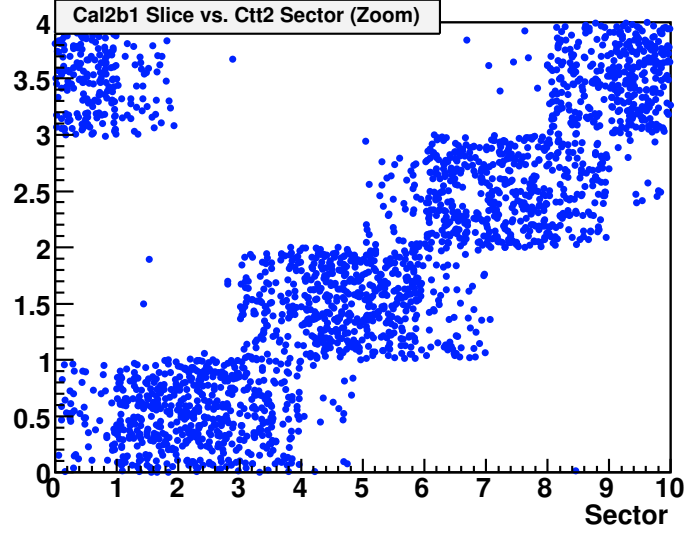
FIGURE A.4. Scatter plots of L1CTT sectors and L1CAL slices made with single tau Monte Carlo [92]. Tracks are required to have $P_T > 3$ GeV, while taus are required to have an $E_T > 5$ GeV. All octants are represented in the plot.

	Electrons			Jets	
CTT Sector	Center in L1CAL Slices	Matched Slice(s)	CTT Sector	Center in L1CAL Slices	Matched Slice(s)
0	0.2	0	0	0.2	0, −1
1	0.6	0,1	1	0.6	0, −1
2	1	1,0	2	1	0
3	1.4	1	3	1.4	1,0
4	1.8	1,2	4	1.8	1
5	2.2	2	5	2.2	2, 1
6	2.6	2,3	6	2.6	2,1
7	3	3,2	7	3	2
8	3.4	3	8	3.4	3, 2
9	3.8	3,4	9	3.8	3

TABLE A.7. The matching scheme for track-matched electron and track-matched jet triggers [92]. For each octant there are 10 L1CTT sectors (labeled 0–9) and 4 L1CAL slices (labeled 0–3). The position within a slice that the center of each sector points to is indicated for reference. A slice value of −1 indicates the nearest slice from the lower neighboring octant. A slice value of 4 indicates the nearest slice from the higher neighboring octant.
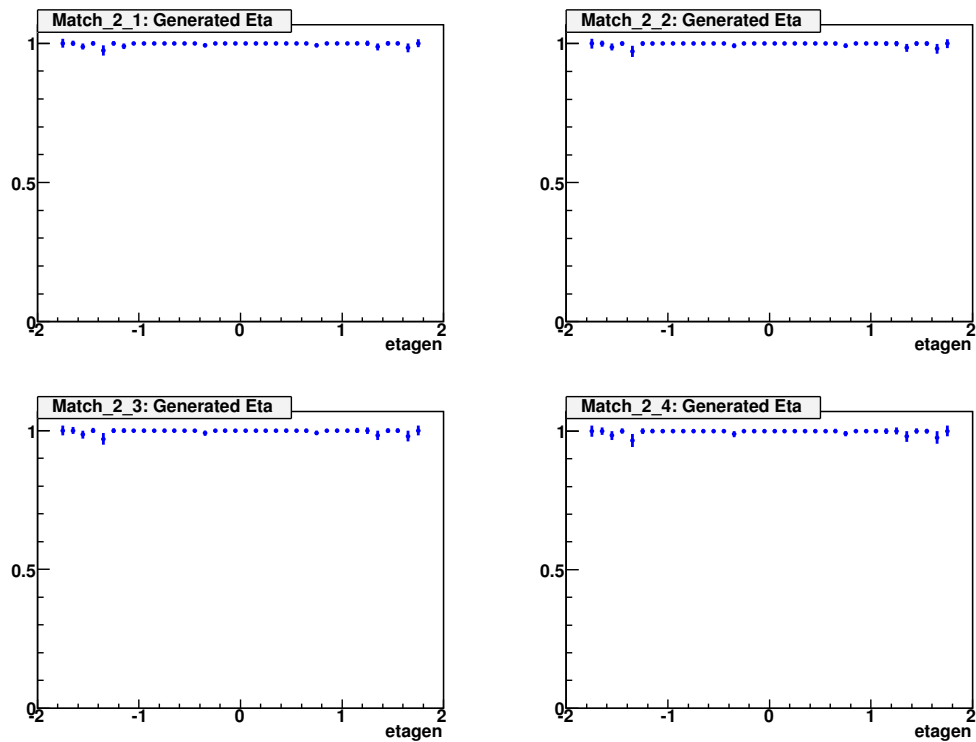
FIGURE A.5. Efficiency for matching L1CTT tracks with L1CAL electrons measured with single electron Monte Carlo [92]. Tracks are required to have $P_T > 3$ GeV. Electrons are required to have $E_T > 4$ GeV (upper left), 6.25 GeV (upper right), 15 GeV (lower left), or 20 GeV (lower right). The L1CTK matching efficiency is greater than 99% in each plot.
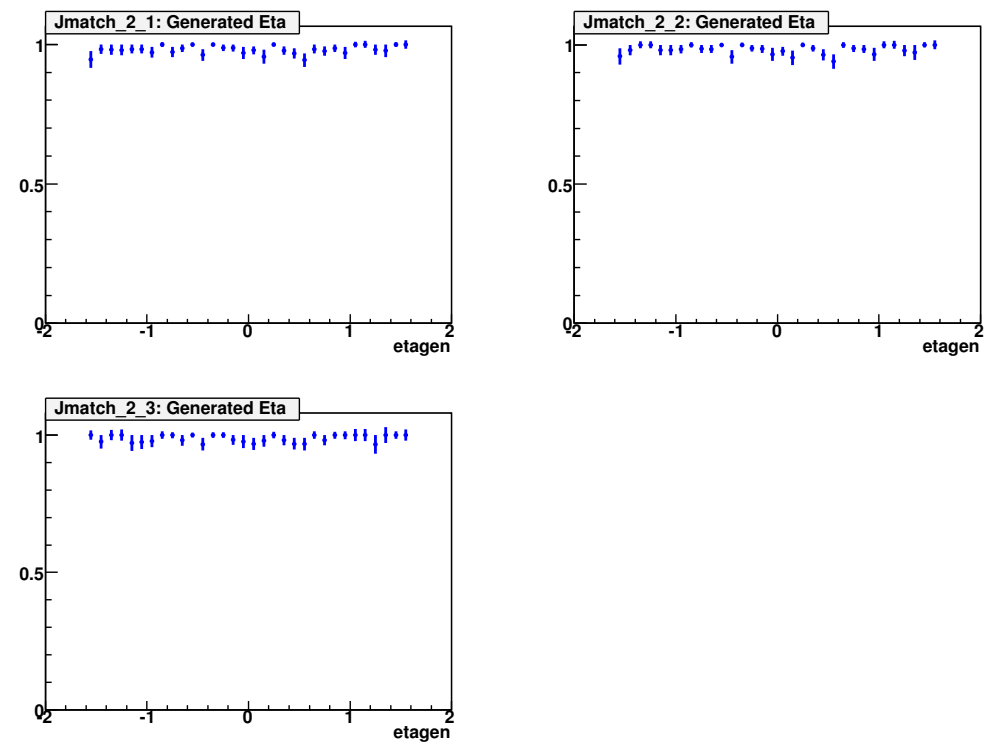
FIGURE A.6. Efficiency for matching L1CTT tracks with L1CAL jets measured with single tau Monte Carlo [92]. Tracks are required to have $P_T > 3$ GeV. Jets are required to have $E_T > 5$ GeV (upper left), 10 GeV (upper right), or 15 GeV (lower left). The L1CTK matching efficiency is greater than 99% in each plot.

A.5 Operations

This section provides a brief summary of the tools available to shifters and experts for maintaining and troubleshooting the L1CTK trigger system. Several of these tools have extensive online documentation available to members of the DØ collaboration on DØ's WIKI system [93].

A.5.1 The Input Gui

The input gui can be used by shifters or experts to cold start or configure the crates as well as to enable or disable specific inputs to the trigger cards. It can also be used by experts to modify the parameter files of the two MTCMs and to change or re-map the triggers that are sent to the Trigger Framework.

A detailed note about the input gui is available online [87]. Within the gui, help is available in the red panel on the left side of the gui window or from the 'Help' menu option at the top of the screen.

The input gui can be started from any online machine by typing:

- **setup d0online**

- **/projects/l1muo/l1caltrack/input_gui/l1ctk_inputs.py (-x)** Typing this command without the flag will open the gui in normal or shifter mode. In this case, expert tools will be disabled. Typing the optional (-x) flag opens the gui in expert mode. Once the gui has been started, the mode can be changed from the 'Mode' menu option at the top of the screen.

A.5.2 Configuring and Restoring the Crates

After a power cycle or after new logic has been loaded, a cold start should be performed to configure the crates. Cold starting may also be necessary if a crate is in a bad state.

The simplest way to cold start the crates is with the input gui:

- Make sure the run is paused or that MRC 0x14 is out of the run.

- Choose the 'General Tools' tab at the top of the gui. Choose the 'Main' subtab. Press 'Setup CTKT' and/or 'Setup CTKM' to cold start one or both crates. If you have just power cycled and you receive an error, you may have tried to cold start before the processor finished booting. Wait several minutes and try again. Also, if you or someone else is logged into the processor (for example via the VxWorks gui), the crate will not cold start successfully. Log out, and try again.

The crates may also be cold started within the VxWorks gui (Section A.5.6).

A.5.3   Enabling and Disabling Inputs

If there are known problems with one or more inputs to L1CTK, they should be disabled. Once fixed, they should be re-enabled as quickly as possible. Both of these tasks can be performed with the input gui.
To disable a L1CTK input:

- Ask for the run to be stopped or paused. (During data-taking it is advisable to ask for a run transition since disabling or enabling an input constitutes a configuration change.)

- In the 'General Tools' tab, click on the subtab for the type of input you want to disable (CTT, CAL, FPS, or an octant card input to the CTKM). Then, click on the input until it turns from red to gray. Note that if you wish to disable only one of the 24 L1CAL inputs (as opposed to disabling one octant, which corresponds to three inputs), the gui must be in expert mode.

- Click on 'Write params.dat files'.

- Click on either 'Restore CTKT' or 'Restore CTKM'.

- Ask for an sclinit and for the run to be resumed for started.

Experts can also enable or disable inputs by directly modifying the parameter files:

/projects/l1muo/l1caltrack/vxstuff/ctkt_params.dat

/projects/l1muo/l1caltrack/vxstuff/ctkm_params.dat

However, one should not modify the parameter files while simultaneously using the gui to enable or disable inputs. Choose one method or the other!

A.5.4   Changing Parameter Files

Experts may use the 'Expert Tools' tab in the input gui to modify MTCM parameters or to change the triggers that are mapped to the Trigger Framework. To change MTCM parameters, choose either the 'Expert-CTKM MTCM' or the 'Expert-CTKT MTCM' subtab. Type in the desired term, press 'Write params.dat files', and restore the appropriate crate. The 'Check MTCM terms' button simply checks that you have typed in a valid term.

You can also change the masks of manager and trigger cards on these pages. After modifying a mask, press the 'Use These Masks' button. Do not use the 'Write params.dat' button! This button is equivalent to the 'Use General Masks' button and will write the masks from the 'General Tools' pages.

To re-map the trigger terms sent to the TF, choose either the 'Expert-CTKM Trigs' or the 'Expert-CTKT Trigs' subtab. These pages display the 32 triggers sent by a card to the TF when the twist'n'flat cable is attached. (In standard configuration, the twist'n'flat cable is connected to the MTM.) Triggers can be changed by clicking on a trigger name and typing either the name or the number associated with the desired trigger. The 'Check all Triggers' button checks that the names or the numbers correspond to valid triggers. The 'Show all Trigger Names' button displays

all available triggers (up to 256) in a separate window. After modifying the page, press 'Write params.dat' and restore the crate.

A.5.5   Monitoring the Registers

A python script can be utilized to check the mask, lock, and parity registers for each L1CTK crate. This tool is useful when trying to debug a bad BOT or an out-of-synchronization error on MRC 0x14 that you suspect may be related to a particular input.

The script can be run from any online machine by typing:

- **setup d0online**

- **/projects/l1muo/REGmonitor/calTrack_mon.py <proc> (card slot)**
  where <proc> is the name of the processor in the appropriate L1CTK crate ('d0olmuo27' for CTKT and 'd0olmuo24' for CTKM). The optional 'card slot' allows you to specify the cards for which the script should check the registers. If no card is specified, registers are checked for all cards.

- Choose **(r)** to read the registers, **(c)** to clear the parity register and then read the registers, or **(e)** to exit.

The output of the script is written in columns headed by 'Card', 'Mask 1', 'Mask 2', 'Lock 1', 'Lock 2', 'Parity 1', and 'Parity 2', where the 1 and 2 refer to inputs 0–15 and inputs 16–19, respectively. The register values are printed in hexadecimal numbers. If there are no parity errors, 'Parity 1' and 'Parity 2' should read '0x0'. The masks should be the same as those in the parameter files.

A gui similar to the L1MUO Crate Monitoring gui has been written for L1CTK. This gui displays mask, lock, parity, and FIFO full information for all the inputs. Unfortunately, insufficient memory on the L1CTK processors currently makes this gui unusable. The gui can be started by typing:

- **setup d0online**

- **/projects/l1muo/l1caltrack/REGmonitor/CrateMonitor**

A.5.6   VxWorks

The VxWorks gui can be used to read and write registers, cold start or restore crates, and to load new logic to any of the electronics cards [94]. It can be started by typing:

- **setup d0online**

- **setup pyxml**

- **/projects/l1muo/VxWorks/VxWorks5_0/vxworks**

The first step in using VxWorks is to log into the processor for the appropriate crate. Choose 'Processors' from the 'Start' menu and select either 'd0olmuo24' (CTKM) or 'd0olmuo27' (CTKT). Registers can be read or modified in VxWorks by choosing the 'VME' option from the menu at the top of the screen and the 'Ethernet Read/Write' option within 'VME'. The crates can be cold started or restored by typing **cd "/projects/l1muo/l1caltrack/vxstuff"** and then either <**setup-mtccal** or <**restore-mtccal** in the command line of VxWorks window.

Since either of the above tasks can be completed with the input gui, the most common use of VxWorks is to load logic to a MTCM or a trigger card. Before being used in an L1CTK crate, a MTCM must be loaded with FPGA logic, a Message Builder that writes the Level 3 messages, and the Level 3 messages. Note that the Message Builder must be loaded and the crate must be cold started before the messages can be successfully loaded.

To upload logic or the Message Builder to a MTCM:

- Choose 'MTCM' from the menu at the top of the screen and select 'New NVRam, FPGA Loader'.

- Select either 'MTCM Logic' or 'Message Builder' and change the file name in the appropriate box if necessary.

- Press 'Write and Verify' and the 'Load NVRAM' button. Use 'Read and Verify' to confirm success.

- Cold start the crate. Remember that the run should be paused or MRC 0x14 should be taken out of the run during a cold start!

To load a new message:

- Choose 'L2/L3 Message' from the 'MTCM' menu.

- Go through the menu boxes to select the relevant message (i.e.'ufb', 'L3', 'short' or 'long').

- Press 'Load'.

- Press 'Save NVRam'.

- Cold start the crate.

To load logic to the octant trigger cards or to the MTM:

- Choose the 'Load Flash Memory' from the 'MTCXX' window.

- Go through the menu boxes, one by one, selecting the location of the trigger logic file (i.e. '36 x36', 'ufb', 'v0.1', and either 'oct0' for an octant trigger card or 'mtm' for the manager card). For the 'VME slot', select the slot for the appropriate card. The octant trigger cards are in the odd slots from 1–15. The MTM is in slot 4.

- Press 'Load and Transfer' and then use 'Test Flash' to verify success.

- Cold start the crate.

Table A.8 lists the current locations of the logic files.

Card & File Type	File Location
MTCM FPGA Logic	/projects/l1muo/vxstuff/rbf/36x36/new-mtcm/v0.1/mtcm-050127.rbf
MTCM Message Builder	/projects/l1muo/vxstuff/rbf/36x36/new-mtcm/v0.1/message_builder-050422.rbf
Octant Trigger Card Logic	/projects/l1muo/vxstuff/rbf/36x36/ufb/v0.1/oct0/UFB_Stratix_Chip_Logic.rbf
MTM Logic	/projects/l1muo/vxstuff/rbf/36x36/ufb/v0.1/mtm/UFB_Stratix_Chip_Logic.rbf

TABLE A.8. Current locations of logic files for L1CTK cards.

A.5.7   The Power Supply

The Wiener power supply is connected via a CANBUS system that is shared with the L1CAL power supplies. CALMUO shifters monitor the L1CTK and L1CAL supplies with a common gui.

A standalone gui with just the L1CTK power supply is available for remote monitoring by experts. It can be started from any online machine by typing:

- **setup d0online**

- **/projects/l1muo/l1caltrack/lvps/testPS**

The eight channels (U0–U8) correspond to the eight voltage modules. U0–U3 are the 5 V, 12 V, −12 V, and 3.3 V modules respectively for the CTKT crate, and U4–U7 are the corresponding voltage modules for the CTKM crate.

If the power supply trips, it can be manually powered on by flipping the on/off switch on the front panel. If you ask a shifter to power on the supply, have them go to Rack 119 of the first floor movable counting house and be sure to note the error message on the front panel. The error should specify which of the eight modules tripped and for what reason (overcurrent, overvoltage, etc.). After power cycling, both crates will need to be configured (Section A.5.2). If the supply trips regularly, the limits may need to be adjusted.

To reset the trip limits or to modify other power supply settings, first take MRC 0x14 out of the run or ensure the run is stopped or paused. Then:

- Power down the supply.

- Hold the 'mode select' toggle up while pushing 'on/off' to the 'on' position (up) and continue to hold until the display stops changing. After this, the display should be on, but the power supply off.

- Use 'mode select' to toggle to the parameter you wish to change (U0, U1, U2...PSTime, FanTime, etc.) and select it by pushing 'on/off' to the 'on' position and holding the switch until the display starts blinking.

- Toggle through the subdirectory (Imax, Vmax, Imin, etc.) and again choose the parameter you'd like to modify by pushing 'on/off' to the 'on' position and holding the switch until the display starts blinking.

- Use 'mode select' to raise (up) or lower (down) the parameter to the desired value.

- To set the new value, push 'on/off' to the 'off' position once.

- Push 'on/off' to the 'off' position a second time to return to the main menu.

- Finally, push 'on/off' to the 'off' position once more to turn the display off. Then turn on the supply normally to power the crates.

Note that for the -12 V module, the Wiener is programmed to produce 12 V, and the negative is accomplished by reversing the power cables to the supply.

A.5.8 The Muon Readout Client

The Muon Readout Client is a monitoring gui for all the muon read crates. It can be started by typing:

- **setup d0online**

- **setup D0RunII p20.04.01**

- **start_muo readout_gui**

The L1CTK crates are inputs 4a (CTKT) and 4b (CTKM) in Muon Readout Crate 0x14 (MRC 0x14). Occasionally, the crate stops responding to commands issued with the Muon Readout Client and needs to be rebooted.

To reboot MRC 0x14 from any online machine, type:

- **telnet t-d0-mch3 2035**

- **CTRL-x**

- After the crate has finished rebooting, you can exit with **CTRL-]**

- Start the readout for MRC 0x14 in the Muon Readout Client.

A.5.9 The Examine

The most comprehensive monitoring tool for the L1CTK trigger system is the online examine. It checks for differences between simulated triggers and hardware counters, synchronization errors, or significant differences between simulated and observed inputs. If found, significant event server (SES) alarms are generated. The examine is also used to generate the plots posted on the L1CTK web site (http://www-d0online.fnal.gov/www/groups/l1muo/l1caltrack/). These plots are updated every five minutes and problems can be quickly spotted by an unhappy face appearing on the first page.

The L1CTK examine utilizes code in two packages, 'l1caltrack_examine' and 'tsim_l1caltrack'. During global physics runs, the executable ('l1caltrack_examine_x' run on node 'd0ol88') uses the information from the long CTKT Level 3 message to simulate the L1CTK trigger decisions for comparisons with the actual hardware counters. Similarly, readout data from the L1CAL and L1CTT systems are used to simulate L1CTK inputs.

Hardware and simulator comparisons for each run are stored in a root file labeled 'L1CalTrackExamine_runxxxxxx.root' where 'xxxxxx' is the run number. These files

are located in '/scratch/l1muo/l1caltrack_examine'.

Although the examine is run automatically and monitored by a crontab job on five-minute intervals, it may sometimes be necessary to restart the examine or to start a separate copy on a different node for debugging purposes. Detailed instructions for building and running examine jobs are available at:

/projects/l1muo/l1caltrack/examine/README

The script that generates the summary plots for the web page is located at /projects/l1muo/l1caltrack/plot_examine_temp/cronscript_d0ol88.sh

A.5.10 Rate Check Plots

A tool similar to the rate check gui used for L1MUO to compare real-time trigger rates to those expected for a given luminosity is available for L1CTK.

The gui can be run from any online machine, by typing:

- **setup d0online**

- **/projects/l1muo/l1caltrack/rate_check/rategui/L1CalTrack_AllRates.py**

The expected trigger rates are derived from fits to trigger rates recorded in earlier runs. A parameter file specifies the triggers that are used for the fits:

/projects/l1muo/l1caltrack/rate_check/fitparams_4gui.out

If you re-map the triggers that are sent to the TF, this file needs to be modified before the rate check gui can work properly. Online documentation explains how to make the appropriate modifications [93].

A.5.11 Troubleshooting

From January 2007 when L1CTK triggers were first included in the official trigger list through the time of this writing, the L1CTK system has been remarkably stable. Still, problems occasionally occur. The three most likely problems are:

1. The online examine reports an error.

2. The power supply trips.

3. MRC 0x14 reports an error.

This section provides brief suggestions for handling each of these problems.

The Online Examine Reports an Error As described in Section A.5.9, a failed synchronization check or a significant hardware-simulator difference generates an SES alarm and causes an unhappy face to appear on the front page of the examine plots. Often the problem is a bunch crossing number difference detected between one of the trigger cards and the TF. The SES alarm provides instructions to the shifters as to how they should address the problem (i.e. issue an sclinit, and/or stop and restart the readout for MRC 0x14). These actions usually resolve the alarm, and the plots appear normal as soon as they are updated (within 5 minutes).

If a persistent problem occurs, the detailed octant-level examine plots should be used to identify the card or input causing the problem. If the problem is traced to a particular card, it sometimes helps to re-configure or power cycle the crate, re-seat the card, re-seat the processor, or re-seat the crate's MTCM. If the card needs to be swapped, spares are available either in the test stand or in the FPD crate.

The Power Supply Trips Section A.5.7 describes how to power on the supply after a trip. Be sure to note the error on the display screen. It should indicate which voltage module tripped and for what reason (usually overcurrent). After power cycling, both L1CTK crates need to be cold started (Section A.5.2) and the readout for MRC 0x14 may need to be restarted.

If the supply trips regularly, the cause should be investigated. In the past, the supply tripped each time the L1CTT team performed a certain type of download. Although this issue has been resolved, a situation could arise for which the trip limits need to be reset. Instructions for this procedure are in Section A.5.7.

MRC 0x14 Reports an Error If MRC 0x14 reports an error, first click on the Crate 0x14 box in the Muon Readout Client to determine if the error is with input 0a (L1CTM) or inputs 4a or 4b (L1CTK). For any L1CTK error, first ask for an sclinit. If this doesn't help, try to determine if the error (particularly an out-of-synchronization error) could be caused by a bad input to the L1CTK trigger system. Use the script to check lock and parity registers (Section A.5.5). It may also be helpful to check the trigger rates—verifying the BOTs with the DAQ monitor and running the rate check gui (Section A.5.10). This helps to determine if the problem is with the L1CTK hardware (or one of its inputs) or is only in the readout chain.

If the problem is with a specific input, ask the expert of the relevant subsystem to try to resolve the error. If this is not possible, mask the input off to L1CTK (Section A.5.3) and ask for another sclinit. The readout for MRC 0x14 may also need to be stopped and restarted. Note that an input problem could also be with a receiver on of the the octant trigger cards. In this case, the card may need to be swapped.

If the rates, lock registers, and parity registers are all okay and the readout crate will not respond or the issue can not be resolved by stopping and restarting the readout, the next step is to reboot the readout crate. Instructions are in Section A.5.8. If this fails to resolve the problem, you can ask the DAQ shifter to reset the SBC or you can manually reset the SBC on the third floor of the movable counting house. It is usually a good idea to reset the processor at the same time. After this, the readout for MRC 0x14 should be restarted. If all of these steps fail, a Level 3 expert should be contacted. They may recommend power cycling the crate on the third floor of the movable counting house.

References

[1] S. Abachi *et al.* [DØ Collaboration], Phys. Rev. Lett. **74**, 2632 (1995) [arXiv:hep-ex/9503003].

[2] F. Abe *et al.* [CDF Collaboration], Phys. Rev. Lett. **74**, 2626 (1995) [arXiv:hep-ex/9503002].

[3] S. W. Herb *et al.*, Phys. Rev. Lett. **39**, 252 (1977).

[4] *CDF Top Quark Physics Results*, Fermi National Accelerator Laboratory, 29 April 2007 <http://www-cdf.fnal.gov/physics/new/top/top.html>.

[5] *DØ Top Quark Physics Results*, Fermi National Accelerator Laboratory, 29 April 2007 <http://www-d0.fnal.gov/Run2Physics/WWW/results/top.htm>.

[6] Visual Media Services, Fermi National Accelerator Laboratory, Photographer: Reidar Hahn (2003).

[7] D. J. Griffiths, "Introduction To Elementary Particles" (John Wiley & Sons, Inc., New York, 1987).

[8] N. Kidonakis and R. Vogt, Int. J. Mod. Phys. A **20**, 3171 (2005) [arXiv:hep-ph/0410367].

[9] N. Kidonakis and R. Vogt, Phys. Rev. D **68**, 114014 (2003) [arXiv:hep-ph/0308222].

[10] C. T. Hill and S. J. Parke, Phys. Rev. D **49**, 4454 (1994) [arXiv:hep-ph/9312324].

[11] O. M. Rohne, Eur. Phys. J. directC **4S1**, 15 (2002).

[12] F. Beaudette [CMS Collaboration], CMS-CR-2005-010 (2005) [arXiv:hep-ex/0506056].

[13] W.-M. Yao *et al.* [Particle Data Group], J. Phys. G **33**, 1 (2006).

[14] S. F. Novaes, IFT-P/010/2000 (2000) [arXiv:hep-ph/0001283].

[15] C. Quigg, Front. Phys. **56**, 1 (1983).

[16] D. Chakraborty, J. Konigsberg and D. L. Rainwater, Ann. Rev. Nucl. Part. Sci. **53**, 301 (2003) [arXiv:hep-ph/0303092].

[17] E. Brubaker *et al.* [Tevatron Electroweak Working Group], [arXiv:hep-ex/0608032].

[18] G. 't Hooft and M. J. G. Veltman, Nucl. Phys. B **44**, 189 (1972).

[19] A. Khodjamirian, SI-HEP-2004-03 (2003) [arXiv:hep-ph/0403145].

[20] S. L. Glashow, Nucl. Phys. **22**, 579 (1961).

[21] A. Salam and J. C. Ward, Phys. Lett. **13**, 168 (1964).

[22] S. Weinberg, Phys. Rev. Lett. **19**, 1264 (1967).

[23] P. W. Higgs, Phys. Lett. **12**, 132 (1964); P. W. Higgs, Phys. Rev. Lett. **13**, 508 (1964); P. W. Higgs, Phys. Rev. **145**, 1156 (1966).

[24] F. Englert and R. Brout, Phys. Rev. Lett. **13**, 321 (1964).

[25] G. S. Guralnik, C. R. Hagen and T. W. B. Kibble, Phys. Rev. Lett. **13**, 585 (1964).

[26] T. W. B. Kibble, Phys. Rev. **155**, 1554 (1967).

[27] T. Kawamoto [LEP Collaborations], "Precision measurements at LEP and LEP-2," 25th SLAC Summer Institute on Particle Physics: Physics of Leptons (SSI 97), Stanford, CA (1997).

[28] G. Altarelli and M. W. Grünewald, Phys. Rept. **403-404**, 189 (2004) [arXiv:hep-ph/0404165].

[29] G. W. Bennett *et al.* [Muon G-2 Collaboration], Phys. Rev. D **73**, 072003 (2006) [arXiv:hep-ex/0602035].

[30] R. K. Ellis, W. J. Stirling and B. R. Webber, Camb. Monogr. Part. Phys. Nucl. Phys. Cosmol. **8**, 1 (1996).

[31] P. Nason, S. Dawson and R. K. Ellis, Nucl. Phys. B **303**, 607 (1988).

[32] M. Cacciari, S. Frixione, M. L. Mangano, P. Nason and G. Ridolfi, JHEP **0404**, 068 (2004) [arXiv:hep-ph/0303085].

[33] S. Eidelman *et al.* [Particle Data Group], Phys. Lett. B **592**, 1 (2004).

[34] *Fermilab's Chain of Accelerators*, Fermi National Accelerator Laboratory, 29 April 2007
<http://www.fnal.gov/pub/inquiring/physics/accelerators/chainaccel.html>.

[35] B. M. Evanger *et al*, "Concepts Rookie Book v3," Beams-doc-# 1023-v1 (2002), Fermi National Accelerator Laboratory, 29 April 2007
<http://beamdocs.fnal.gov/AD-public/DocDB/ShowDocument?docid=1023>.

[36] V. M. Abazov *et al.* [D0 Collaboration], Nucl. Instrum. Meth. A **565**, 463 (2006) [arXiv:physics/0507191].

[37] Paul Telford, "Re-tuning of pmcs_chprt to P13 and P14 Data," internal DØ Note 4297 (2004).

[38] V. M. Abazov *et al.* [D0 Collaboration], "Measurement of the $t\bar{t}$ Production Cross Section in $p\bar{p}$ Collisions Using Dilepton Events," *in preparation* (2007).

[39] W. R. Leo, "Techniques for Nuclear and Particle Physics Experiments: A How To Approach" (Springer, Berlin and Heidelberg, 1987).

[40] C. Clément *et al.*, "MuonID Certification for p14," internal DØ Note 4350 (2004).

[41] The DØ Collaboration, "Improved Determination of the DØ Luminosity," internal DØ Note 5140 (2006).

[42] *Run II Reconstruction Program Status - Version p14*, Fermi National Accelerator Laboratory, 29 April 2007 <http://www-d0.fnal.gov/computing/algorithms/status/p14.html#overview>.

[43] *Common Samples Group: PASS 2 Skimmed Datasets*, Fermi National Accelerator Laboratory, 29 April 2007 <http://www-d0.fnal.gov/Run2Physics/cs/skimming/pass2.html>.

[44] *Common Samples Skim Monitoring Page*, Fermi National Acceleratory Laboratory, 29 April 2007 <http://www-clued0.fnal.gov/~shary/csskim_monitor/pass2/>.

[45] The Top Physics Group of the DØ Collaboration, "DØ Top Analysis and Data Sample for the Winter Conferences 2004," internal DØ Note 4419 (2004).

[46] M. Klute, L. Phaf, and D. Whiteson, "TopAnalyze - A Framework Analyze Package For Top Group Analyses," internal DØ Note 4122 (2003).

[47] *Top Sample Luminosity Summary*, Fermi National Accelerator Laboratory, 29 April 2007 <http://d0.phys.washington.edu/%7Egwatts/research/d0/Lumi/2004%2Dfall%2Dpass2%2D04/>.

[48] *Offline Run Quality Database Queries*, Fermi National Accelerator Laboratory, 29 April 2007 <http://d0db.fnal.gov/qualitygrabber/qualQueries.html>.

[49] S. Anderson et. al., "Measurement of the ttbar Production Cross-section at $\sqrt{s} = $ 1.96 TeV in ee and $\mu\mu$ Final States Using 370 pb^{-1} of Pass2 Data," DØ Note 4827 (2005).

[50] V. M. Abazov *et al.* [DØ Collaboration], Phys. Lett. B **626**, 55 (2005) [arXiv:hep-ex/0505082].

[51] S. Anderson et al., "Measurement of the $t\bar{t}$ production cross section at $\sqrt{s} =$ 1.96 TeV in dilepton final states," internal DØ Note 4683 (2005).

[52] M. Agelou et al., "The top trigger efficiency measurements and the `top_trigger` package," DØ Note 4512 (2004).

[53] J. Temple, "Overview of Changes in L1 Muon Logic for RunIIB," internal DØ Note 5165 (2006).

[54] J. Temple, R. McCroskey, K. Johns, "Upgrade of Level 1 Muon Trigger Logic for the v13 Trigger List," internal DØ Note 4566 (2004).

[55] H. Greenlee, "The D0 Kalman Track Fit," internal DØ Note 4303 (2003).

[56] T. Diehl et al. "Tracking Algorithm Recommendation Committee (TARC) Report II" (2003).

[57] P. V. C. Hough, International Conference on High Energy Accelerators and Instrumentation, CERN (1959).

[58] R. E. Kalman, J. Bas. Eng. **82D**, 35 (1960); R. E. Kalman and R. S. Bucy, J. Bas. Eng. **83D**, 95 (1961).

[59] A. Schwartzman, M. Narain, "Primary Vertex Selection," internal DØ Note 3906 (2001); A. Schwartzman, M. Narain, "Probabilistic Primary Vertex Selection," internal DØ Note 4042 (2002).

[60] A. García-Bellido et al, "Primary Vertex certification in p14," internal DØ Note 4320 (2004).

[61] G. Bernardi, E. Busato, J. Vlimant, "Improvements from the T42 Algorithm on Calorimeter Objects Reconstruction," internal DØ Note 4335 (2004).

[62] E. Busato, A. Andrieu, "Jet Algorithms in the D0 Run II Software: Description and User's Guide," internal DØ Note 4457 (2004).

[63] U. Baur (ed.), R. K. Ellis (ed.) and D. Zeppenfeld (ed.), FERMILAB-PUB-00-297.

[64] J. Agram, et al., "Jet Energy Scale at D0 RunII," internal DØ Note 4720 (2005).

[65] J. Kozminski et. al., "Electron Likelihood in p14," internal DØ Note 4449 (2004).

[66] M. L. Mangano, M. Moretti, F. Piccinini, R. Pittau and A. D. Polosa, JHEP **0307**, 001 (2003) [arXiv:hep-ph/0206293].

[67] H. L. Lai *et al.* [CTEQ Collaboration], Eur. Phys. J. C **12**, 375 (2000) [arXiv:hep-ph/9903282].

[68] T. Sjostrand, P. Eden, C. Friberg, L. Lonnblad, G. Miu, S. Mrenna and E. Norrbin, Comput. Phys. Commun. **135**, 238 (2001) [arXiv:hep-ph/0010017].

[69] D. J. Lange, Nucl. Instrum. Meth. A **462**, 152 (2001).

[70] S. Jadach, Z. Was, R. Decker and J. H. Kuhn, Comput. Phys. Commun. **76**, 361 (1993).

[71] J. M. Campbell and R. K. Ellis, Phys. Rev. D **60**, 113006 (1999) [arXiv:hep-ph/9905386].

[72] "Geant–Detector Description and Simulation Tool," CERN Program Library Long Writeups Q123 (1993), CERN, 29 April 2007 <http://wwwasdoc.web.cern.ch/wwwasdoc/geantold/GEANTMAIN.html>.

[73] *d0gstar_user*, Fermi National Accelerator Laboratory, 29 April 2007 <http://www-d0.fnal.gov/d0dist/dist/releases/p14.07.00/ d0gstar_user/doc/index_code.html>.

[74] *D0sim*, Fermi National Accelerator Laboratory, 29 April 2007 <http://www-d0.fnal.gov/computing/MonteCarlo/simulation/d0sim.html>.

[75] E.W. Varnes, "Track reconstruction efficiency measurement with single muons," internal DØ Note 4317 (2004).

[76] R. Hall, J.D. Hobbs, Hui Zhu, "A Study of Kinematic Fitting of $\mu\mu$ Events," internal DØ Note 2591 (1996).

[77] R. C. McCroskey, Ph.D. thesis, University of Arizona, FERMILAB-THESIS-2004-38 (2004).

[78] S. Anderson S. Burke, J. Levêque, "Update to the Summer 2005 Conference Measurement of the $t\bar{t}$ Production Cross-section at $\sqrt{s} = 1.96$ TeV in the Dimuon Final State Using 370 pb^{-1} of Data," internal DØ Note 5012 (2006).

[79] The DØ Collaboration, "Measurement of the $t\bar{t}$ Production Cross-section at $\sqrt{s} = 1.96$ TeV in Dilepton Final States Using 370 pb^{-1} of DØ Data," internal DØ Note 4850-CONF (2005).

[80] S. Anderson, "Dimuon Update,"
Talk at the DØ Top Production Meeting, 1 November 2004, (unpublished).

[81] CDF Collaboration, "A Measurement of the $t\bar{t}$ Production Cross-section Using Dileptons," Preliminary Conference Note 8103 (2006).

[82] C. Clement, S. Lager, K. Ranjan, E. Shabalina, "Top Quark Production Cross Section in the lepton + track Channel using Secondary Vertex b-tagging," internal DØ Note 5011 (2006).

[83] V. M. Abazov *et al.* [D0 Collaboration], Phys. Rev. D **74**, 112004 (2006) [arXiv:hep-ex/0611002].

[84] *L1CalTrack Trigger Documents,* The University of Arizona, 29 April 2007
<http://atlas.physics.arizona.edu/
~johns/l1muo/l1caltrack/l1caltrack-top.htm>.

[85] Photographer: Jeffrey Temple (2005).

[86] "Overview of the Level 1 Calorimeter-Track Trigger (L1CalTrack)," The University of Arizona, 29 April 2007
<http://atlas.physics.arizona.edu/~johns/l1muo/l1caltrack/
l1caltrack−overview.pdf>.

[87] J. Temple, "Masking of L1CalTrack Inputs with the l1ctk_inputs.py GUI,"
Fermi National Accelerator Laboratory, 29 April 2007
<https://plone4.fnal.gov/P1/D0Wiki/tdaq/l1caltrack/docfolder/l1ctk_doc.pdf>.

[88] *Protocols DFEA2 L1Muon,* Fermi National Accelerator Laboratory, 29 April 2007
<http://www-d0.fnal.gov/hardware/dfe/protocols/dfea2_l1muon.html>.

[89] *TAB to Cal-Track Data Transmission,* Columbia University, 29 April 2007
<http://www.nevis.columbia.edu/~evans/l1cal/hardware/tab/tab_to_caltrack.html>.

[90] S. Anderson, K. Johns, private communication.

[91] C. Armijo, "L1caltrack_MTCM_L3_Messages," The University of Arizona, 29 April 2007
<http://atlas.physics.arizona.edu/
~johns/l1muo/l1caltrack/l1caltrack-l3-messages.pdf>.

[92] S. Anderson, G. Facini, private communication.

[93] *L1CalTrack,* Fermi National Accelerator Laboratory, 29 April 2007
<https://plone4.fnal.gov/P1/D0Wiki/tdaq/l1caltrack/>.

[94] J. Temple, "Everything You Ever Needed to Know About the Level 1 Muon Trigger," Fermi National Accelerator Laboratory, 29 April 2007 <http://www-clued0.fnal.gov/~jtemple/gila2/jtemple/Documents/ l1mu_overview/l1mu.pdf>.